

For Reference

NOT TO BE TAKEN FROM THIS ROOM

Ex LIBRIS
UNIVERSITATIS
ALBERTAEANAE





THE UNIVERSITY OF ALBERTA
FACULTY OF GRADUATE STUDIES AND RESEARCH
THE UNIVERSITY OF ALBERTA

The undersigned certify that they have read, and
presenting to the Faculty of Graduate Studies and Research, for
acceptance, a thesis entitled **A LINEAR TEMPERATURE CONTROLLER FOR DESORPTION
SPECTRUM STUDIES**
DESORPTION SPECTRUM STUDIES BY OPAS CHUTATAPE. In
partial fulfillment of the requirements for the degree of Master

by



OPAS CHUTATAPE

A THESIS

SUBMITTED TO THE FACULTY OF GRADUATE STUDIES AND RESEARCH
IN PARTIAL FULFILMENT OF THE REQUIREMENTS FOR THE DEGREE
OF MASTER OF SCIENCE

DEPARTMENT OF ELECTRICAL ENGINEERING

EDMONTON, ALBERTA

SPRING, 1973

THE UNIVERSITY OF ALBERTA
FACULTY OF GRADUATE STUDIES AND RESEARCH

The undersigned certify that they have read, and
recommend to the Faculty of Graduate Studies and Research, for
acceptance, a thesis entitled A LINEAR TEMPERATURE CONTROLLER FOR
DESORPTION SPECTRUM STUDIES submitted by OPAS CHUTATAPE, in
partial fulfilment of the requirements for the degree of Master
of Science.

ABSTRACT

The processes governing the behaviour of an energetic particle when it collides with and penetrates a solid surface are exceedingly complex. Parameters such as particle type, energy, target material and orientation can be well specified and yet it is still extremely difficult to accurately predict target behaviour under any given bombardment condition. Much, however, can be learned about bombardment processes by studying the behaviour of the trapped particles as they re-evolve from the target material at elevated temperatures and a well-defined temperature-time profile can considerably facilitate evaluation of particle-solid interaction.

This thesis describes the design and construction of a control system for linearly varying the temperature of a solid target as a function of time. First, the characteristics of the heating process and of the system were investigated. Then the mathematical model of the process was derived and used to describe the system behaviour, leading to the design and construction of an electro-mechanical controller. The whole system was analysed by a frequency response method which indicated that compensation was necessary. The compensated system was finally tested and its specifications were compared with those previously set.

The controller was tested by generating post-bombardment desorption spectra from a stainless steel target which had been previously inactivated with both argon and helium ions. In comparing the activation

energies for desorption from stainless steel with earlier work, discrepancies arise, particularly at the higher temperatures. Deficiencies in adequately controlling the target temperature in these earlier studies and different target configurations may account for these differences.

ACKNOWLEDGEMENTS

The author wishes to thank his supervisors, Dr. R.P.W. Lawson and Dr. J.F. Vaneldik, for their teaching and guidance during the course of this work and throughout the writing of this thesis.

The staff and students of the Electrical Engineering Department are to be praised for making the author's stay in the Department both enjoyable and stimulating. The author is particularly indebted to Dr. P. Bryce and Mr. R. Schmaus of the High Vacuum Laboratory for many helpful discussions.

The financial support received from the Canadian International Development Agency is gratefully acknowledged.

TABLE OF CONTENTS

Page		
CHAPTER I	INTRODUCTION	1
1.1	Preliminary Remarks	1
1.2	Mathematical Analysis Background	3
1.3	Objective and Scope of the Thesis	6
CHAPTER II	HEATING PROCEDURE AND DETERMINATION OF PROCESS TRANSFER FUNCTION	8
2.1	Introduction	8
2.2	Heating Procedure and Background Information	8
2.3	Previous Work Reviewed	14
2.4	Thermal System Configurations	15
	2.4.1 Ultra-high vacuum chamber	15
	2.4.2 Filament and target arrangement	15
2.5	Thermocouple Accuracy Considerations	18
2.6	Final Thermocouple	20
2.7	Mathematical Modelling of the Heating Process	23
	2.7.1 Energy balance equations and the behaviour of the process	23

2.7.2 Linearization and representation of the process	30
2.7.3 Approximation of the transfer function of the process	34
CHAPTER III	
CONSTRUCTION OF CONTROL SYSTEM	51
3.1 Introduction	51
3.2 Schematic Diagram of the Control System	51
3.3 Type of Controller	53
3.4 Circuit Details	56
3.4.1 Ramp function generator	56
3.4.2 Comparator	56
3.4.3 The proportional plus integral controller	61
3.4.4 Trigger and triac circuits	69
3.5 Form of the Transfer Function of Each Block	74
3.5.1 Comparator	74
3.5.2 Controller	76
3.5.3 Trigger and triac circuits	77
3.6 Block Diagram Representation of the Control System	77

		<u>Page</u>
CHAPTER IV	ANALYSIS AND DESIGN	81
4.1	Introduction	81
4.2	Determination of the Frequency Response	82
	4.2.1 Experimental procedure	83
	4.2.2 Results	83
4.3	Adjustment of Controller Gains	88
4.4	Phase Lead Compensation Network	95
4.5	Pole Shifting	98
CHAPTER V	RESULTS OF TEMPERATURE CONTROL	101
5.1	Introduction	101
5.2	Step Response	101
5.3	Ramp Response	103
5.4	Accuracy and Errors in the Measurement of Temperature	115
CHAPTER VI	THE STUDY OF DESORPTION SPECTRA	117
6.1	Introduction	117
6.2	Apparatus	117
6.3	Experimental Method	119
6.4	Results	119
	6.4.1 Desorption spectra	119
	6.4.2 The determination of activation energies	127

6.4.3 Comparison to previous results by Burch ²	132	
CHAPTER VII	CONCLUSIONS	133
7.1	Summary	133
7.2	Suggestions for Further Work	135
BIBLIOGRAPHY		137

LIST OF FIGURES

	<u>Page</u>	
Figure 2.1	Diode plate current as a function of filament current.	12
Figure 2.2	Cross section of the UHV chamber showing the thermal system configurations.	16
Figure 2.3	Temperature-emf characteristic curve of type R thermocouple.	21
Figure 2.4	Thermistor bridge circuit.	22
Figure 2.5	Block diagram of the heating process.	32
Figure 2.6	Electrical analog network of the heating process.	33
Figure 2.7	Transient responses of the thermal system to step filament currents.	35
Figure 2.8	Plotted curves for the determination of poles of the system: Curve I, plot of $\log c(t)-c(\infty) / c(0)-c(\infty) $ vs. t, Curve II, asymptote of curve I, Curve III, average of $\log[\frac{c(t)}{K_m} - (1-2.2e^{-0.099t})]$ vs. t.	36
Figure 2.9	Plot of curves I, II, and III in linear scale.	38
Figure 2.10	Electrical analog for cooling process of the target.	41
Figure 2.11	Cooling curve of the target.	42

	<u>Page</u>	
Figure 2.12	Log-Log plot between $V_{th}(t_s)$ and I_f .	47
Figure 2.13	Curves between $V_{th}(t_s)$ and I_f .	48
Figure 2.14	Block diagram representing the thermal system.	50
Figure 3.1	Schematic diagram of temperature control system.	52
Figure 3.2	Simplified diagram of control system.	54
Figure 3.3	Ramp function generator.	57
Figure 3.4	Comparing bridge circuit.	58
Figure 3.5	Instrument set up for measuring and attenuating thermocouple emf.	59
Figure 3.6	Input network of the recorder.	60
Figure 3.7	Simulation of the transfer function $\frac{K_1}{T_i s} + K_2$.	61
Figure 3.8	Low drift dc. amplifier of inverted gain K_1 .	63
Figure 3.9	Low drift dc amplifier of non inverted gain K_2 .	64
Figure 3.10	Integrator.	68
Figure 3.11	Summing amplifier.	69
Figure 3.12	Trigger and triac circuits for controlling of filament current.	70
Figure 3.13	Turn on characteristics of SCR and triac.	71
Figure 3.14	Load voltage waveform.	73
Figure 3.15	Block diagram of the electrometer and recorder.	75

	<u>Page</u>
Figure 3.16	Block diagram of the control circuit. 76
Figure 3.17	Curve plotted between I_f and V_c . 78
Figure 3.18	Block diagram representing the trigger and triac circuits. 79
Figure 3.19	Block diagram of the linearized system. 80
Figure 4.1	Instrument set up for frequency response test. 84
Figure 4.2	Bode diagram of the recorder and electrometer. 85
Figure 4.3	Bode diagram of trigger and triac circuits. 87
Figure 4.4	Block diagram of the control system with calculated transfer functions. 89
Figure 4.5	Total response of elements from the trigger circuit forward to the recorder. 90
Figure 4.6	Bode diagram of the open loop transfer function for $K_2=1$ (solid lines) and that of the compensated system (dotted lines). 94
Figure 4.7	Insertion of compensation network. 97
Figure 4.8	Root locus of the system. 99
Figure 5.1	Step response of the compensated system. 102
Figure 5.2	Ramp function responses of the compensated system at various ramp speeds. 104-109
Figure 5.3	Ramp function response of the compensated system adjusted at $K_2=400$, $K_1=150$, $T_i=70$. 110

	<u>Page</u>
Figure 5.4 Error signal (V_E) for a ramp input.	111
Figure 5.5 Filament current (I_f) for a ramp input.	112
Figure 5.6 Bombarding electron current for a ramp input.	113
Figure 5.7 Thermistor bridge calibration curve.	114
Figure 6.1 Differentiating circuit.	118
Figure 6.2 Helium desorption spectra for incident ion energies of 100 to 500 ev, at constant dose 1×10^{14} ions/cm ² , heating rate 6.83°C/Sec.	120
Figure 6.3 Helium desorption spectra for incident ion energies of 600-800 ev, at constant dose 1×10^{14} ions/cm ² , heating rate 7.12°C/Sec.	121
Figure 6.4 Argon desorption spectra for incident ion energies of 200, 500 ev, at constant dose 1×10^{14} ions/cm ² and heating rate 5.25°C/Sec.	122
Figure 6.5 Argon desorption spectra for incident ion energies of 800 ev, at constant dose 1×10^{14} ions/cm ² and heating rate 6.7°C/Sec.	123

CHAPTER I

INTRODUCTION

1.1 Preliminary Remarks

In the study of outgassing and surface properties of metals and semiconductors an inert gas ion such as helium at different doses and energies may be used to bombard the surface producing defects to its atomic lattice. The gas atom finally either becomes trapped within the metal or escapes through the surface with reduced kinetic energy¹. Post bombardment heating of the target² is a useful technique for studying the trapping mechanism and location of injected ions. Heating causes escape from the trapping configuration, migration to the surface and effusion from the target. The desorbed gas pressure measured in the system when plotted with time is referred to as a "desorption spectrum".

Mathematical analysis of the desorption spectra is of a reasonably tractable nature, when the surface temperature is a specified function of time. The information obtained from the analysis includes:³

- a) the number of the various desorbing phases and the population of the individual phases;
- b) the activation energy of desorption of the various phases and
- c) the order of the desorption reaction

Four temperature functions that were used to analyze the desorption spectra are⁴

a) a step function temperature $(T=T_0+T')$

b) a linear temperature increase

with time $(T=T_0+bt)$

c) a reciprocal temperature decrease

with time $(\frac{1}{T} = \frac{1}{T_0} - bt)$

d) a series of step functions of

gradually increasing temperature

$$[T = T_0 + T_1 \{u(t) - u(t-\Delta t)\} + T_2 \{u(t-\Delta t) - u(t-2\Delta t)\} + \dots +$$

$$+ T_n \{u(t-(n-1)\Delta t)\}]$$

Generally speaking, thermal inertia associated with the surface produces an exponential function of time $[T = T_0 + T'(1 - e^{-t/\tau})]$ rather than a step function temperature increase. Then analysis of the desorption becomes complex and this temperature function is rarely used.

The linear and reciprocal temperature functions are the most widely used functions which will considerably simplify most of the analysis. The fourth temperature function is also of some importance and a temperature displacement schedule approximating to this function has been employed by Burtt et al.⁵ and Kelly⁴. It was also used to analyze the desorption from a continuum of heterogeneous sites of different desorption energies where the linear and reciprocal temperature/time function lead to a quantitatively intractable evaluation⁴.

1.2 Mathematical Analysis Background

P.A. Redhead³ has given a detailed analysis of methods for determining the activation energy, rate constant and order of reaction from the desorption experiments using two heating schedules, i.e. a linear and a reciprocal time/temperature variation. In addition G. Carter⁴ describes fully the generality of the numerical technique for the analysis of continuous energy spectra and its application to various other investigations involving a variety of surface temperature/time schedules. Some important results will be quoted here to show the advantages of a linear temperature/time function.

The Maximum Desorption Rate

The rate of desorption from a unit surface area is

$$N(t) = - \frac{d\sigma}{dt} = v_n \sigma^n \exp\left(-\frac{E}{RT}\right) \quad (1.1)$$

where N = desorption rate (molecules/cm²/sec)

σ = number of molecules desorbed (molecules/cm²)

n = the order of the desorption reaction

v_n = rate constant

E = the activation energy of desorption (K cal/mole)

R = gas constant (1.986×10^{-3} K cal/mole °K)

T = absolute temperature (°K)

For a linear change of sample temperature with time ($T=T_0+bt$) and assuming that E is independent of σ , the above equation is solved to find the temperature (T_p) at which the desorption rate is maximum.

Then :

$$\frac{E}{RT_p}^2 = (\nu_1/b) \exp(-E/R T_p) \quad \text{For } n = 1 \quad (1.2)$$

$$\left. \begin{aligned} &= (2\sigma_p \nu_2/b) \exp(-E/RT_p) \\ &= \frac{\sigma_0 \nu_2}{b} \exp(-E/RT_p) \end{aligned} \right\} \quad \text{For } n = 2 \quad (1.3a)$$

$$\left. \begin{aligned} &= \frac{\sigma_0 \nu_2}{b} \exp(-E/RT_p) \end{aligned} \right\} \quad (1.3b)$$

where σ_0 = initial surface coverage

σ_p = coverage at T_p

For a first order desorption process in which the desorption rate depends linearly upon σ , i.e. there is no interaction between adsorbed molecules in the desorption process, the relation between E and T_p is very nearly linear and, for $10^{13} > \nu_1/\sigma > 10^8$ ($^{\circ}\text{K}^{-1}$), is given to $\pm 1.5\%$ by

$$\frac{E}{RT_p} = \ln \frac{\nu_1 T_p}{b} - 3.64 \quad (1.4)$$

taking the first order rate constant $\nu_1 \approx 10^{13} \text{ sec}^{-1}$.

Carter derives the temperature at the maximum rate as :

$$T_p = - \frac{E}{R} \frac{1}{\log \left(\frac{bE}{R\nu_1} \right)} \quad (1.5)$$

In order to obtain the initial site population σ_0 , equation (1.1) is integrated to give

$$\sigma = \sigma_0 \exp[-\nu_1 \int_0^t \exp\{-\frac{E}{RT}\} dt] \quad (1.6)$$

This is eventually solved as :

$$\frac{d\sigma}{dt_p} \approx - \frac{\sigma_0 bE}{RT_p^2 e} \quad (1.7)$$

Thus the initial site population σ_0 can be deduced from the maximum rate itself.

For the second order reaction the rate equation becomes :

$$\frac{d\sigma}{dt} \approx - \nu_2 \sigma^2 \exp\{-\frac{E}{RT}\} \quad (1.8)$$

The approximate expression for the maximum desorption rate is given as

$$\frac{d\sigma}{dt_p} \approx \frac{bE\sigma_0}{4RT_p^2} \quad (1.9)$$

It can be seen that the complicated expressions are solved and approximated by simpler ones to obtain the required information when an appropriate temperature/time function is assumed. It is therefore desirable to have a linear temperature/time relation for simplifying the

analysis of desorption spectra. Furthermore, the linear temperature/time relation will clearly distinguish different peaks on a desorption spectrum which will help determine the order of the reaction simply by visual examination³.

1.3 Objective and Scope of the Thesis

This thesis describes the design of a controller capable of heating a stainless steel sample at a linear rate from room temperature (25°C) to the sample melting point with due regard to simplicity and economy. The prime requirements are:

- 1) Linearity in the temperature range of interest from 25°C up to 1200°C.
- 2) Variable heating rate from 5°C/sec to 25°C/sec.

The required specifications of the controller may be separated into two parts as follows:

a) Transient response requirements

In general it is desirable that the transient response be sufficiently fast and be sufficiently damped. For a step response from 25°C up to approximately 1200°C the following quantities are required:

- 1) Rise time (t_r): The time required for the response to rise from 10 to 90% of its final value should be less than 5 sec.
- 2) Settling time (t_s): The time required for the response to decrease to and stay within 2% of its final value should be less than 15 sec.

3) Maximum overshoot (M_p): Maximum overshoot should be less than 5% of the input amplitude, i.e., less than 60°C which corresponds to a damping ratio of between 0.7 and 0.9.

b) Steady state response

The output ramp response of the system should exactly follow various input ramp speeds but with constant steady state error in temperature. Although no stringent limit on this error is required, it should be kept small.

After designing of the controller, its stability and performance are investigated, and final specifications are determined. The final system is later compensated to obtain the required stable performance. Results are then presented in the form of linear temperature versus time curves. Some desorption spectra obtained by use of these linear temperature/time functions are shown to demonstrate the capability of the controller. The results are compared with those obtained previously.

CHAPTER II

HEATING PROCEDURE AND DETERMINATION OF
PROCESS TRANSFER FUNCTION2.1 Introduction

In this chapter a suitable heating method is chosen. Thereafter the "plant" is arranged according to this method and the actual transfer function of the thermal system is determined. The outline of this chapter is as follows:

Section 2.2 describes the heating procedure together with some background information.

Section 2.3 reviews the previous heating method and the results obtained by Burch.²

Section 2.4 describes the ultra high vacuum chamber and shows the arrangement of the thermal plant components.

Section 2.5 considers thermocouple accuracy and choice of thermocouple.

The actual thermocouple used is described in the concluding portion of section 2.6 and in the last section (2.7), the actual transfer function of the thermal system is determined.

2.2 Heating Procedure and Background Information

An electron beam is selected as the heat source to heat the

target because of its being almost contamination free and because of its extremely high temperature capabilities. Thermionic emission is the source of electrons. In principle, energy is imparted to free electrons in a thoriated tungsten filament by heating the filament. An increase in filament temperature increases electron activity and average velocity and enables the electrons to overcome the restraining forces at the filament surface and thus escape from the filaments. The emission from the filament would therefore depend upon its temperature and its work function. The thermionic emission current per unit area of emitting surface is given by the Richardson-Dushman equation:

$$J = AT^2 \exp \left(\frac{\omega_0}{kT} \right) = AT^2 \exp \left(\frac{b_0}{T} \right) \quad (2.1)$$

where J = current density in amperes/cm²,

A = a constant. For tungsten $A \approx 60.2$ amp/cm²-deg.²,

T = absolute temperature (°K),

ω_0 = work function at absolute zero. For tungsten

$\omega_0 = 4.5$ ev,

k = Boltzmann's gas constant = 1.381×10^{-16} erg/°K.

When a target at a high positive voltage is placed near to the filament the potential gradient between the target and the filament causes the electrons to move and be accelerated toward the target. The target surface will be struck by electrons of high kinetic energy. Most electrons will come to rest within the target and most of their kinetic

energy will be converted to heat. Secondary emission is also caused by the bombardment of electrons. When this happens, the striking electrons may knock one or more electrons out of the target material, giving rise to a reverse component of current which, in effect, causes a part of the kinetic energy of the primary electrons to be lost. Thus the heat energy delivered to the target will be reduced. The velocity of secondary electrons is for the most part very low and they may be attracted back to the target or to nearby materials. All metals have a low secondary emission at low primary electron potentials. The secondary emission yield (δ) of any material is defined as the ratio of the total number of secondaries per primary electron; δ reaches a maximum value at a certain primary electron potential $E_p(\max)$, usually between 200 and 400 volts for most of the metals. Beyond $E_p(\max)$ secondary emission decreases slowly and becomes constant at a value between 50 and 95 percent of the maximum value⁶. For type 304 stainless steel (clean) after degassing $\delta_{\max} = 1.18$, $E_p(\max) = 500$ volts and at $E_p = 1300$ volts, $\delta = 1.$ ⁷ At the maximum of secondary emission it is believed that the majority of the secondary electrons are liberated from a depth of several atoms into the metal. Beyond this potential the primaries penetrate still farther into the metal, and the probability that electrons knocked out of the atoms at this depth will reach the surface decreases, with the result that the secondary emission decreases.⁶ Thus it is apparent that high positive target voltage has advantages in that it reduces energy loss by secondary emission making target heating more efficient.

By increasing the filament heating current the number of electrons liberated from it may be increased. More total kinetic energy is then delivered to the target and its temperature will rise accordingly. Therefore, it appears possible to control the temperature of the target by varying of the filament current.

The configuration between the filament and target is like that of cathode and plate in the diode vacuum tube. For two parallel plane electrodes the space charge saturation current density is given by⁶

$$J = \frac{2.335 \times 10^{-6} E_p^{3/2}}{x^2} \text{ Ampere/cm}^2 \quad (2.2)$$

where E_p is potential between electrodes (volts),
 x is distance between electrodes (cm).

This equation constitutes the Child-Langmuir space charge law. When the cathode is a filament instead of a solid cathode, a number of effects contribute to making the behaviour different from that with a solid cathode. The most important effect is the voltage drop along the filament, which may cause considerable divergence from the simple three halves power law of plate current versus voltage as expressed by equation (2.2). Several correction factors have to be added to this expression⁶ to take account of the elongated filament effect.

For every constant value of cathode to plate voltage there is a certain value of cathode temperature (corresponding to a particular filament current) beyond which the plate current will remain virtually

constant as the cathode temperature is increased further. Under this condition the emission is said to be space-charge-limited. The nature of this saturation is shown in Fig. 2.1.

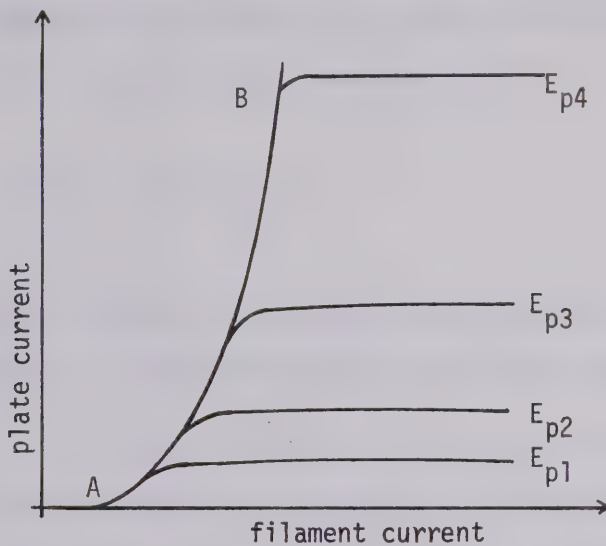


Fig. 2.1 Diode plate current as a function of filament current.

In a small region between zero filament current and that corresponding to point A (fig. 2.1) no electrons are emitted by the filament. Hence if the plate or target current is to be controlled by varying of the filament current, the proper operating region must be the region between point A and point B, i.e. in the unsaturated region. In this region target electron current is given by⁸

$$I_p = b \cdot e^{-g/I_f} \quad (2.3)$$

where b, g are constants,

I_p = plate current,

I_f = filament current.

This expression fits the experimental observations very well. Another expression which fairly accurately agrees with the experimental results over a portion of the range of I_p is

$$I_p = c I_f^m \quad (2.4)$$

where c, m are constants that depend upon the surface area of the emitter. This equation is preferred because of its simpler form.

In heating the target it is more desirable to use filament current control rather than target high voltage control because

a) the quantity of emitted electrons may be controlled more directly and easily by only small changes in filament power. The effective gain of this process is usually much higher.

b) The amount of heat delivered can be made high by setting the target voltage at a sufficiently high value. The target temperature can be controlled from room temperature up to the desired level if filament control is used. This is impossible if only the target high voltage is varied.

c) There are many other limitations in varying high voltage, i.e., narrow variable range available from the power supply, breakdown, danger in operating near high voltage and the complexity in varying and

incorporating the high voltage power supply into the control system.

2.3 Previous Work Review²

It was determined previously that the specimen heating rate, produced by applying a high current directly to the filament and with 1500 volts applied between filament and target, was approximately linear and given by

$$T = 23.5t - 100 \quad (2.5)$$

A deviation from linearity of less than 5% over the temperature range 100 to 500°C was assumed. The entire temperature curve was said to be more accurately described by

$$T' = 1.179 \times 10^{-3} t'^3 - 0.388 t'^2 + 32.8 t' - 55 \quad (2.6)$$

where $t' = t - 5$ sec ,

$$T' = T - 30^\circ\text{C}.$$

The main disadvantages of this procedure are:

a) the linear temperature-time function derived in equation (2.5) is only an approximation for the initial part of the exponential temperature rise. The equation (2.6) is not a linear temperature-time function and is too complicated.

b) the heating rate as obtained depends solely on the thermal inertias of the filament and the target, on the rate of heat loss from

target and filament and on filament radiation to the target. These characteristics cannot be varied. It, therefore, becomes more difficult to fully analyse desorption spectra for a range of specimens and temperatures.

c) the temperature-time linearity over the whole temperature interval of interest cannot be maintained.

2.4 Thermal System Configurations

2.4.1 Ultra-high vacuum chamber

The design and construction of the ultra-high vacuum system and its associated parts have been described in detail earlier². The system was designed for pressures of 1×10^{-10} torr. The essential part is the bakeable type 304 stainless steel experimental chamber six inches in diameter by twelve inches long. It incorporates ports at various positions to be used for mounting of gauges, mass spectrometer, pumps and other temporary instrumentation. Some of the ports are used to insert components into the chamber. The volume of the main chamber was found to be 8.85 litres. Figure 2.2 represents its cross section showing target, filament, and ion gun arrangement.

2.4.2 Filament and target arrangement

The filament was made from fifteen turns of 0.010 inch thoriated tungsten wire wound into a coil of about 1.6 mm diameter and enclosed in a stainless steel box of width 1.8 cm per side. One open side faced the target and was approximately 1 cm away from it. The reason for using thick wire is to enable it to withstand the erosion

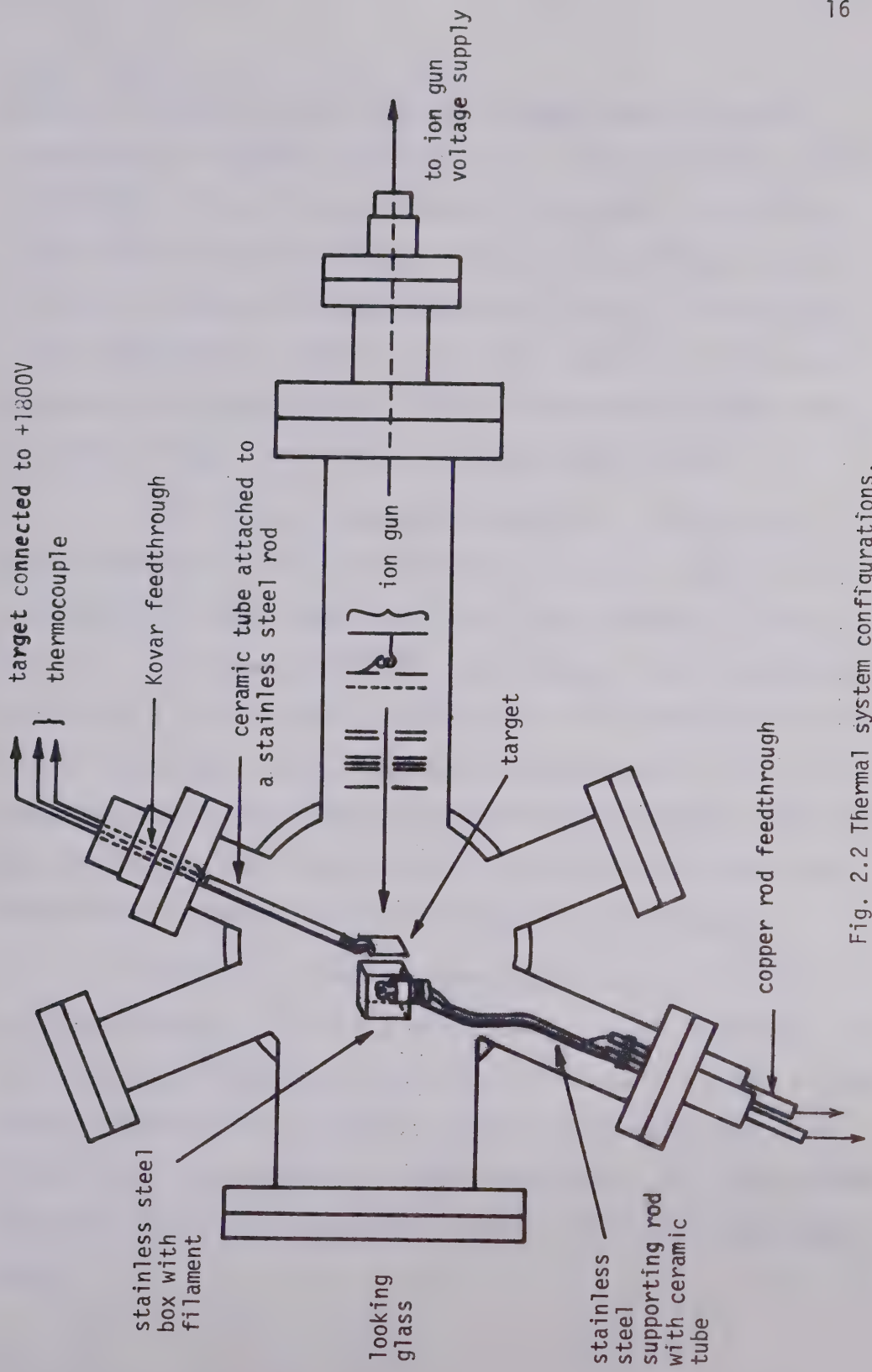


Fig. 2.2 Thermal system configurations.

caused by evaporation and by positive ion bombardment at energies corresponding to the high target potential. The positive ions referred to have their origin in residual gases in the chamber and from the target itself. Another advantage is that a thicker filament would be less likely to fracture through brittleness caused by crystallization at high temperatures. Outside the box each tungsten wire was wound together with a heavy stranded copper wire protected by ceramic tubes and passed through a hole made in the bottom side of the box.

The wires were extended and clamped to a two-lead, high current feedthrough. The aforementioned structure was supported by a stainless steel rod of approximately 0.15 cm in diameter as shown in Fig. 2.2. The box was electrically connected to a copper feedthrough by means of a stainless steel supporting rod and placed parallel to the back of the target. This arrangement fixed the stainless steel box essentially at the same potential as the enclosed filament. Hence, the electron beam could be more uniformly focused towards the target and the temperature gradient across the target could be minimized.

The target used was a square plate of type 304 stainless steel approximately 1.5 cm \times 1.5 cm \times 0.056 cm. A 0.2 cm diameter stainless steel supporting rod was carefully spot welded to the edge of the target to minimize heat conduction losses while the other end of the supporting rod was attached to a Kovar feedthrough. This target support system also acted as a ground return lead for the electron bombardment beam.

2.5 Thermocouple Accuracy Considerations

The only practical and possible way to measure the target surface temperature is to use a thermocouple. This method has the disadvantage that with the target and sensor at high voltage some portion of the instrumentation associated with the sensor must be at high voltage. Breakdown, leakage, safety and convenience become problems.

Two types of thermocouple material were considered for the application, type R-Platinum/13% Rhodium (+) versus Platinum (-) and type K-Chromel (+) Alumel (-). It was found that at a pressure of 10^{-6} torr, a type R thermocouple made of fine wire (.002 inch in diameter) could not be used because at temperatures greater than 500°C the thermocouple emf would drift negatively followed by mechanical failure of the platinum wire at a point near the target where the temperature gradient was highest.

At this high vacuum, the high temperatures caused excessive grain growth⁹ which rendered the platinum susceptible to contamination thus causing negative drifts in calibration and also resulted in mechanical failure of the platinum element. Negative calibration shifts may also be caused by diffusion of rhodium from the alloy wire into the platinum, or by volatilization of rhodium from the alloy. A type K thermocouple (0.025 inch in diameter) gave satisfactory results at the pressure range of 10^{-6} torr but the heat loss to the thermocouple was high and its larger diameter reduced the sensitivity and accuracy.

Neither thermocouple is recommended for long term use in a vacuum because of preferential volatilization of the constituent metals in the thermocouple and diffusion of impurities from the sample and insulators near the thermocouple^{9,10}. Thermal cycling is also one potential cause of errors¹⁰. The trouble was traced to precipitated impurities in the wire. Yet another possible cause of error is the presence of inhomogeneities in the wire¹⁰ in a region where there is a temperature gradient. The inhomogeneities may be present in the wire as received, or may result from contamination of the couple by sample or electrode material when welding, by diffusion of the sample material into the couple at high temperatures, or by cold work in bending or stretching. In general it would be expected that a fine thermocouple wire would be more susceptible to errors from inhomogeneities than a larger diameter wire because for a given size impurities will occupy a larger proportion of the cross sectional area of the wire and there is a lowered probability of averaging by pure metal that bridges the impurity¹⁰. A second disadvantage of fine wire, particularly in the absence of a thermocouple protection tube, is that its high surface to volume ratio results in a very sharp temperature gradient due to radiation from the wire at the worst possible place near the weld. The high temperature gradient of the fine wire can lead to the mechanical failure of the wire.

Due to the complicated structure of the vacuum chamber and the requirement that the system must be vacuum tight the reference junction of the thermocouple had to be left at a point inside the stainless steel chamber distant from, and much cooler than the target. The junction temp-

erature was determined from a thermistor bridge reading. Actual calibration of the thermocouple under the conditions of use was found to be impractical.

On the basis of the preceding facts, one can see that it is not possible to claim any high accuracy with this type of temperature measurement, since its accuracy always becomes degraded by conditions of use. Since no other suitable method of temperature measurement is available, a thermocouple must be used. To obtain reasonable accuracy despite the disadvantages mentioned, measuring instruments must be carefully aligned, leads must be carefully dressed, and manufacturer's emf data must be used.

2.6 Final Thermocouple

Despite the disadvantages of fine thermocouple wire it is desirable to use as small a wire diameter as possible in this application to minimize heat loss. Such losses cause nonuniformity of temperature across the target and slow transient response. At the same time the Pt. wire should be thick enough to avoid the aforementioned mechanical failure and withstand small leakage currents passing through it accidentally. For the same reason, no thermocouple insulator tubes should touch the sample in the immediate vicinity of the spot measured.

The final system incorporated a Pt/Pt-13% Rh (type R) thermocouple with manufacturer's characteristic as shown in Fig. 2.3. Each side was made of five 0.002 inch wires wound together and welded near to the centre of the rear of the target, i.e. facing the ion gun. The ceramic

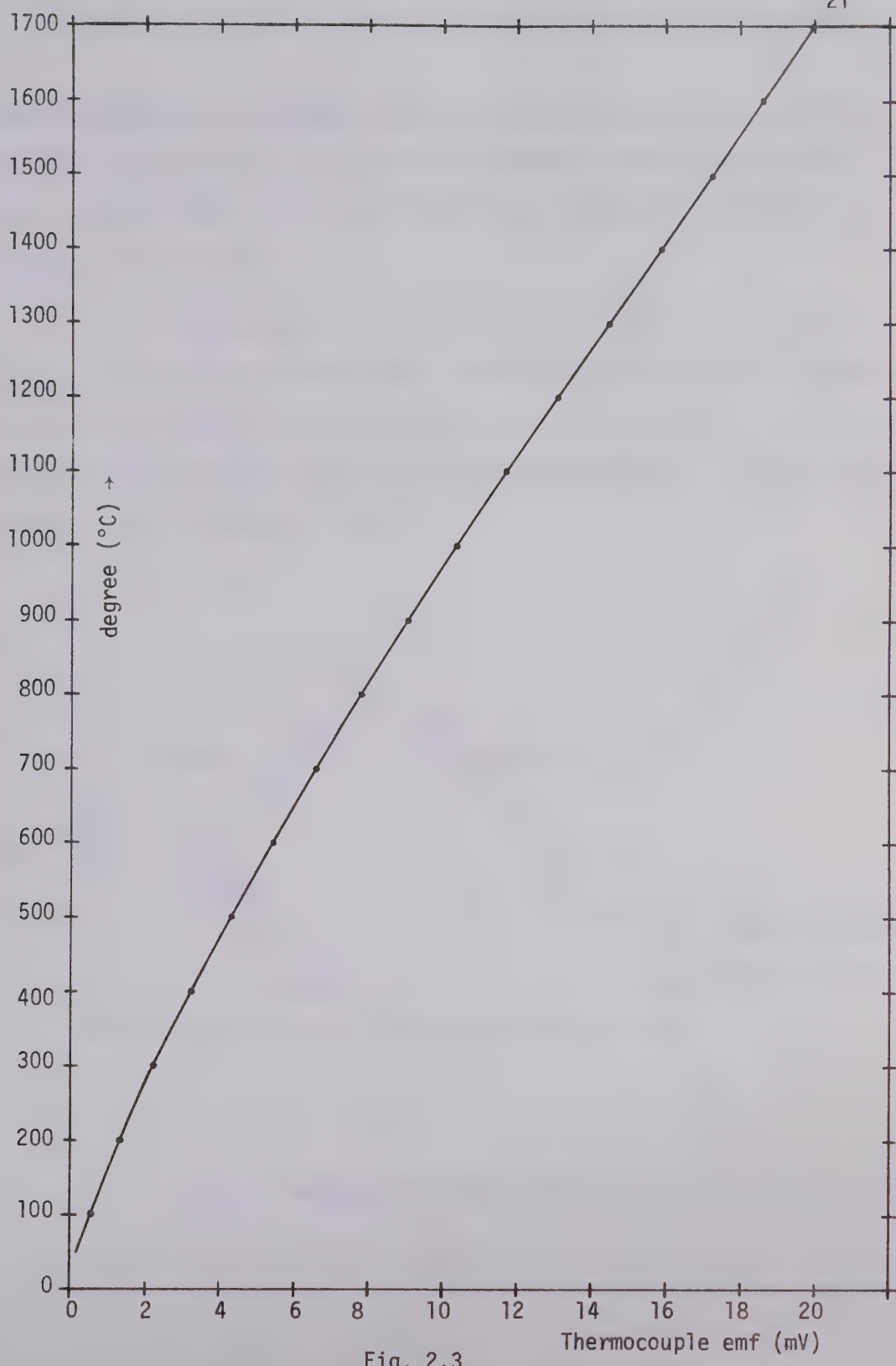


Fig. 2.3

Temperature-emf characteristic curve of type R thermocouple.

tubes attached to the supporting rod of the target were used to protect and carry the wires to an 8-pin Kovar feedthrough where the reference junction was formed. This Kovar feedthrough conducted the thermocouple emf out of the chamber.

The temperature of the reference junction was measured by placing a small glass coated Fenwal thermistor GA51L3 specially designed for precision temperature measurement, near to the junction, and connected to the outside bridge circuit by two Kovar feedthroughs. The resistance bridge circuit is shown in Fig. 2.4

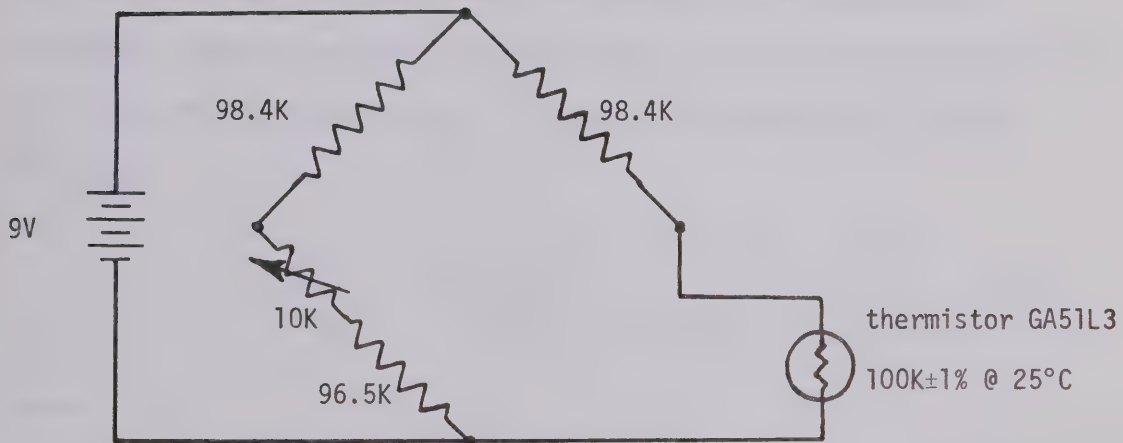


Fig. 2.4 Thermistor bridge circuit.

2.7 Mathematical Modelling of the Heating Process

2.7.1 Energy balance equations and the behaviour of the process

The target is heated by the transformed kinetic energy of electrons striking its surface and by radiation heat directly from the filament. Heat is lost from the target by conduction through the target supporting system, and by radiant energy loss from its surface to the enclosed chamber. Because the target temperature is much lower than the filament temperature no heat is radiated from the target back to the filament.

Consider the target supporting system as a homogeneous material with uniform cross sectional area A and length λ . The temperature difference between both ends is $(T-T_a)$ where T is the target temperature, T_a is the ambient temperature. The heat loss by conduction through this rod is

$$q_s = G_s (T - T_a) = k \frac{A}{\lambda} (T - T_a) \quad (2.7)$$

where

q_s = heat flow rate in watts

G_s = thermal conductance of the supporting system in
watts/ $^{\circ}\text{C}$,

k = thermal conductivity of the material in watts/ $\text{cm}^{\circ}\text{C}$.

For type 304 stainless steel $k \approx .1627$,

T, T_a are in degrees Kelvin.

Radiant heat loss from the target surface is expressed by use of Stefan-Boltzmann law^{11,12} as:

$$q_t = \sigma A_t F_{t-c} (T^4 - T_a^4) \quad (2.8)$$

where

q_t = radiant energy loss from the target in watts,

σ = universal constant = 5.73×10^{-12} watt/(cm²·° K⁴)

A_t = emitting area of the target in cm²,

F_{t-c} = shape factor between the target and the chamber surfaces,

$= \epsilon_t$ = emissivity of the target because the target is completely enclosed and small compared with the enclosing chamber.

For type 304 stainless steel $\epsilon_t = 0.44$,

T, T_a are the temperatures in degrees Kelvin.

The energy balance of the target is given by the equation

$$q_R + q_E = G_s (T - T_a) + \sigma A_t \epsilon_t (T^4 - T_a^4) + MC \frac{dT}{dt} . \quad (2.9)$$

where q_R = the radiated heat from the filament,

q_E = the kinetic energy converted to heat by electron bombardment,

M,C = mass and specific heat of the target respectively.

If the filament carries a current of I_f amperes creating a voltage drop of V_f volts, the power input is $V_f I_f$. This will cause the temperature of the filament to increase until equilibrium is reached and the heat generated becomes equal to the heat lost. Because the filament is a slender wire, little heat is conducted away by the leads and because of the high vacuum, negligible heat convection is possible. Most of the energy loss is by radiation.

The energy radiated per unit time depends only on the filament absolute temperature and is expressed by the Stefan-Boltzmann law^{11,12}:

$$P = V_f I_f = \sigma A_f \epsilon_f T_f^4 \quad (2.10)$$

where A_f = emitting area of the filament

ϵ_f = the total radiation emissivity. For pure tungsten at the normal operating temperature range of 2000-2500°K,

ϵ_t = 0.260 - 0.301 respectively.

T_f = filament temperature in °K.

If the filament is considered as a radiant heat source having very small area and spherically radiating heat with constant intensity in all directions, then, from the filament and target configurations described earlier, the target area will roughly subtend a solid angle

$\frac{4\pi}{6}$ steradian or less. This solid angle is equal to $\frac{1}{6}$ of the solid angle subtended by a sphere, measured at the center. Because $T_f \gg T_t$ no heat is reflected from the target to the filament. Therefore, the mean value of radiated heat absorbed on the target surface is

$$q_R \approx \frac{1}{6} V_f I_f \text{ or less} \quad (2.11)$$

At higher target temperatures, the filament is operated at $I_f \approx 3$ amperes, $V_f \approx 8$ volts. Therefore,

$$q_R \approx \frac{1}{6} \times 24 = 4 \text{ watts.}$$

The amount of electron bombardment heat is

$$Q_E \approx E_p I_p \text{ watts} \quad (2.12)$$

where E_p = high voltage applied between the filament and target.

A suitable value for E_p is 1800 volts.

I_p = electron bombarding current.

The value of I_p corresponding to the previous value of I_f is approximately 45 mA, therefore,

$$\begin{aligned} q_E &= 1800 \times 45 \times 10^{-3} \\ &= 81 \text{ watts.} \end{aligned}$$

Hence $q_E \approx 20 q_R$ at $I_p = 3$ amperes.

The radiant heat occurs immediately when power is applied to the filament and before the electron bombarding heat begins. It is likely that this effect helps eliminate the insensitive region before point A as shown in Fig. 2.1. The amount of heat radiated depends on the power input to the filament which is rather low and constant. This can be explained by looking at the emission equation (2.1). The exponential term accounts for most of the variation of emission with temperature. In the case of tungsten at 2500°K a 1% change in temperature changes the T^2 term by 2% but changes the exponential term by 20%. This causes the emission-temperature function to be a very rapidly varying function. The power applied to the filament is therefore changed only slightly for a large change in electron emission current.

At a target temperature of $T = 1300^{\circ}\text{K}$ the radiant heat loss can be estimated from equation (2.8)

$$q_t = 5.73 \times 10^{-12} \times 2 \times 2.25 \times 0.44 \times (28561 - 81) \times 10^8$$

$$\approx 32.4 \text{ watts.}$$

By estimating the effective dimensions of the supporting rod as being $\ell = 5\text{cm}$, $A = \pi \left(\frac{0.24}{2}\right)^2 \text{ cm}^2$, the thermal conductance is

$$G_s = 0.1627 \times \pi \left(\frac{0.24}{2}\right)^2 \times \frac{1}{5} = 1.47 \times 10^{-3} \text{ watt/}^{\circ}\text{C}$$

Hence the conduction heat loss is

$$q_s = 1.47 \times 10^{-3} \times 1000$$

$$= 1.47 \text{ watts}$$

which is only 4.35% of the total heat loss.

If this conduction heat loss is neglected the thermal energy balance equation (2.9) is reduced to

$$q_R + q_E = \sigma A_t \epsilon_t (T^4 - T_a^4) + MC \frac{dT}{dt} \quad (2.13)$$

At steady state $\frac{dT}{dt}$ is zero and the temperature of the target is

$$T_h = \left(\frac{q_R + q_E + \sigma A_t \epsilon_t T_a^4}{\sigma A_t \epsilon_t} \right)^{1/4} \quad (2.14)$$

During the cooling period the thermal energy balance is

$$\sigma A_t \epsilon_t T_a^4 = \sigma A_t \epsilon_t T^4 + MC \frac{dT}{dt} \quad (2.15)$$

Equilibrium temperature is

$$T_c = \left(\frac{\sigma A_t \epsilon t^4 T_a}{\sigma A_t \epsilon t} \right)^{1/4} = T_a \quad (2.16)$$

Equation (2.13) can be rearranged as

$$dt = \frac{MC}{Q_h \left(1 - \frac{\sigma A_t \epsilon t}{Q_h} T^4 \right)} dT \quad (2.17)$$

$$\text{where } Q_h = q_R + q_E + \sigma A_t \epsilon t T_a^4. \quad (2.18)$$

Equation (2.17) is integrated from ambient temperature T_a up to any temperature T as follows:

$$\int_0^t d\tau = t = \int_{T_a}^T \frac{MC}{Q_h \left(1 - \frac{\sigma A_t \epsilon t}{Q_h} \theta^4 \right)} d\theta \quad (2.19)$$

The right hand side integrand can be evaluated by a conventional method and the exact result is

$$t = \frac{MC}{2\sigma A_t \epsilon t T_h^4} \left[T_h \left(\text{arc tan} \frac{T}{T_h} - \text{arc tan} \frac{T_a}{T_h} \right) + \frac{T_h}{2} \left(\ln \frac{T_h + T}{T_h - T} - \ln \frac{T_h + T_a}{T_h - T_a} \right) \right] \quad (2.20)$$

A simplified form of this solution obtained by knowing the nature of this problem is¹¹

$$T = T_h - (T_h - T_a) e^{-t/\tau_h} \quad (2.21)$$

In the same manner the simplified expression for the cooling process is

$$T = T_a - (T_a - T_{hc}) e^{-t/\tau_c} \quad (2.22)$$

where $\tau_h = MC/4\sigma A_t \epsilon_t T_h^3$ (2.23)

$$\tau_c = MC/4\sigma A_t \epsilon_t T_a^3 \quad (2.24)$$

T_{hc} = temperature at the beginning of the cooling process.

It is obvious that the time constant of the heating process as defined by equation (2.23) is inversely proportional to the final temperature, or in other words, to the amount of heat input. Either the heating or the cooling process cannot actually be described by single time constants.

For the purpose of design, all processes have to be linearized so that linear analysis can be applied. In the final design, adjustment of system parameters is necessary because the system cannot be described accurately in linear terms.

2.7.2 Linearization and representation of the process.

Equation (2.13) is expanded as

$$q_R + q_E = \sigma A_t \epsilon_t (T^2 + T_a^2) (T + T_a) (T - T_a) + MC \frac{dT}{dt} \quad (2.25)$$

Let

$$\sigma A_t \epsilon_t (T^2 + T_a^2) (T + T_a) = G_t(T)$$

Assume a mean value of $T = \bar{T}$ which is constant. Then,
 $G_t(\bar{T}) = \bar{G}_t$ is constant. Also let $Q = q_R + q_E$ = heat flow input. Hence

$$Q = \bar{G}_t (T - T_a) + MC \frac{dT}{dt} \quad (2.26)$$

Rearranging and Laplace transforming this equation yields

$$\begin{aligned} T \bar{G}_t \left(\frac{MC}{\bar{G}_t} s + 1 \right) &= Q + \bar{G}_t T_a \\ T &= Q \cdot \frac{1}{\bar{G}_t \left(\frac{MC}{\bar{G}_t} s + 1 \right)} + \frac{T_a}{\left(\frac{MC}{\bar{G}_t} s + 1 \right)} \\ &= Q \cdot \frac{1}{\tau s + 1} + \frac{T_a}{\tau s + 1} \end{aligned} \quad (2.27)$$

where $\tau = \frac{MC}{\bar{G}_t}$ = a time constant.

Both q_R and q_E are functions of power input to the filament ($I_f^2 R_f$) and vary in the same direction. Each amount may be approximated to be directly proportional to I_f within its operating range. Therefore,

$$q_R = \frac{A}{\tau_f s + 1} \quad (2.28)$$

and

$$q_E = \frac{B}{\tau_f s + 1} \quad (2.29)$$

where A, B are linearized gains at steady state,

τ_f is the heating time constant of the filament.

From the previous discussions it is clear that q_R is rather constant and less than q_E . Then $A < B$.

The linearized heating process as described by equations (2.27), (2.28) and (2.29) can now be represented by the block diagram in Fig. 2.5

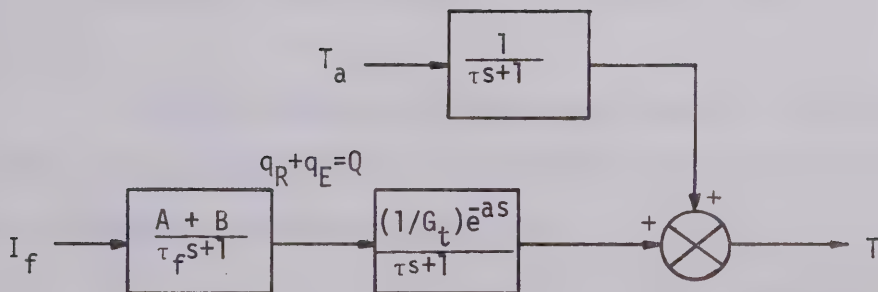


Fig. 2.5 Block diagram of the heating process

This figure also includes a transport delay "a" resulting from the physical separation between the heated surface and the thermo-couple junction. The electrical analog network¹³ is shown in Fig. 2.6

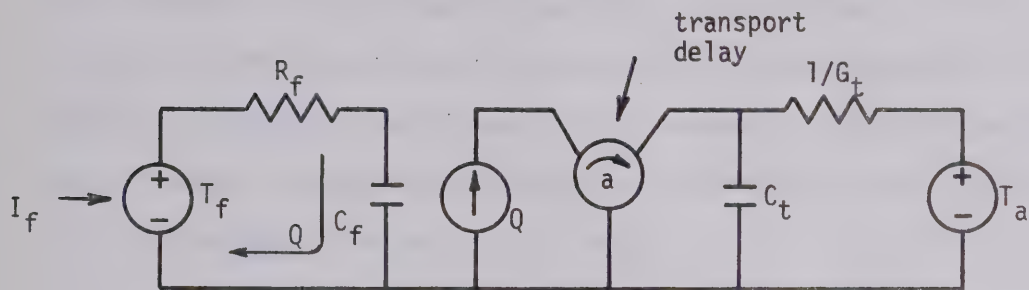


Fig. 2.6 Electrical analog network of the heating process.

From the behaviour of the thermal system, it was found that heating of the target required a considerably longer time than heating of the filament. Therefore from Fig. 2.6

$$R_t C_t = \frac{C_t}{G_t} \gg R_f C_f .$$

The dominant time constant of the thermal system is therefore $R_t C_t$ and the response to a step input will be largely affected by this time constant.

2.7.3 Approximation of the transfer function of the process

a) Heating

The transfer function of the process was estimated from a step response curve obtained by applying a step of input current to the filament and then recording the thermocouple emf output versus time by means of a Moseley Autograf Model 2D X-Y recorder. The responses for step filament current inputs between 3 - 4 amperes are shown in Fig. 2.7. The high voltage E_p was set at 1800 volts.

For the purpose of analysis of the step response curve, the filament current in the operating region was found to lie in the range between 2 - 3.5 amperes and mostly at 3-3.4 amperes. The step response for I_f at 3.4 amperes was selected as the most representative one in the whole controlled temperature range.

With $C(t)$ as the exponential output response of the thermal system, the logarithm of $|C(t)-C(\infty)| / |C(0)-C(\infty)|$ was plotted versus t as shown in Fig. 2.8¹⁴. The resulting plot (curve I of Fig. 2.8) behaves asymptotically as the straight line II with slope = .0438 and ordinate 2.2 at the origin. The nonlinearity in the first time interval shows that this thermal system is not a simple first order one but that it can be considered as such to a first approximation.

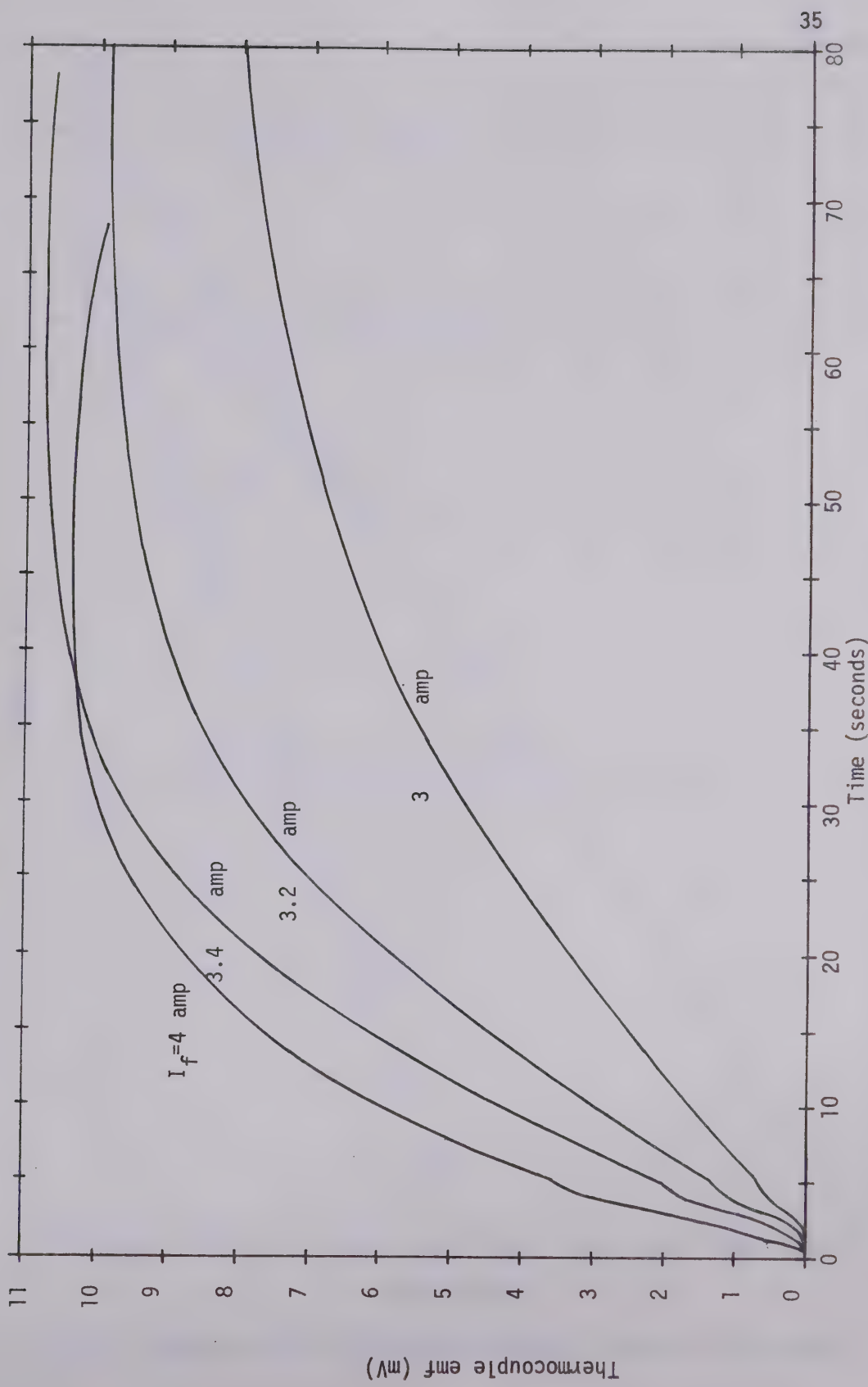


Fig. 2.7 Transient responses of the thermal system to step filament currents.

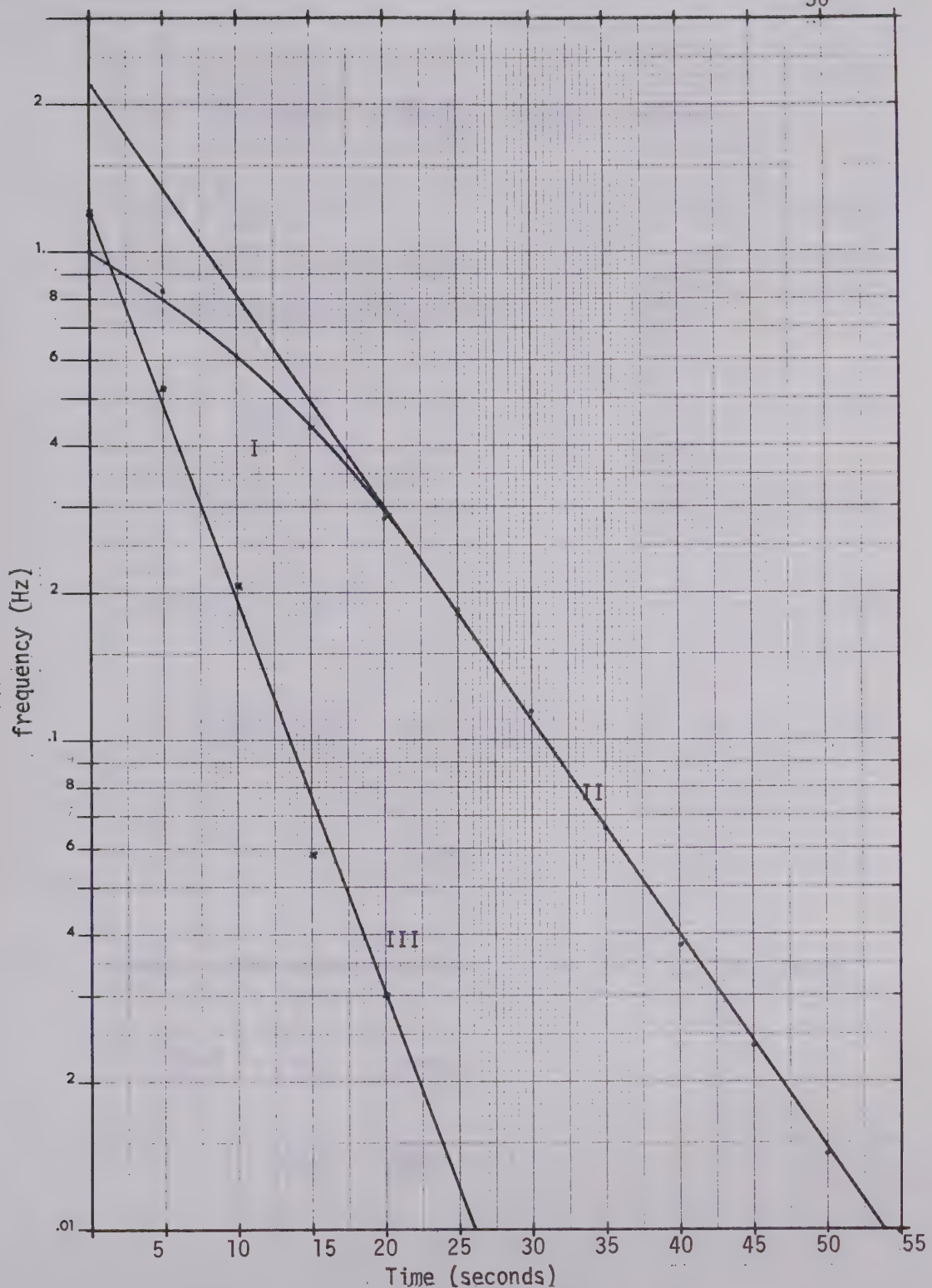


Fig. 2.8 Plotted curves for the determination of poles of the system.

For a first order system the transfer function is

$$G(s) = \frac{K}{\tau s + 1} \quad (2.30)$$

The step response of magnitude m is

$$C(s) = \frac{K}{\tau s + 1} \frac{m}{s} \quad (2.31)$$

$$C(t) = Km (1 - e^{-t/\tau}) \quad (2.32)$$

$$|C(t) - C(\infty)| = Km e^{-t/\tau} \quad (2.33)$$

$$\log \left[\frac{|C(t) - C(\infty)|}{|C(0) - C(\infty)|} \right] = \log \frac{|C(t) - C(\infty)|}{Km} = - \frac{t}{\tau} \log e \quad (2.34)$$

$$= \left(- \frac{\log e}{\tau} \right) t \quad (2.34)$$

This is the equation of the straight line II. This yields

$$- \frac{\log e}{\tau} = \text{slope} = - .0438.$$

$$\tau = \frac{\log e}{.0438} = \frac{.4343}{.0438} = 10.1$$

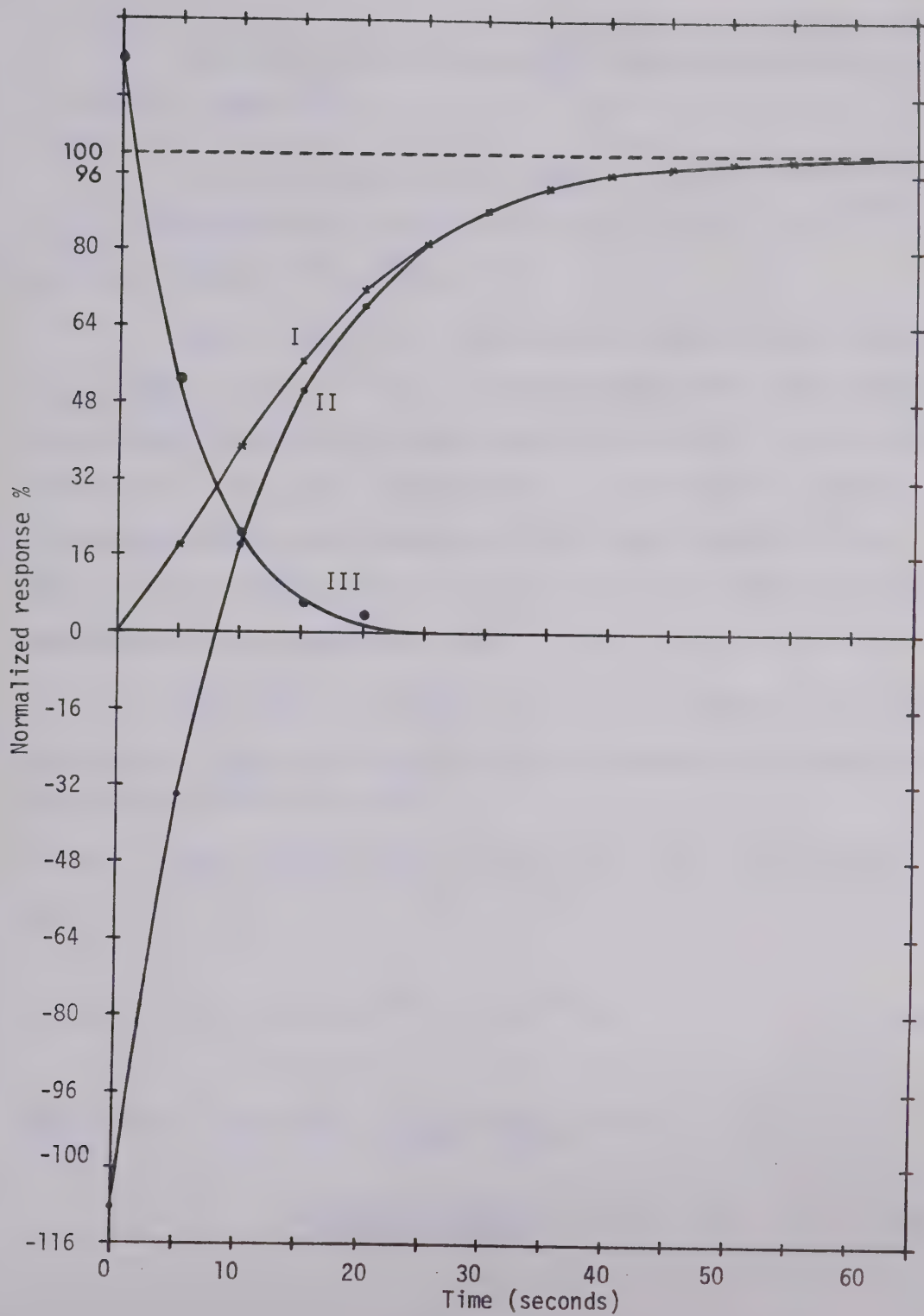


Fig. 2.9

Plot of curves I, II, III in linear scale.

This means that the function $\frac{C(t)}{Km}$ behaves asymptotically as $2.2e^{-t/10.1} = 2.2e^{-0.099t}$.

The chosen normalized step response $\left[= \frac{C(t)}{Km} \right]$ was redrawn in Fig. 2.9 together with the variation of the function $1 - 2.2e^{-0.099t}$, which was asymptotic to normalized $c(t)$.

Next the logarithm of the difference between curves I and II or $\log \left[\frac{C(t)}{Km} - (1-2.2e^{-0.099t}) \right]$ was plotted against time. The average curve through those points was approximated as a straight line as shown by curve III in Fig. 2.8. The deviation of points from the straight line may be caused by the nonlinearity of the system itself, or by inaccuracy in the procedure which relies entirely on the accuracy and the measurement of the step response $C(t)$.

Curve III has an ordinate at 1.2 which corresponds to a time constant of 5.5 secs. The straight line then represents the exponential function $1.2e^{-t/5.5} = 1.2e^{-0.182t}$.

Hence the approximate expression for the unit step response $C(t)$ is

$$C(t) = K(1-2.2e^{-0.099t} + 1.2e^{-0.182t}) \quad (2.35)$$

and that for $C(s) = K\left(\frac{1}{s} - \frac{2.2}{s+0.099} + \frac{1.2}{s+0.182}\right)$

$$= \frac{K(-.00014s + .018)}{s(s+0.099)(s+0.182)} \quad (2.36)$$

The negative numerator coefficient of s corresponds to a positive zero in the s plane; it should be neglected because its coefficient is much smaller than .018 and it is unlikely that this thermal system will have an unstable zero. This term, again, might arise from the inaccuracy in the procedure.

Thus the approximate normalized transfer function becomes:

$$\frac{G(s)}{K} = \frac{.018}{(s+.099)(s+.182)} \quad (2.37)$$

Once more it should be recalled that the position of the first pole is the more reliable one while that of the second pole is just an approximation of the combined effects of nonlinearities and the other pole contributed by the filament.

Theoretically the method so far described is applicable to a periodic system of any order but its use becomes inaccurate and unwieldy for higher order systems. In this thermal system the previous method cannot be relied upon to give more accurate results if additional poles are extracted from the step response.

b) Cooling

The equivalent electrical analog for cooling of the target can be drawn as in Fig. 2.10. Since the heat source is absent, the

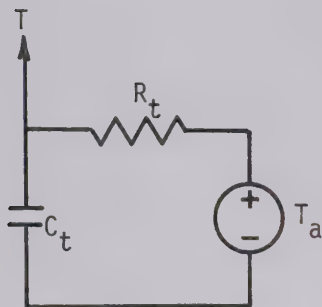


Fig. 2.10

Electrical analog for cooling process of the target.

current source Q must be disconnected and the previously charged C_t will discharge through R_t only. The linearized expression for cooling is simply an exponential decay asymptotic to the final temperature:

$$T = (T_0 - T_a) e^{-t/\tau} + T_a \quad (2.38)$$

where T_0 is the initial temperature at $t = 0$

T_a = final (ambient) temperature

τ = time constant

The time constant τ can be determined directly from the recorded cooling curve by drawing a tangent line at $t = 0$.

This line will intersect the ambient temperature line at $t = T$ as shown in Fig. 2.11. From measurement the average T is 12.38 sec. The dominant pole therefore is at $s = -0.081$ in the complex plane. This value shows close agreement (within the experimental error) with the value of the first pole in equation 2.37. The most probable value was chosen

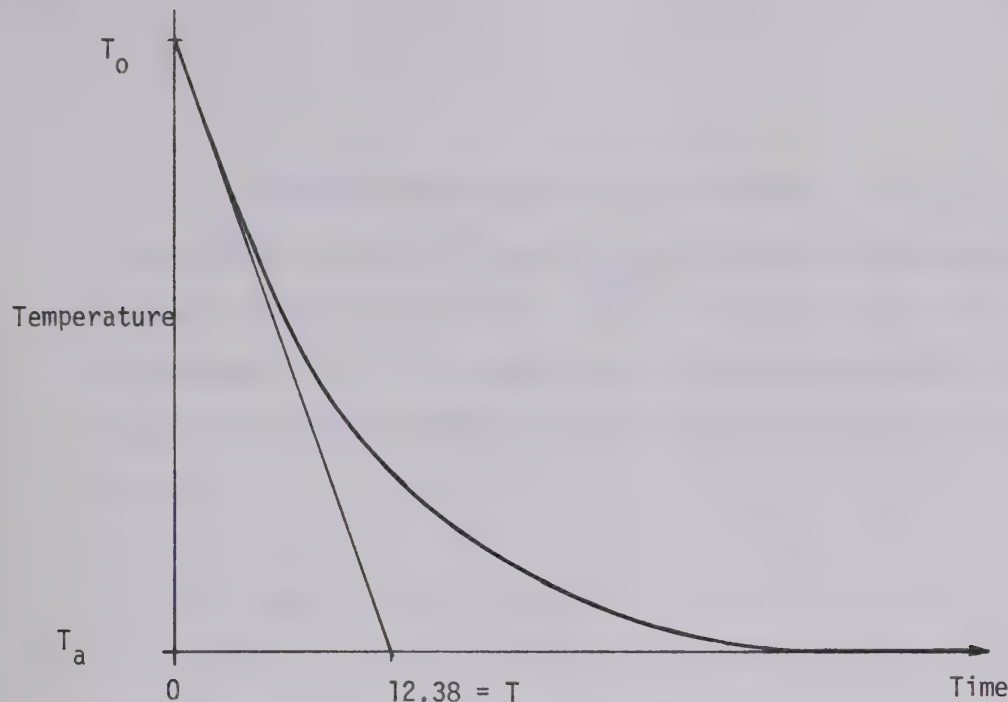


Fig. 2.11

Cooling curve of the target
(arbitrary scale).

as $s = -0.09$.

c) Steady state gain

To find the steady state gain between the unit step input current I_f and the output temperature T , Fig. 2.5 is analysed. If $I_f = 1$ ampere is applied to the filament, the steady state temperature will be

$$T(t \rightarrow \infty) = T_a + \lim_{s \rightarrow 0} s \cdot \frac{A+B}{\tau_f s + 1} \cdot \frac{R_t e^{-as}}{\tau_s + 1} \cdot \frac{1}{s} \quad (2.39)$$

$$= T_a + (A+B) R_t \quad (2.40)$$

where $R_t = 1/G_t$.

Therefore the steady state gain $(A+B)R_t = T(t \rightarrow \infty) - T_a$.

If the final temperature is measured and the ambient temperature is known then the steady state gain $\frac{T(t \rightarrow \infty) - T_a}{I_f}$ for any value of I_f can be calculated. If it is assumed that the thermocouple emf is directly proportional to the difference between target and ambient temperatures, i.e.

$$T(t) - T_a = k V_{th}(t) \quad (2.41)$$

where $V_{th}(t)$ is thermocouple emf (mV) at time t ,

and k is a constant,

$$\text{then } (A+B)R_t = \frac{k V_{th}(t \rightarrow \infty)}{I_f} \quad (2.42)$$

Hence the steady state state gain between V_{th} and I_f can be found as:

$$\frac{V_{th}(t \rightarrow \infty)}{I_f} = \frac{(A+B)R_t}{k} \quad (2.43)$$

This steady state gain can change depending upon I_f because of the nonlinear relationship between bombarding electron current, radiant heat and the filament current. The transfer function of the thermal system can be rewritten as

$$\frac{V_{th}}{I_f} = \frac{(A+B)R_t}{k} \times \frac{.0162 \times e^{-as}}{(s+.09)(s+.18)} \quad (2.44)$$

To find the steady state gain between the filament current in amperes and the thermocouple emf in millivolts, different inputs I_f were applied to the filament. V_{th} was then recorded in each case after the transients had died out ($t > 5\tau$). One problem inherent in these measurements was that the thermocouple emf dropped down gradually as the time increased. This created large errors in measuring the steady state temperature. The effect was evident when high filament current was used. This phenomenon is likely caused by:

- 1) The increase in reference junction temperature due to heat radiated and conducted from the process.
- 2) Secondary electrons and positive ions being released from the target more rapidly at high temperatures.

The second cause listed above was evident from the gradual decrease in electron bombarding current as measured over a long time interval. Working at low current and taking data only once in a long time could reduce this error especially with respect to the first cause. A decrease in the electron current, however seemed unavoidable.

The relationship between the electron current and the filament current as given by equation 2.4 is rewritten as

$$I_p = a I_f^n \quad (2.4)$$

If each electron that comes to rest in the target delivers equal energy to the target and all its kinetic energy is completely converted to heat, then the power converted to heat equals:

$$q = E_p I_p = a E_p I_f^n \quad (2.45)$$

An equilibrium state will be established when the rate of heat input equals the rate of heat loss. Let Q_s be the net amount of heat (in joules) delivered to the target to raise its temperature from T_a to T_s at steady state. Thus, the increase in temperature is

$$\Delta T = T_s - T_a = \frac{Q_s}{MC} = \frac{b(a E_p I_f^n) t_s}{MC} \quad ^\circ C \quad (2.46)$$

where $b < 1$ because of heat loss,

t_s = settling time which is assumed to be constant,

M, C = mass and specific heat of the target.

Equation 2.46 can be reduced to

$$\Delta T = \alpha E_p I_f^n \quad (2.47)$$

where $\alpha = \frac{ab t_s}{MC} = \text{a constant.}$

Equation 2.41 is rewritten as

$$V_{th} = \frac{1}{k} (T - T_a) \text{ mV.}$$

$$\text{At } t_s, V_{th}(t_s) = \frac{\alpha}{k} E_p I_f^n$$

If E_p is kept constant, then the thermocouple emf (V_{th}) and the filament current (I_f) are related in a simple manner by

$$V_{th}(t_s) = \beta I_f^n \quad (2.48)$$

where $V_{th}(t_s)$ is in mV,

I_f is in amperes,

β is a constant.

Taking the logarithm of both sides of (2.48) gives

$$\log V_{th}(t_s) = \log \beta + n \log I_f \quad (2.49)$$

It is expected that a log - log plot between $V_{th}(t_s)$ and I_f should be a straight line with slope n and ordinate β . However, the nonlinear effects from radiant heat and from the electron bombarding process itself will cause deviation from the linear relationship as obtained by (2.49). The resulting plots of data presented in Fig. 2.12 show that this nonlinearity is large for low values of I_f . All points have to be

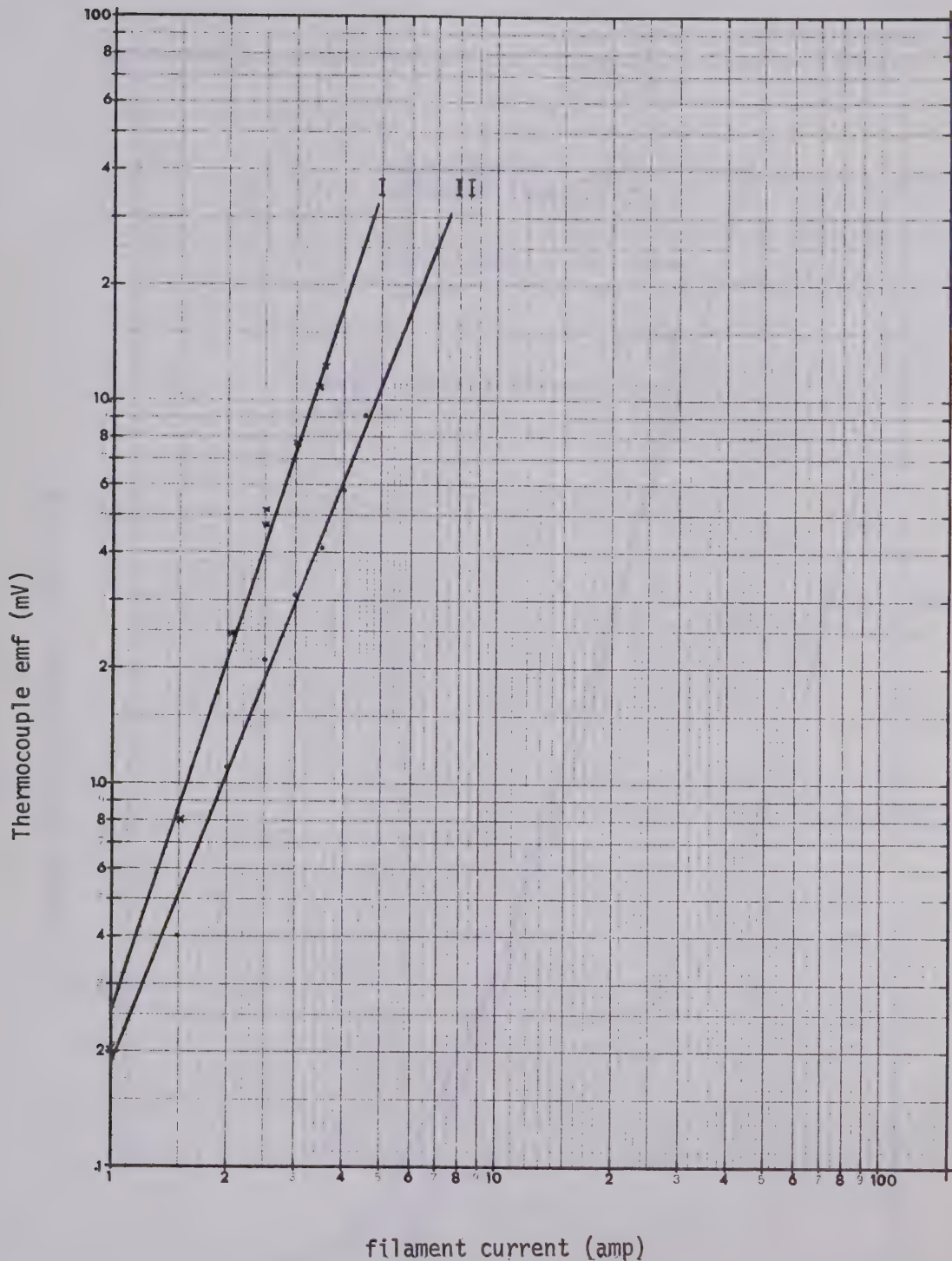
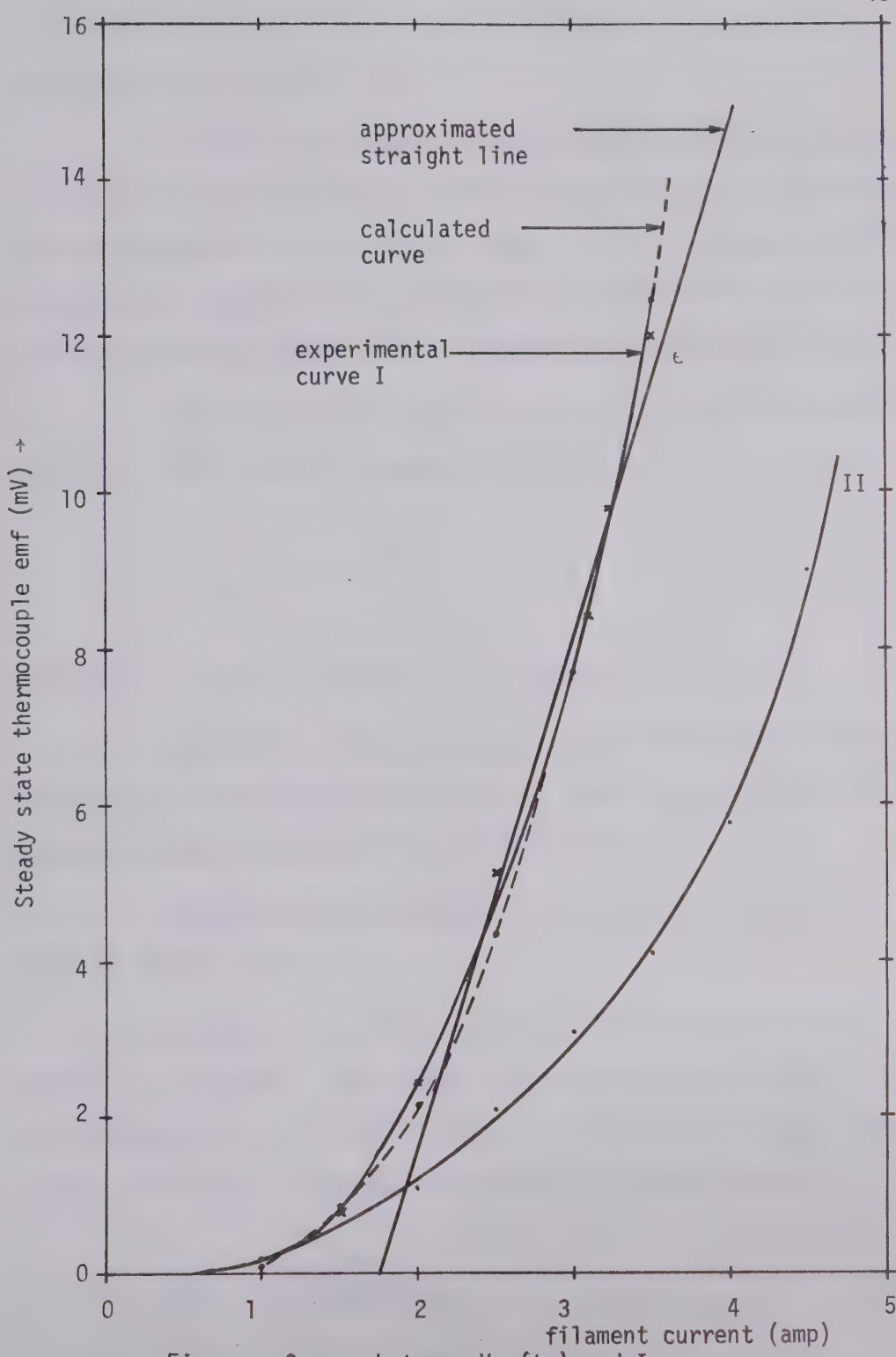


Fig. 2.12

Log-Log plot between $V_{th}(t_s)$ and I_f .



averaged by the straight line I.

The other set of data obtained from repeating the same procedure as discussed above was plotted as the straight line II to show the effect of deteriorated emissivity of the filament. This is because thorium can be completely evaporated from the tungsten filament after a few heating cycles at currents of more than 3.5 amperes over extended periods of time.

The straight line I has an ordinate at .25 and a slope of $\tan 72.3^\circ = 3.72$. Hence, from equation 2.48

$$V_{th}(t_s) = .25 I_f^{3.12} \quad (2.50)$$

where V_{th} is in millivolts and I_f is in amperes.

The initial data of $V_{th}(t_s)$, I_f and those calculated from equation 2.50 were plotted in Fig. 2.13. These two curves show good agreement between measured and calculated values.

The block diagram representing the thermal system can be drawn as in Fig. 2.14.

As mentioned earlier, the nominal operating values of I_f lie between 2-3.5 amperes. This region of the curve shown in Fig. 2.13 can be approximated as a straight line having slope $\frac{14.7}{4-1.75} = \frac{14.7}{2.25} = 6.53$ mV/amp. Therefore, the transfer function can be simplified to

$$\frac{V_{th}}{I_f} = \frac{.106 e^{-sa}}{(s+.09)(s+.18)} \quad (2.51)$$

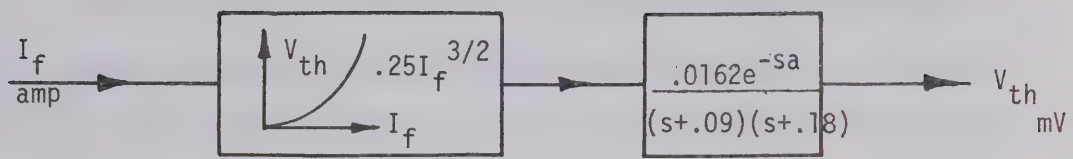


Fig. 2.14

The time delay "a" mentioned previously is also inserted in the final equation (2.51) to complete the transfer function but cannot be determined by the previous method. The frequency response method, which includes this effect, will be used to analyse the system as discussed in Chapter IV.

CHAPTER III

CONSTRUCTION OF CONTROL SYSTEM

3.1 Introduction

This chapter will describe the proposed electron bombardment control system. Details of control circuits and other system components are given. The transfer function of the control circuits are estimated and later the block diagram of the complete system is drawn.

Section 3.2 presents the schematic diagram of the proposed control system.

Section 3.3 determines the type of the required controller for the application.

Section 3.4 describes the control circuit details.

Section 3.5 estimates the form of the transfer function of the control circuits.

In section 3.6, the block diagram form of the complete control system is given.

3.2 Schematic Diagram of the Control System

A control system was constructed to control the filament current for the purpose of heating the target in a linear manner as required. The simplified schematic diagram is shown in Fig. 3.1.

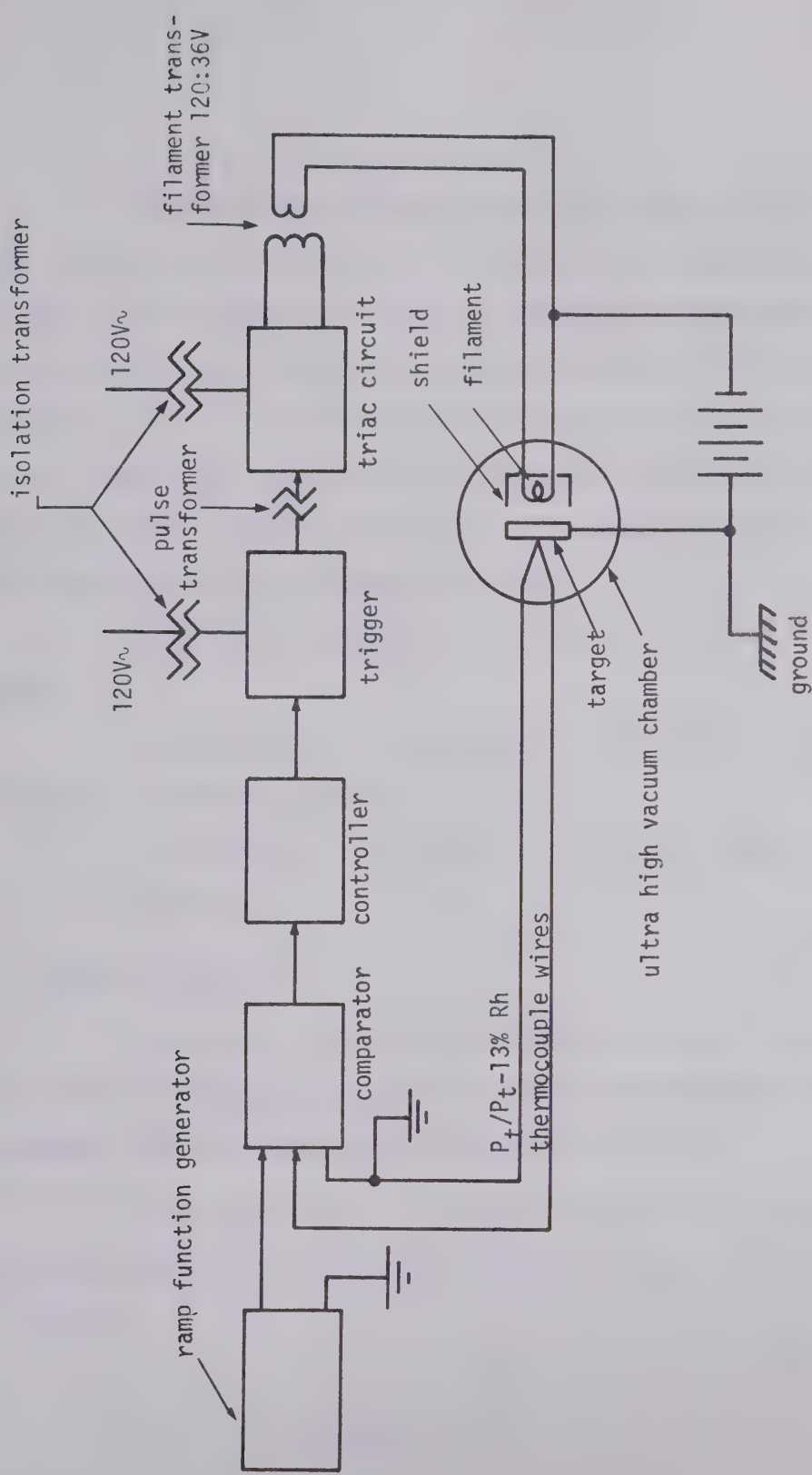


Fig. 3.1 Schematic diagram of temperature control system.

The potential difference between the target and the filament must be maintained at about 2 KV. Since the control system must supply AC power to the filament in response to thermocouple measurement of target temperature, high voltage isolation of parts of the control system is required. To eliminate the difficulties of floating the entire control system, the positive side of the high voltage supply was grounded and the filament power supply at the negative side was floated. This offers potential advantages as follows:

- a) Safety and convenience of using and adjusting the control system.
- b) Elimination of inaccuracy and difficulties resulting from electrical breakdown or leakage.
- c) A reduction in the number of interfaces between high and low voltage elements.

3.3 Type of Controller

The transfer function of the thermal system as determined can be written as $\frac{b e^{-as}}{(s+0.09)(s+0.18)}$ where a and b are constants. The control system may also be simplified and redrawn as in Fig. 3.2.

If the controller is a proportional controller having gain K, the steady state error of the output temperature with a unit ramp input is given by

$$e_{ss} = \lim_{s \rightarrow 0} \frac{s}{1+G(s)H(s)} \quad \frac{1}{s^2} \quad (3.1)$$

$$= \lim_{s \rightarrow 0} \frac{1}{s} \frac{1}{1 + \frac{K_b e^{-as}}{(s+0.09)(s+0.18)}} \quad (3.2)$$

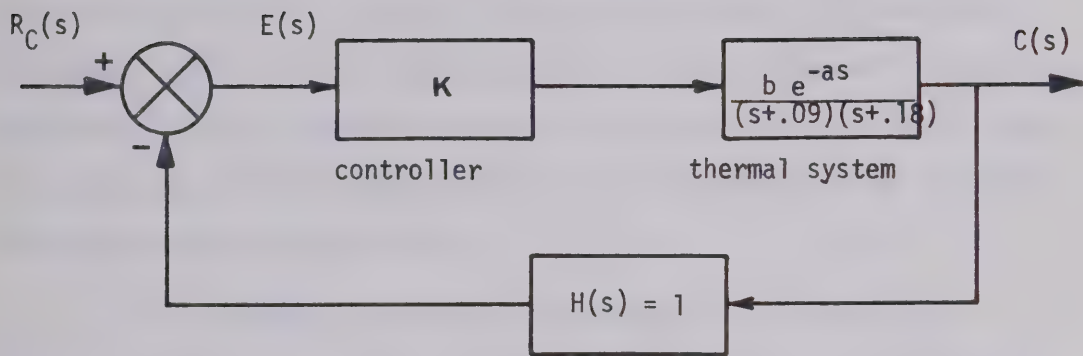


Fig. 3.2

Simplified diagram of control system.

which becomes infinite when the time increases. Generally speaking, if the controller does not include a free integrator to contribute at least one pole at the origin, the output temperature of the element will not change linearly with time but will gradually deviate from the ramp function input. The controller must, therefore, contain a free integrator with transfer function $\frac{1}{s}$ so that the system will be at least type one and its output can follow a ramp input with a finite error. In this

thermal system a straight integral controller only is not applicable because the system will become unstable even at very low gains. The s-plane locations of the closed-loop poles of this system with an integral controller included are very close to the imaginary axis. Their locations change depending on the value of the loop gain K . By slightly increasing gain K , two closed loop poles of the system will move into the right half s plane and the transient response to a constant magnitude input will increase monotonically or oscillate with increasing amplitude. Such a system is unstable. The stability of a linear system is a property of the system itself and does not depend on the input or driving function of the system.

To increase the stability and improve the response of the system it is desirable to modify the controller to a proportional plus integral type having the transfer function $K_p(1 + \frac{1}{T_i s})$ where K_p and $\frac{1}{T_i}$ are gain constants called proportional gain and integral gain respectively. This controller will create a negative real axis zero having a position determined by the value of T_i . The presence of a negative real axis zero will pull the locus of the poles towards itself; hence, the system will be more stable over a wide range of gains K_p . However, the actual system may be more complex and have additional poles from other components in the control loop. To obtain enough stability the loop gain may have to be carefully adjusted. If the system performance is not satisfactory after the adjustment of gains, compensation networks or derivative gain may have to be included.

The following section will deal with the details of the control circuits to obtain the proportional plus integral control action of the filament current as outlined in Fig. 3.1. Approximate transfer functions of various parts are also given.

3.4 Circuit Details

Economy, simplicity and reliability were guiding considerations in the construction of this control system.

3.4.1 Ramp function generator

Several dc amplifier circuits comprising a typical operational amplifier μ A709 modified with a FET differential input stage using two FET's 2N3819 which had very similar characteristics were built and used as an integrator with a gain of $1/RC$ s of about $.02/s$. The results were not satisfactory however, because the gate bias current was very high producing high rate drifts which were non-adjustable. This also made the circuit insensitive to small inputs. To avoid these drift problems, a mechanical integrator was built by connecting a 10 turn Helipot precision potentiometer (having a resistance of $10K \pm 3\%$ and a linearity tolerance of only 0.250%) across a low voltage source and rotating this potentiometer by means of a small Rustrak synchronous motor at a constant speed of 2 rpm. The complete circuit is shown in Fig. 3.3.

3.4.2 Comparator

Many problems may be eliminated if the comparator is a bridge circuit having the prescribed ramp voltage generator as one side

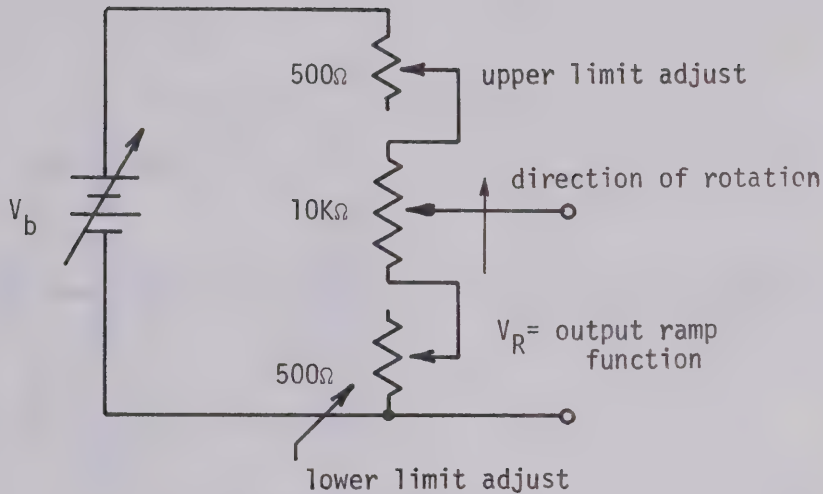


Fig. 3.3

Ramp function generator.

of a bridge circuit and a linear precision potentiometer rotating precisely according to the output signal as the other side. The error voltage can then be taken from the two sliders of the potentiometers. An available Electronik 16 Lab Recorder from Honeywell had an accuracy of $\pm \frac{1}{4}\%$ of full scale, a dead band of 0.1% of span and a travel speed of only 0.2 sec for full scale deflection. The above mentioned scheme was implemented satisfactorily by attaching a 1 turn, 10K Helipot precision potentiometer (having linear tolerance of .150% and resistance tolerance of 1%) to the rotating pen

shaft of the recorder and by connecting the two potentiometers together as shown in Fig. 3.4.

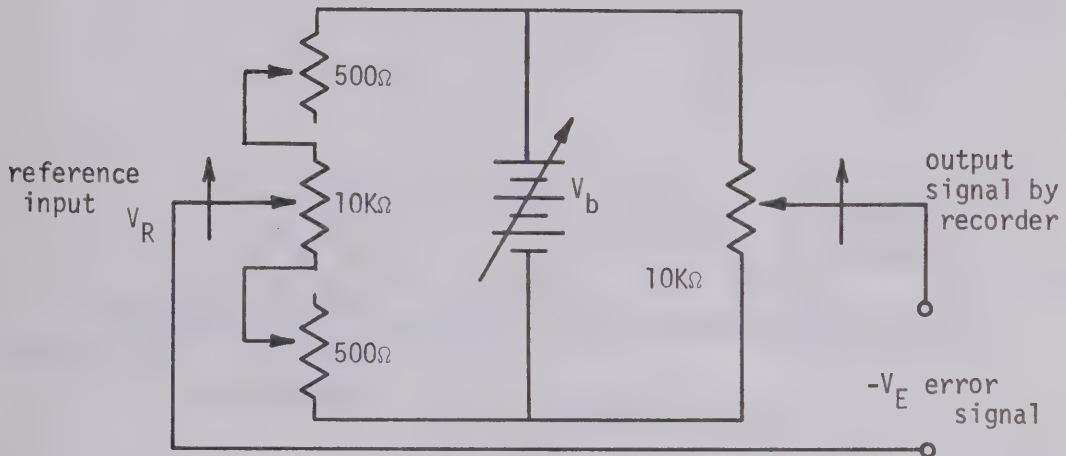


Fig. 3.4
Comparing bridge circuit.

A self contained precision bridge circuit capable of comparing the input ramp function with the desired output signal was thus formed. The position of the slider of the right arm of the bridge was determined by the controlled temperature of the target when the input to the recorder was the thermocouple emf. The full scale input of the recorder was about 3.4 mV and a potentiometer had to be used to attenuate the maximum thermocouple emf down to this value. By varying this attenuation the maximum controlled temperature and the speed of temperature sweep could

also be varied. The speed of the temperature sweep, however, could only be increased, i.e., the sweeping period would be 5 minutes or less.

This procedure is shown in Fig. 3.5.

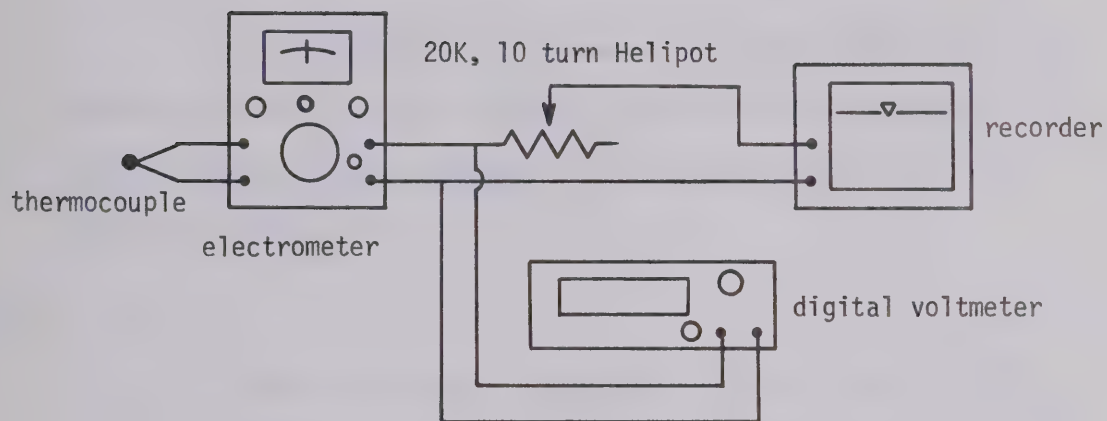


Fig. 3.5

Instrument setup for measuring and attenuating thermocouple emf.

The Keithley Model 600B Electrometer has excellent zero stability and was used as both a thermocouple emf indicator and as a unity gain buffer amplifier. Its zero drift was less than 2 millivolts per 24 hours, less than 200 microvolts per $^{\circ}\text{C}$, after 30 minutes warm up. The input impedance was greater than 10^{14} ohms and the output impedance was 910 ohms.

Thus, the electrometer could be used as an isolation amplifier to isolate the thermocouple from the rest of the circuit. A 20 K 10 turn Helipot potentiometer was placed in series with the recorder to attenuate the thermocouple emf down to less than 3.4 millivolts at the input of the recorder. A digital multimeter, DANA Model 3800 was also connected across the output of the electrometer to facilitate reading of the thermocouple emf.

The attenuating potentiometer inserted in the position as shown was found to be the simplest and most efficient method of attenuating when the arrangement of the recorder input network is considered (Fig. 3.6).

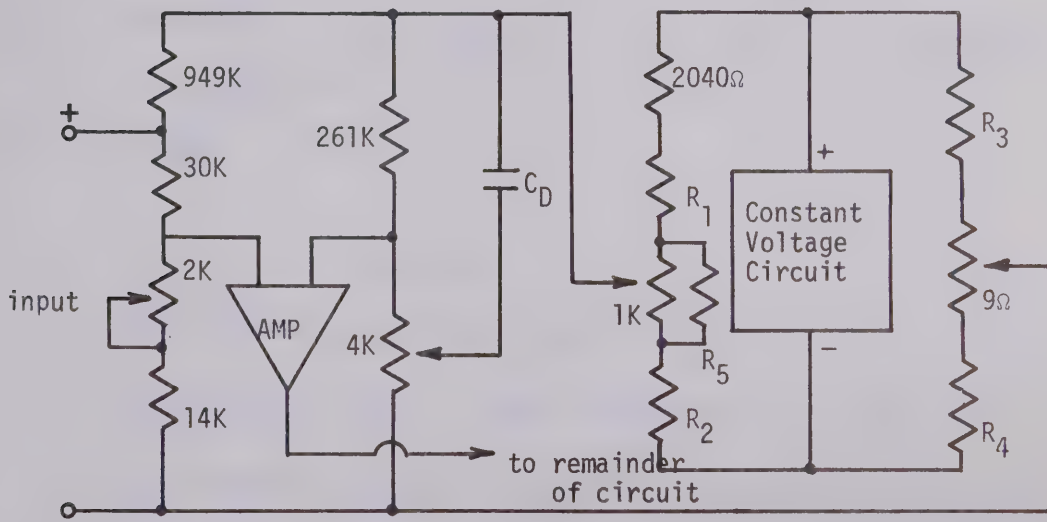


Fig. 3.6

Input network of the recorder.

3.4.3 The proportional plus integral controller

The integral gain may be varied manually by changing $\frac{1}{T_i}$ to $\frac{K_1}{T_i}$ where K_1 is a variable gain. The required transfer function of the controller is then changed to $\frac{K_1}{T_i s} + K_2$. This was simulated as shown in Fig. 3.7.

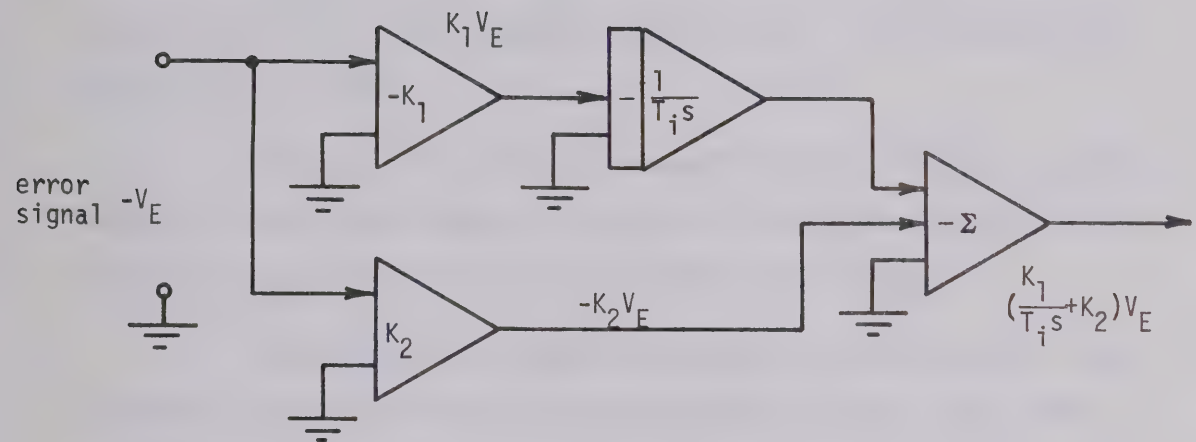


Fig. 3.7

Simulation of the transfer function $\frac{K_1}{T_i s} + K_2$.

The circuit details of each function are as follows.

a) Amplifiers of gains $-K_1$ and K_2

These are two temperature controlled differential dc amplifiers having high gains ($-K_1, K_2$) and very low drifts.^{15,16} In this technique, a

monolithic transistor pair (μ A726) is stabilized at a temperature above ambient by an integrated circuit heater. As the ambient temperature changes, the power fed to the heater is changed to maintain the temperature of the differential pair at a constant level. Since the temperature of the differential pair does not change appreciably the effective input voltage drift is considerably reduced. Because the device is constructed on a single silicon chip with only small mass involved the chip temperature stabilizes within a few seconds. When stabilized, the input offset voltage drift is only about $0.2 \mu\text{V}/^\circ\text{C}$, and the input offset current drift is reduced to about $10 \text{ pA}/^\circ\text{C}$. The long term drift is about $5.0 \mu\text{V}/\text{week}$.

Figs.3.8 and 3.9 are the schematics of the inverting amplifier of gain K_1 and the noninverting amplifier of gain K_2 respectively. The design of these circuits^{16,17} can be summarized as follows.

The differential stages were designed to be operated at low collector current levels to minimize input bias current, input offset current and their drifts. The collector current was set at $100 \mu\text{A}$ per transistor. For this collector current, h_{FE} was 400. Since the two transistors are matched, the power supply must deliver the total current of $200 \mu\text{A}$ to both transistors, assuming that $I_c \approx I_E$. A constant current source comprising a matched pair transistor 2N2060A was used in the emitter circuit; this significantly improved the common mode rejection ratio (CMRR) which is proportional to the high output resistance R_o of the current source.

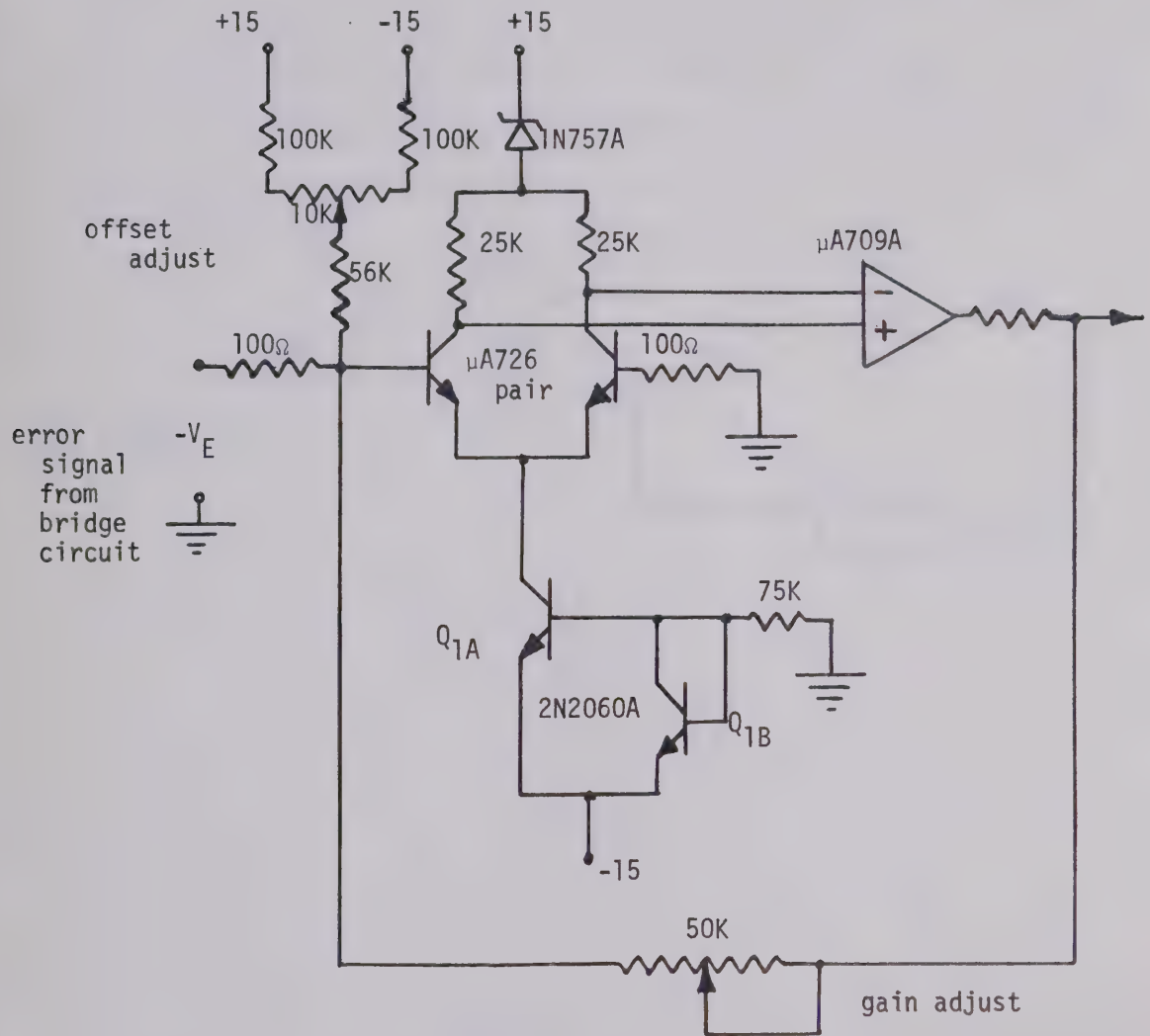


Fig. 3.8

Low drift dc amplifier of inverted gain K_1 .

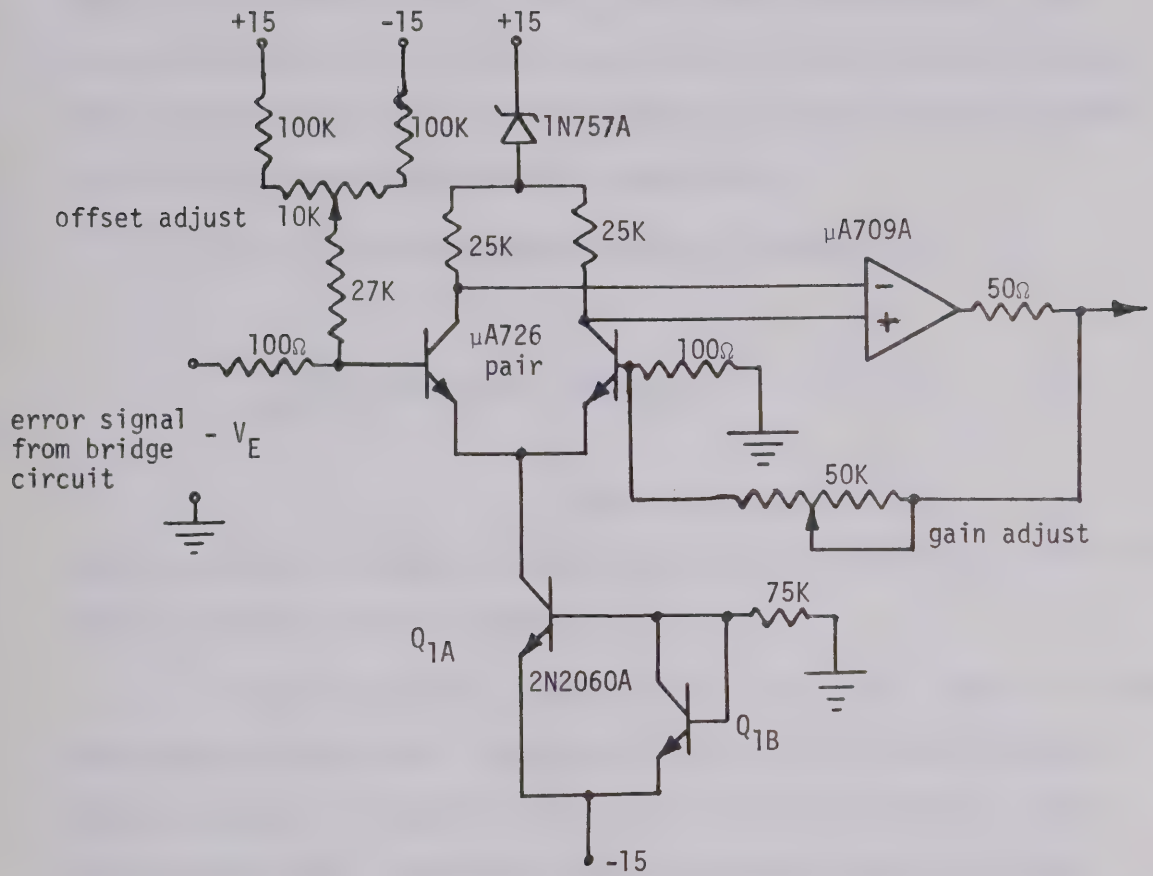


Fig. 3.9

Low drift dc amplifier of non inverted

gain K_2 .

For the circuit of the constant current source as shown, the bases of both transistors Q_{1A} and Q_{1B} are at the same potential. When the transistors are located very close together on the same chip (matched pair), their properties will be very similar and their collector currents will tend to be equal regardless of temperature.

The Q_{1B} collector current may be calculated by

$$\frac{15 - V_{BE}}{75K} = \frac{15 - 0.61}{75K} = \frac{14.39}{75} \text{ mA}$$

$\approx 200 \mu\text{A}$ as required.

The Q_{1B} collector current is largely independent of temperature and therefore so is the collector current of Q_{1A} .

Once the collector current levels were chosen, load resistances determined voltage biases. Collector resistors were chosen to provide the desired gain and output dc level within the bias limits for common mode voltage swing. The chosen value of collector resistor (R_C) was $25\text{K}\Omega$. Common mode gain which can be approximated by $-\frac{R_C}{2R_O}$ (where R_O = output resistance of the current source) therefore should be very low. The desired bias was achieved by using a zener diode 1N757A to reduce the power supply from +15 volts to +6 volts. For simplicity, the temperature controlling circuits and pin connections to the integrated circuits are not shown.

The input voltage offsets due to unequal base-emitter voltages in the input transistor pair remained finite for these two circuits and could not be tolerated in the experiments. A normal method of balancing these dc offsets by using a small trimming potentiometer with a resistor network is shown in each figure. The drift from variation in the voltage offset due to temperature variation was successfully minimized and that due to the supply variation could not be noticed.

b) Integrator

The integrator circuit built from a single operational amplifier MC1439G is shown in Fig. 3.10. The RESET switch was used to set the initial condition of the capacitor equal to zero ($V_o = 0$ at $t = 0$). Adjusting of the dc balancing potentiometer to obtain minimum drift when applying zero error input signal to the control circuit would give the optimum performance.

When considering the dc offset and bias current of the operational amplifier the output of the integrator consists of two components;¹⁷ the integrated signal term and a group of error terms, i.e.,

$$e_o = -\frac{1}{RC} \int e_i \, dt + \left[\frac{1}{RC} \int V_{os} \, dt + \frac{1}{C} \int I_B \, dt + V_{os} \right] \quad (3.3)$$

where V_{os} is the input offset voltage,

I_B is the input bias current.

In this equation only V_{os} and I_B are considered as causes of integrator error. The maximum voltage drift rate due to these offsets can be found by differentiating the above equation,

$$\frac{\Delta e_o}{\Delta t} = \left| \frac{V_{os}}{RC} \right| + \left| \frac{I_B}{C} \right| \quad (3.4)$$

For the MC1439G operational amplifier¹⁸ the typical values of V_{os} and I_B at $T_a = 25^\circ\text{C}$ are 2.0 mV and 0.2 μA respectively. Therefore the typical maximum error is

$$\left(\frac{\Delta e_o}{\Delta t} \right)_{\max} = \frac{2\text{mV}}{RC} + \frac{0.2\mu\text{A}}{C} \quad (3.5)$$

For the value $R = 7\text{M}$ and $C = 10 \mu\text{f}$ the maximum error is

$$\left(\frac{\Delta e_o}{\Delta t} \right)_{\max} = 20.029 \text{ mV/sec} \quad (3.6)$$

which is very high. Under actual operating conditions there is the possibility that V_{os} and I_B will be greater than the typical values indicated due to other parameter variations such as temperature and component aging. The error component due to bias current was minimized by increasing the capacitance of the feedback element. The capacitor used in the circuit was a mylar 10 μf capacitor 100 WV.

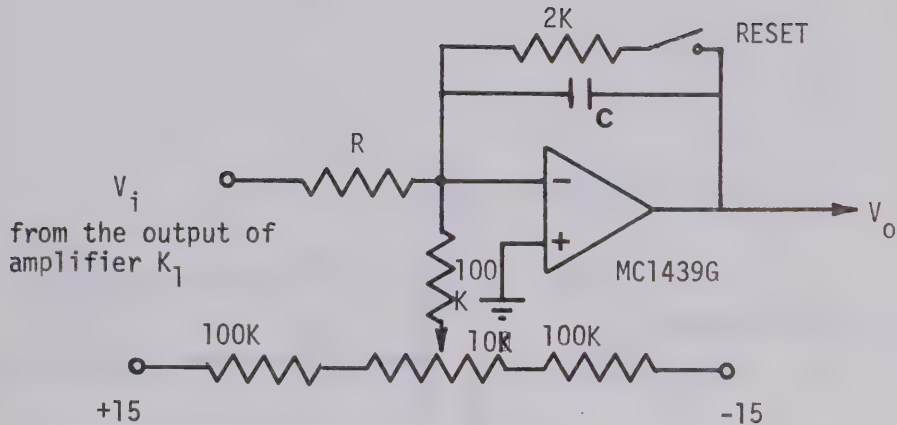


Fig. 3.10

Integrator.

The long time constant and the desired accuracy required many changes in the circuit. The dielectric of the feedback capacitor should be polystyrene or teflon which has low leakage current compared to the input bias current.¹⁷ The circuit may be modified by employing a matched pair of insulated gate FET's as a differential input stage followed by another operational amplifier with higher performance.

c) Summing amplifier.¹⁷

The outputs of the integrator and the K_2 amplifier were finally connected to the input of a summing amplifier. The summing amplifier consisted of a single MC1741CP internally compensated operational

amplifier¹⁹ set at unity gain. The circuit is shown in Fig. 3.11.

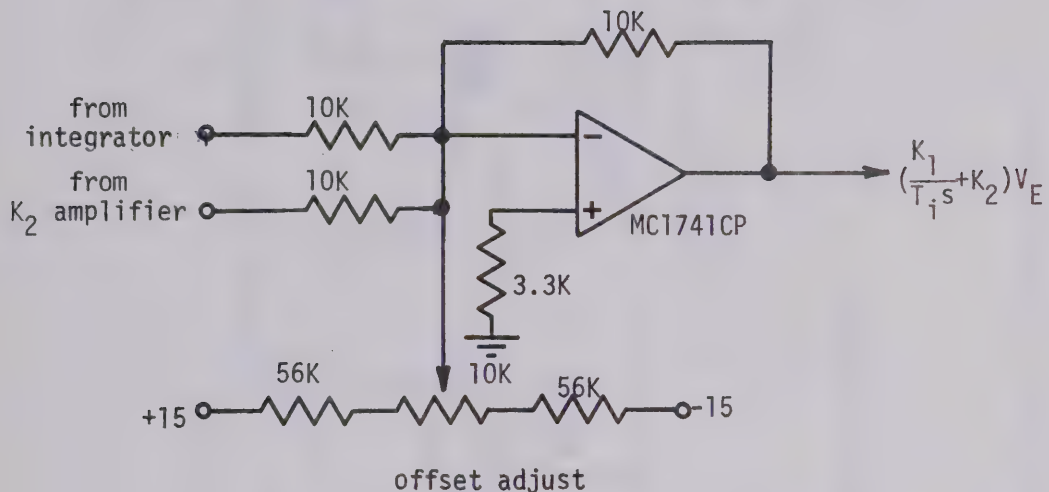


Fig. 3.11

Summing amplifier.

3.4.4 Trigger and triac circuits²⁰

The basic function of the trigger circuit is to generate the pulse signal to trigger the thyristor (SCR or triac) from the off-state to the on-state. The position of the pulse signal on a half cycle of the supply load voltage depends on the magnitude of the input control signal to the trigger circuit. Once triggered, the thyristor will remain conducting for the rest of that half cycle. The average power to the load

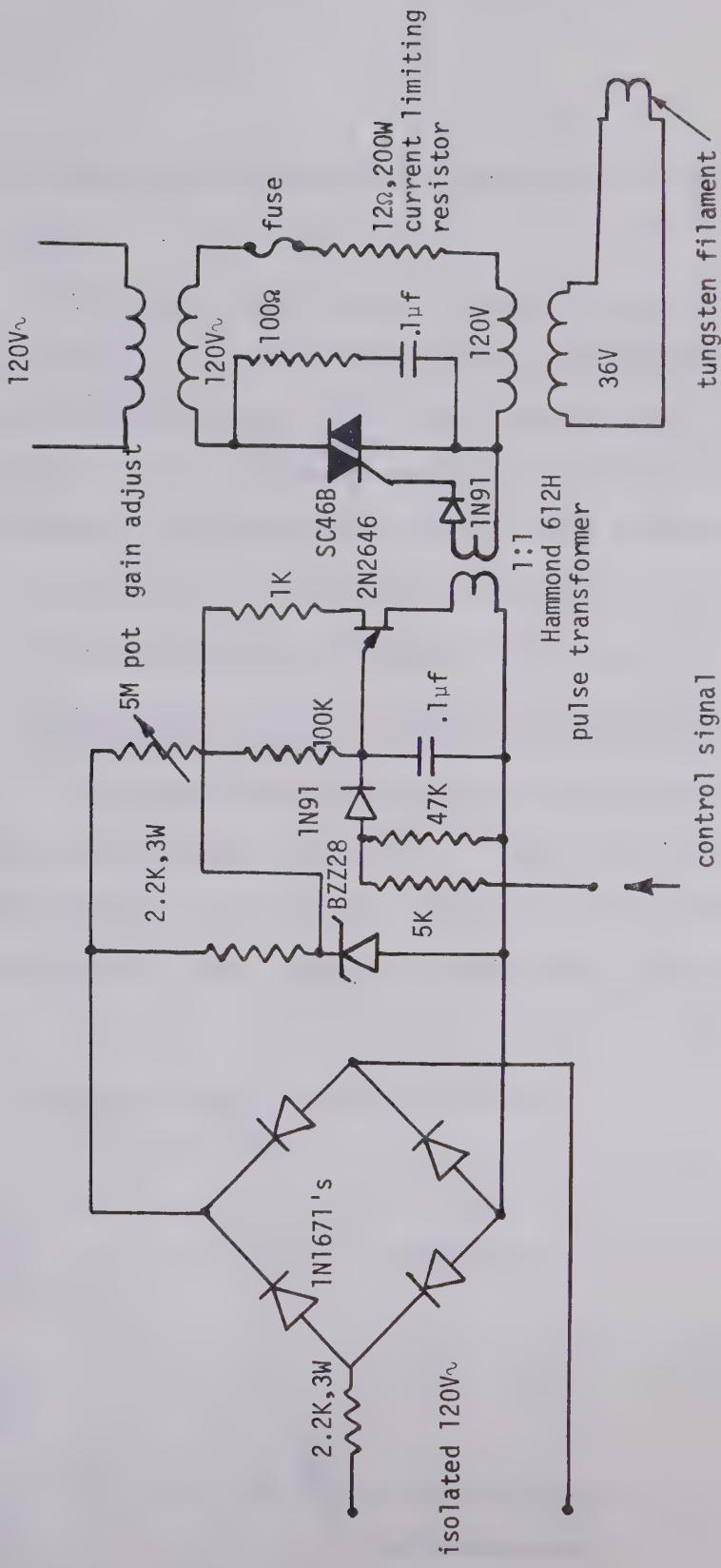


Fig. 3.12

Trigger and triac circuits for controlling of filament current.

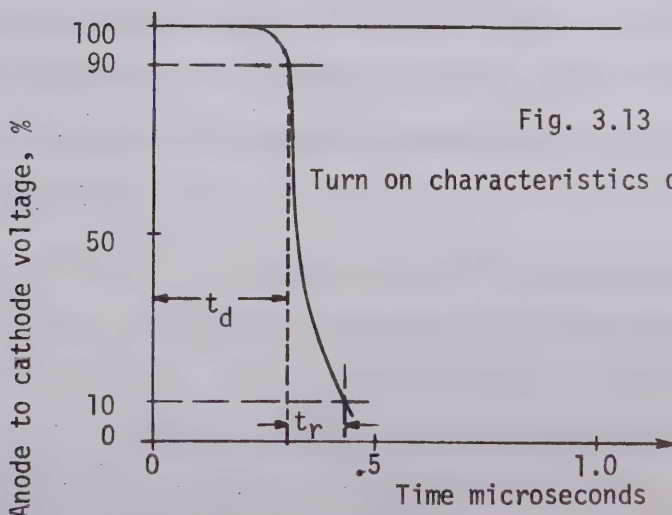
can thus be controlled efficiently by controlling the conduction period of the ac wave.

The trigger circuit used in this application utilized a 2N2646 unijunction transistor (UJT) operated as a relaxation oscillator.²⁰ The ramp and pedestal control²⁰ was later adapted to the circuit. The required thyristor type was determined by the current requirement for filament heating. The circuit that was built used a GESC46B triac capable of delivering 10 amperes of maximum current.

The complete circuit is shown in Fig. 3.12.

The characteristics of the trigger and triac circuits

In the phase control (conduction period control) process there is a time delay in turning on the SCR (or triac) and the percent anode to cathode voltage is decreased as a function of time following the application of the trigger signal. The delay time t_d is shown in Fig. 3.13.²⁰



and defined as the time between the 10% point of the leading edge of the gate current pulse and the 10% point of the anode voltage waveform. The delay time decreases as the amplitude of the gate current pulse is increased, but approaches a minimum value of 0.2 to 0.5 μ sec. Rise time t_r is defined as the time required for the anode voltage to drop from 90% of the initial value to 10%. Total turn on time is defined as $t_{on} = t_d + t_r$ and a typical value is 3 μ sec.

In the present case the transformer contributes an inductive component to the load. This inductance may affect the shape of the current waveforms, delay characteristics and commutation (turn off process) interval. As in the L R circuit the transient current is

$$i = \frac{V}{R} \left(1 - e^{-\frac{R}{L}t} \right) \quad (3.7)$$

Higher $\frac{L}{R} = \tau$ will slow the load current rise time, depress the peak currents and widen the conduction interval. The last effect is the result of inductive voltage in the load circuit. As the delay angle is increased the inductive voltage increases. This additional voltage allows the thyristor to conduct longer than the corresponding thyristor in a resistive circuit.

A small time delay also exists in the phase control process itself. This is the time required for the capacitor in the UJT circuit

to be charged up to the triggering voltage of the UJT emitter. This time delay is governed by the time constant $\approx RC$ in the UJT circuit and the magnitude of the control signal.

The most significant time delay occurring in the control process is from the trigger process. This is explained by the waveform in Fig. 3.14.

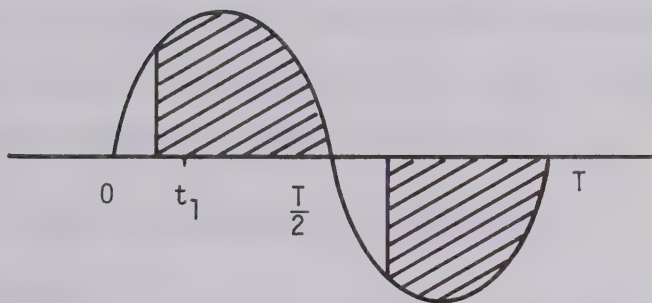


Fig. 3.14

Load voltage waveform.

Suppose that the first half cycle has not been turned on. If at time t_1 a pulse is applied to the gate of the triac, the latter turns on after a finite time as previously described. Suppose now that half cycle has then been partially turned on as shown. Then a next trigger signal originating at t_1 has to wait at least $\frac{T}{2} - t_1$ seconds to turn on the next half cycle, corresponding to the position of the trigger signal. This time delay is not constant but it will vary between

0 and $\frac{1}{2f}$ or ≈ 8 milli seconds where f is the power line frequency.

This time delay is large enough to create instability or severe nonlinearity in the control system with a quickly-responding controlled quantity.

Furthermore, once the triac is turned on, it stays on for the rest of that half cycle, and the system becomes unregulated for that time period. However, the controlled quantity in this case is temperature, which has a long time constant when compared to the switching frequency of the triac. As a result of the long thermal time constant, the system may still be approximated by a linear continuous model suitable for the regulation of target temperature.

3.5 Form of the transfer function of each block

3.5.1 Comparator

The behaviour of the comparator is governed by the transfer function of the electrometer, of the potentiometer attenuator and by the transfer function of the recorder including the bridge circuit.

In normal operation the attenuator potentiometer was adjusted to display 13 mV thermocouple emf, corresponding to the maximum temperature of about 1200°C , on 60% of full chart. Let the dc gain of the recorder combined with the attenuation of the potentiometer be A_r . Also let the normalized transfer function of the electrometer and the recorder be $G_e(s)$ and $G_r(s)$ respectively; therefore all elements can be represented in block diagram form as shown in Fig. 3.15. The frequency response of $G_e(s)$

and $G_r(s)$ will be determined in the next chapter.

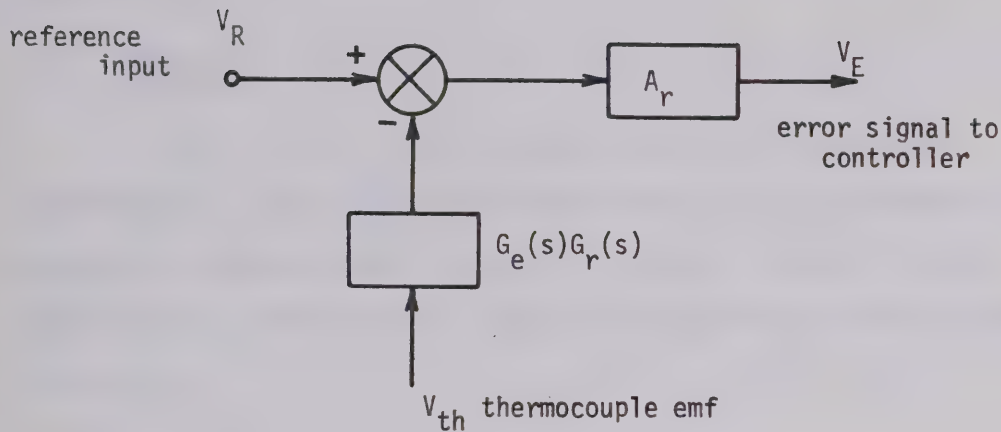


Fig. 3.15

Block diagram of the electrometer and recorder.

Full chart recording time corresponds to 5 minutes approximately. This is the time required for the synchronous motor to drive the reference potentiometer a full 10 turns. When the control system operates, the slider of the feedback potentiometer (right arm of the bridge) has to follow the slider of the reference potentiometer to maintain the bridge output voltage (error signal) near zero. If only 60% of full rotation is used the ramp speed will be increased to $\frac{13\text{mV}}{\frac{6}{10} \times 5\text{mm}} = \frac{13\text{mV}}{3\text{ min.}}$ which corresponds to $\frac{(1200-25)\text{ }^{\circ}\text{C}}{3\text{ min.}}$. When

a smaller percentage of full rotation of the recorder potentiometer is used, however, the attenuation of the attenuator potentiometer must be increased. This will result in the total gain A_r being decreased. Compensation must be provided for this by increasing V_b and/or amplifier gains K_1 , K_2 .

3.5.2 Controller

The transfer function of the controller was previously established as : $(K_2 + \frac{K_1}{T_i s})$. Amplifier gains K_1 and K_2 are constant in the normal frequency range of interest (less than 1 KHz). The block diagram of the control circuit including the amplifier offsets is drawn in Fig. 3.16

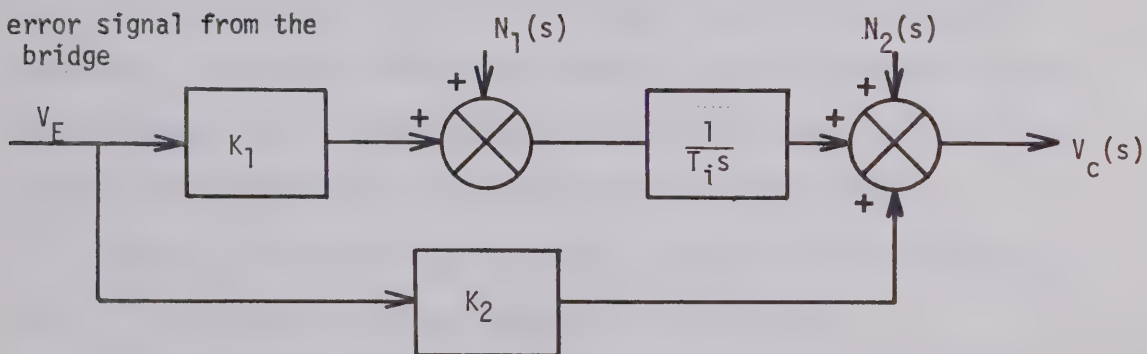


Fig. 3.16

Block diagram of the control circuit

where N_1 is the offset at the integrator input,

N_2 is the offset of the summer and amplifier K_2 .

Both N_1 and N_2 are approximated to be constant.

3.5.3 Trigger and triac circuits

The gain of the trigger and triac circuits may be expressed as

$$\frac{\text{output current (amperes)}}{\text{input control voltage}} = \frac{I_f}{V_c} = \frac{e^{-s\tau_b}}{Ts+1}$$

The time delay τ in the expression varies between 0 and 8 ms. The time constant T represents $\frac{L}{R}$ for the inductive portion of the filament transformer load.

To find the steady state gain of the circuits a variable dc voltage was applied to the circuit. The output filament current was then measured. It was found that the circuit had a small insensitive region at low input signal (V_c) but this could be minimized by adjusting the gain of the circuit which also set the initial output current.

The data plotted in Fig. 3.17 show a linear relation between V_c and I_f . The straight line has slope of 0.521 Amps/Volt.

The block diagram of both circuits can be shown as in Fig. 3.18.

3.6 Block Diagram Representation of the Control System

From the curves of V_{th} vs. I_f and I_f vs. V_c the nonlinearities in the normal operating region ($I_f = 2$ to 3.5 amperes) are quite small. The system therefore may be linearized so that linear analysis can be

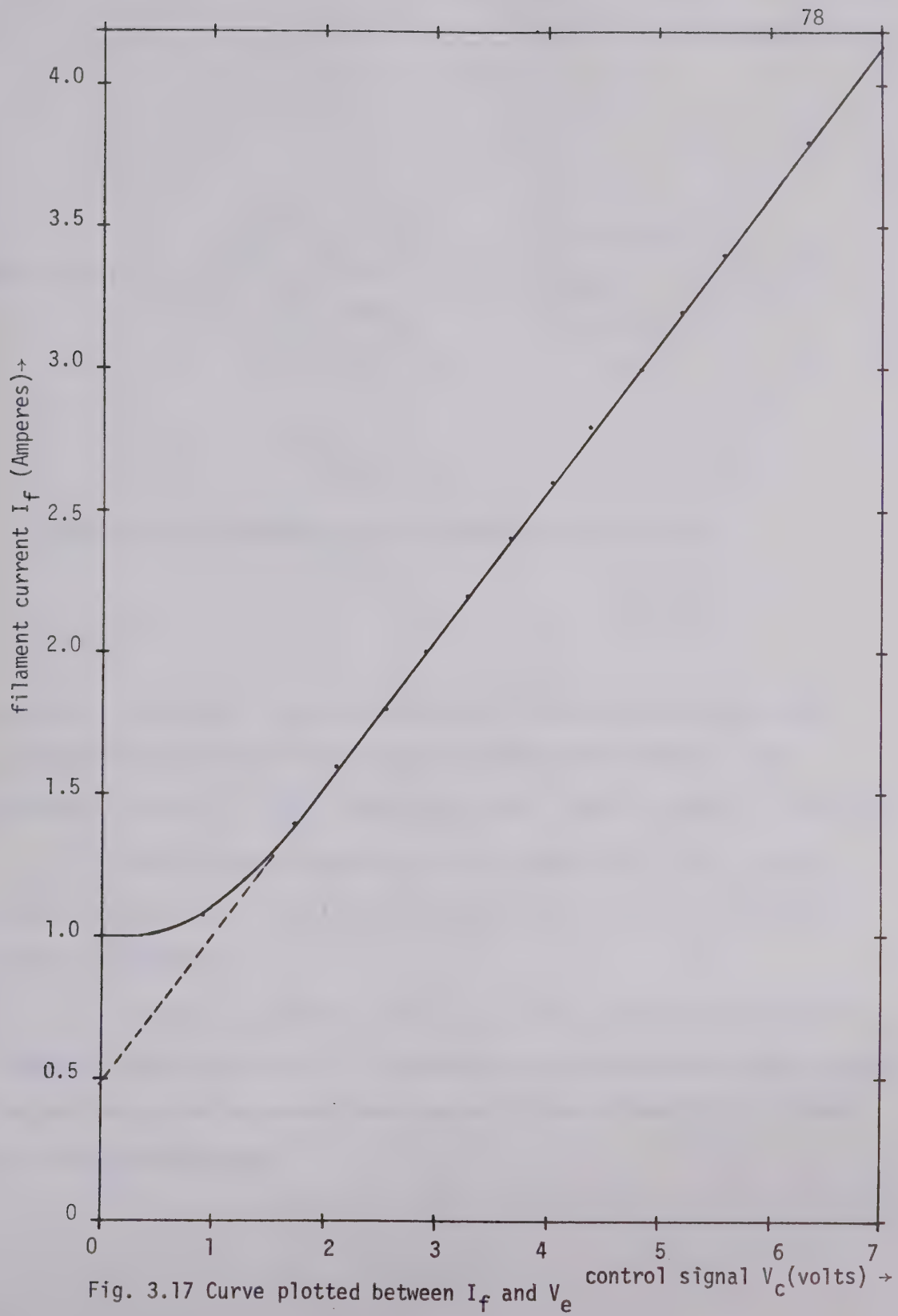


Fig. 3.17 Curve plotted between I_f and V_c

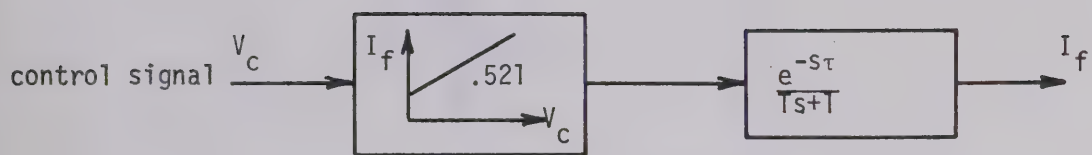


Fig. 3.18

Block diagram representing the trigger and triac circuits.

applied. The slopes of these curves about certain operating points can be regarded as constants that were calculated before (Chapter I and previous section 3.5). The linearized system is then as shown in Fig.3.19.

The variable parameters in this system are A_r , K_1 , T_i and K_2 which have to be set to meet the specifications as outlined in the last section of Chapter I.

In the next chapter, frequency response methods will be used to obtain all necessary details of the complete system characteristics. In particular, the system parameters are adjusted by use of Bode plots to obtain the desired performance.

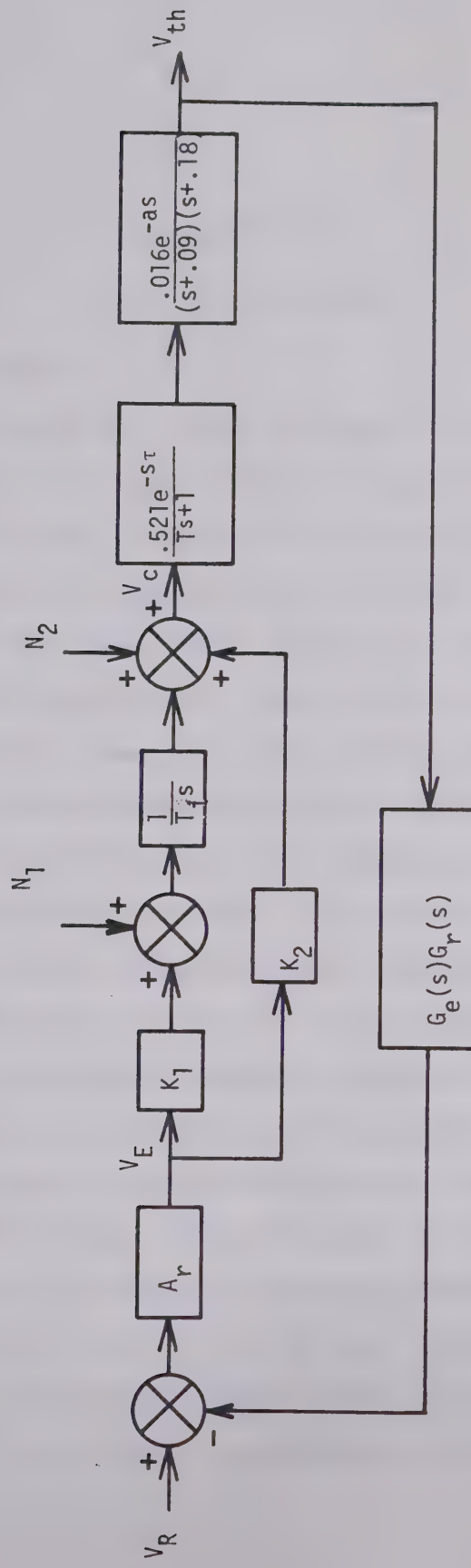


Fig. 3.19

Block diagram of the linearized system.

CHAPTER IV

ANALYSIS AND DESIGN

4.1 Introduction

This chapter will present procedures in the analysis, design and compensation of the system to meet the specifications. The approach used in this chapter is based on the frequency response method as represented by Bode diagrams.²¹ In this method, the steady state response of the open loop transfer function to a sinusoidal input is represented by two separate plots: one is a plot of the logarithm of the magnitude of the sinusoidal transfer function, the other is a plot of the phase angle; both are plotted against frequency on a logarithmic scale. The system behaviour is determined and the design is carried out via frequency domain techniques. The transient response behaviour was considered in terms of frequency domain specifications such as phase margin, gain margin, resonant peak value and bandwidth. The analysis and design in the frequency domain is therefore indirect because the system is designed to satisfy the frequency domain specifications rather than the desired time domain specifications. However, the frequency response plot indicates clearly the manner in which the open loop transfer function should be modified or adjusted to obtain the desired transient response characteristics. After the open loop transfer function has been designed by the frequency response method, the transient response characteristics have to be checked to see whether or not the designed system

satisfies the requirements in the time domain. If it does not, then the design transfer function must be modified and the analysis repeated until a satisfactory result is obtained.

The root locus method²¹ will also be used to show the contributions of each open loop pole or zero to the system behaviour. In this method, the locus of roots of the characteristic equation of the closed-loop system, as the gain is varied from zero to infinity, is plotted in the s plane. The position of the closed loop poles for a specific gain of the open loop transfer function may be approximated, and the characteristic of the transient response of the closed loop system may, therefore, be determined.

The next section will show the results of the frequency response test in which the frequency response of each component in the control loop was determined experimentally and finally combined. The resulting frequency response indicates the manner in which various parameters of the controller should be adjusted to obtain stability and meet the required specifications. This is done in section 4.3. Later, the system is compensated to maintain the stability at higher values of gain as illustrated in section 4.4. The final section(4.5) will discuss the effect of the inexact cancellation of one pole of the thermal plant.

4.2 Determination of the Frequency Response

The frequency responses of the following components were determined:

- Recorder including electrometer and attenuating potentiometer.

b) Trigger, triac circuits and the thermal system (filament, target and thermocouple).

4.2.1 Experimental procedure

A General Radio Type 1305-A low frequency signal generator was used to obtain the frequency response of two sets of system components. The generator frequency was variable from 0.01 Hz to 1000 Hz. Two outputs were available from the generator. The phase of one output with respect to another fixed reference output was variable. The phase shift adjustment on the generator was calibrated in degrees. To obtain the frequency response of a system component, the generator, the oscilloscope and the component under test were connected as shown in Fig. 4.1.

In finding the frequency response for both component sets a) and b) the sinusoidal signal was superimposed on a dc bias signal at suitable level and then applied to the system components as mentioned. The gain and phase shift through the system components were measured by means of the oscilloscope as the input frequency was varied.

4.2.2 Results

The Bode diagram of the recorder and electrometer with V_b set at 6 volts is plotted as shown in Fig. 4.2. The attenuation from the potentiometer setting (≈ 16.08 db) is to be subtracted from the recorder gain. The frequency response of the electrometer at a gain of 1 is flat (within 3 db) throughout the frequency range from dc to 50 KHz. Therefore the frequency response obtained effectively is that of the

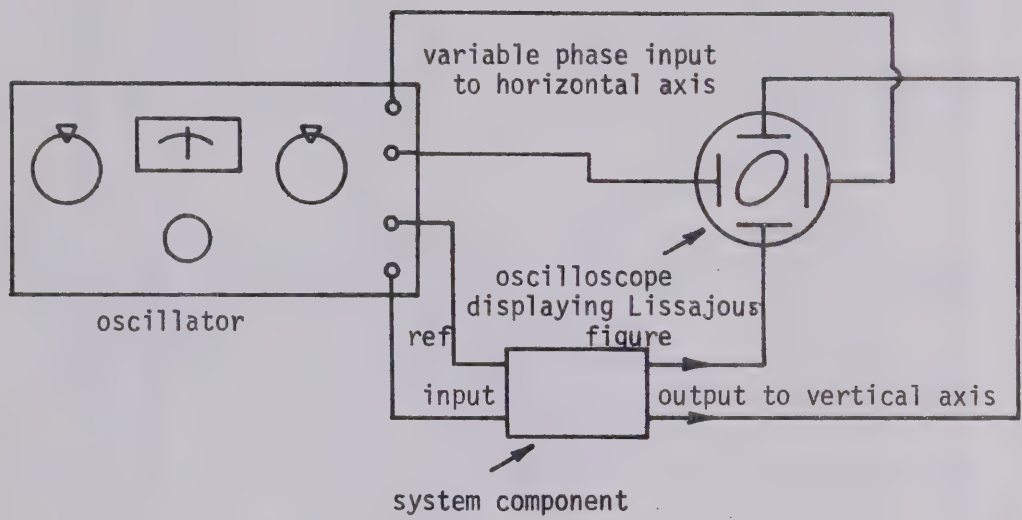


Fig. 4.1

Instrument set up for frequency response test

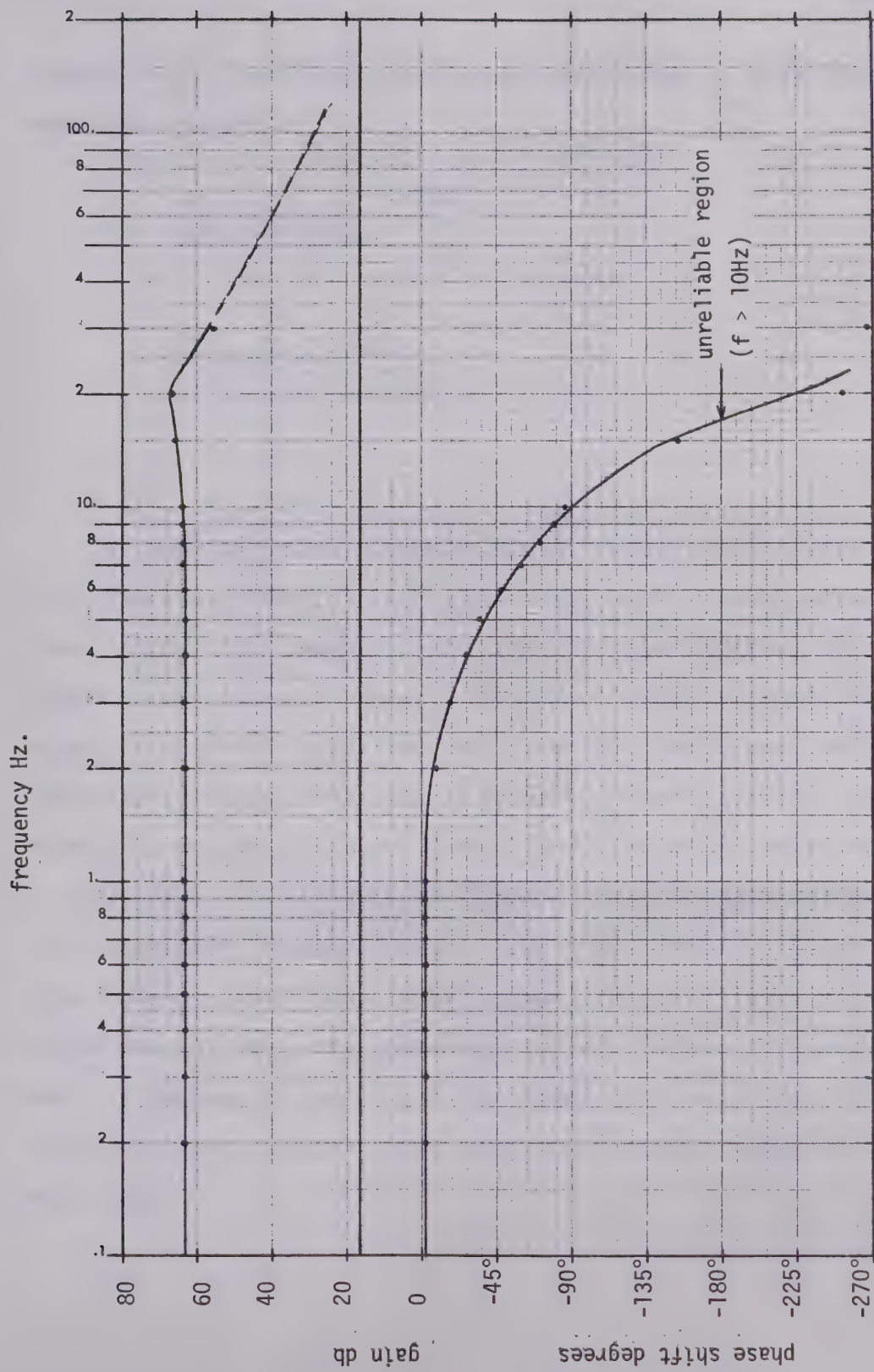


Fig. 4.2 Bode diagram of the recorder and electrometer.

recorder only. From these plots the transfer function of these three components combined is

$$\begin{aligned}
 G_r &\approx \frac{227 \times (40\pi)^2 \times 140\pi \times e^{-0.005s}}{(s+40\pi)^2(s+140\pi)} \\
 &= \frac{15.79 \times 10^8 \times e^{-0.005s}}{(s+125.66)^2(s+439.82)}
 \end{aligned} \tag{4.1}$$

Parts of the response curves at higher frequencies which could not be found experimentally were interpolated and are shown as dotted lines. Another Bode diagram for the trigger-triac circuits and the thermal system combined is shown in Fig. 4.3. It was found that the trigger-triac circuits contribute nothing to the shape of phase response curve within the measurable range of frequency response (< 5 Hz). Both response curves generally agree with the linearized second order transfer function as derived in Chapter II, but without time delay effects, in the measurable frequency response. The dc gain and the -positions of poles, however, are different because a new target and filament had to be used for this test. Any change made in these elements will usually result in the transfer function of the thermal system also being changed. From the frequency response curves the normalized transfer function is found to be

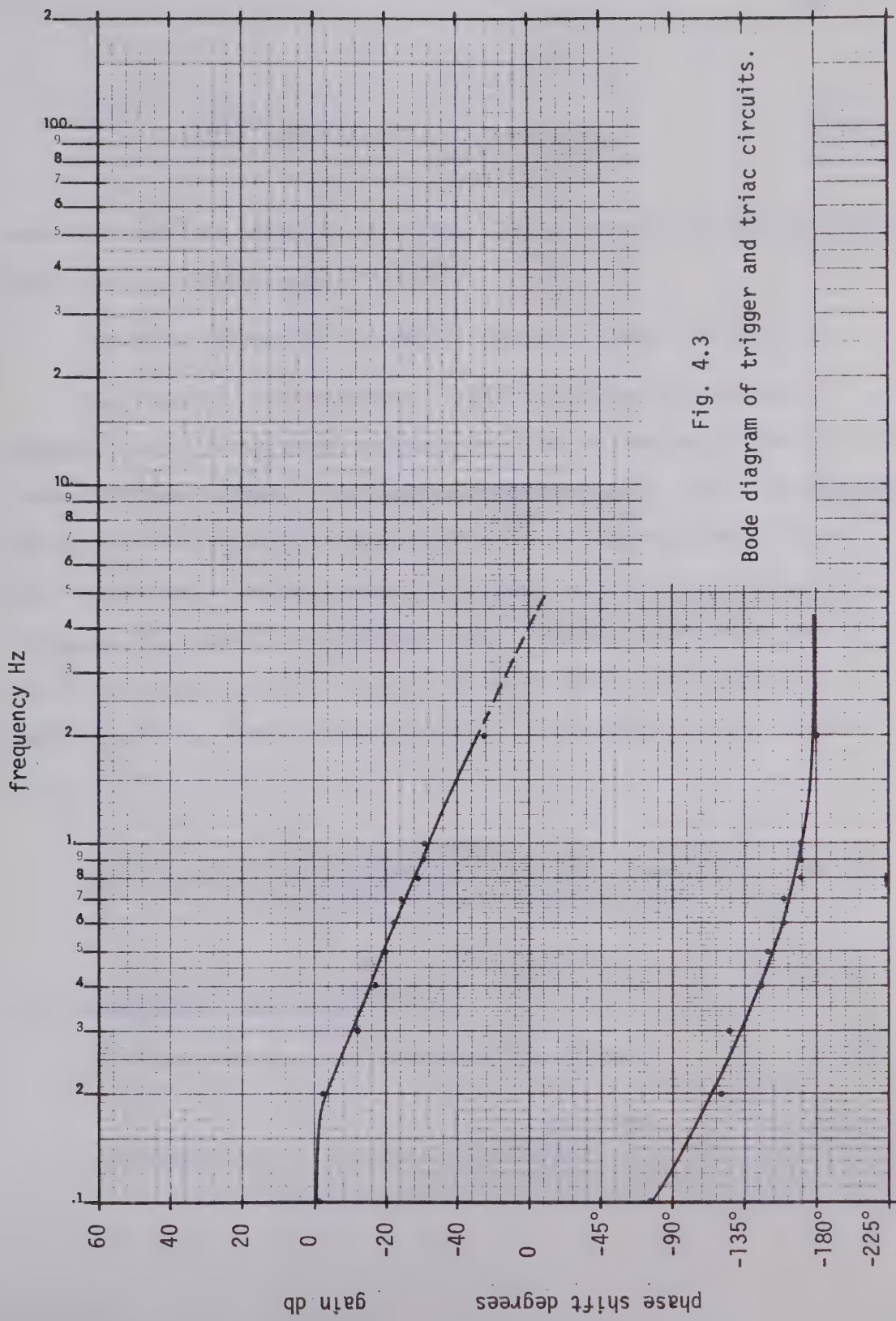


Fig. 4.3
Bode diagram of trigger and triac circuits.

$$\frac{G_p}{K} = \frac{.2825}{(s+.25)(s+1.13)} \quad (4.2)$$

where the suffix p refers to the plant. The dc gain during the experiment was found to be approximately 4×10^{-3} .

The block diagram of the complete system is shown in Fig. 4.4.

The frequency response curves from Fig. 4.2 and 4.3 are added together, yielding the total response of elements from the trigger circuit forward to the recorder. The results are shown in Fig. 4.5. The response curves have the essential characteristics of the thermal system itself. The instability is mainly caused by the presence of the recorder which increases the order of the system by two. However, the forward gain can be increased up to 53 db (=gain at 446.7) before the system will become unstable. The transfer function of the combined curves is found to be

$$G_r(s) G_p(s) = \frac{17.83 \times 10^5 \times e^{-0.005s}}{(s+.25)(s+1.13)(s+125.66)^2(s+439.82)} \quad (4.3)$$

4.3 Adjustment of Controller Gains

The open loop transfer function of the system is

$$G_r(s) G_p(s) G_c(s) = G(s)H(s) = \frac{17.83 \times 10^5 \times e^{-0.005s} \times K_2 \{s + K_1 / (K_2 T_i)\}}{s(s+.25)(s+1.13)(s+125.66)^2(s+439.82)}$$

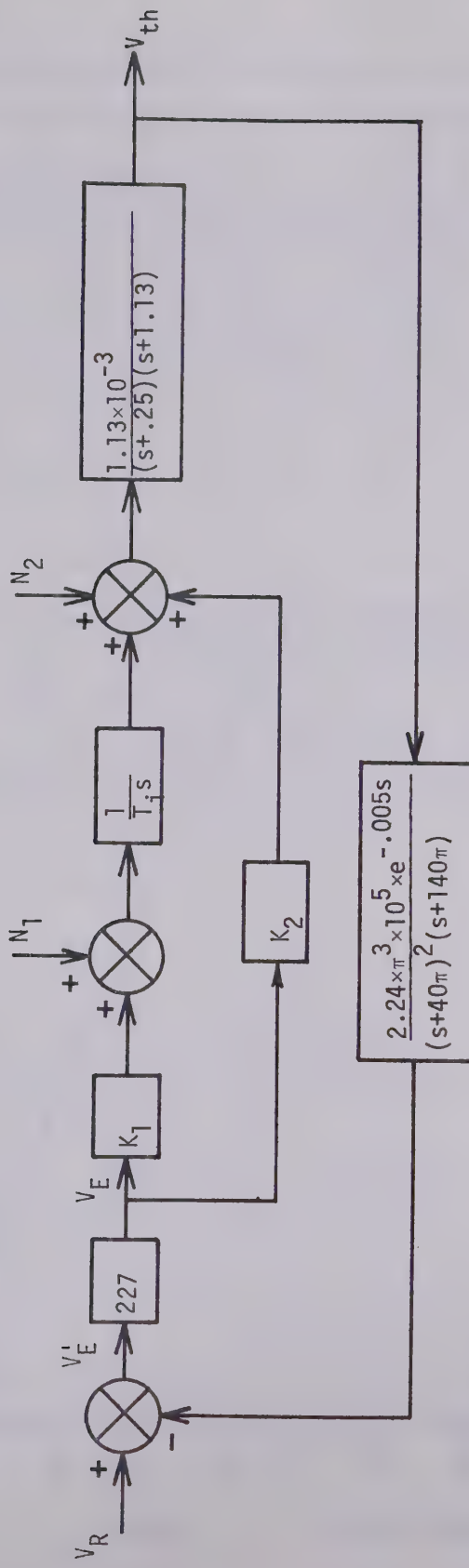
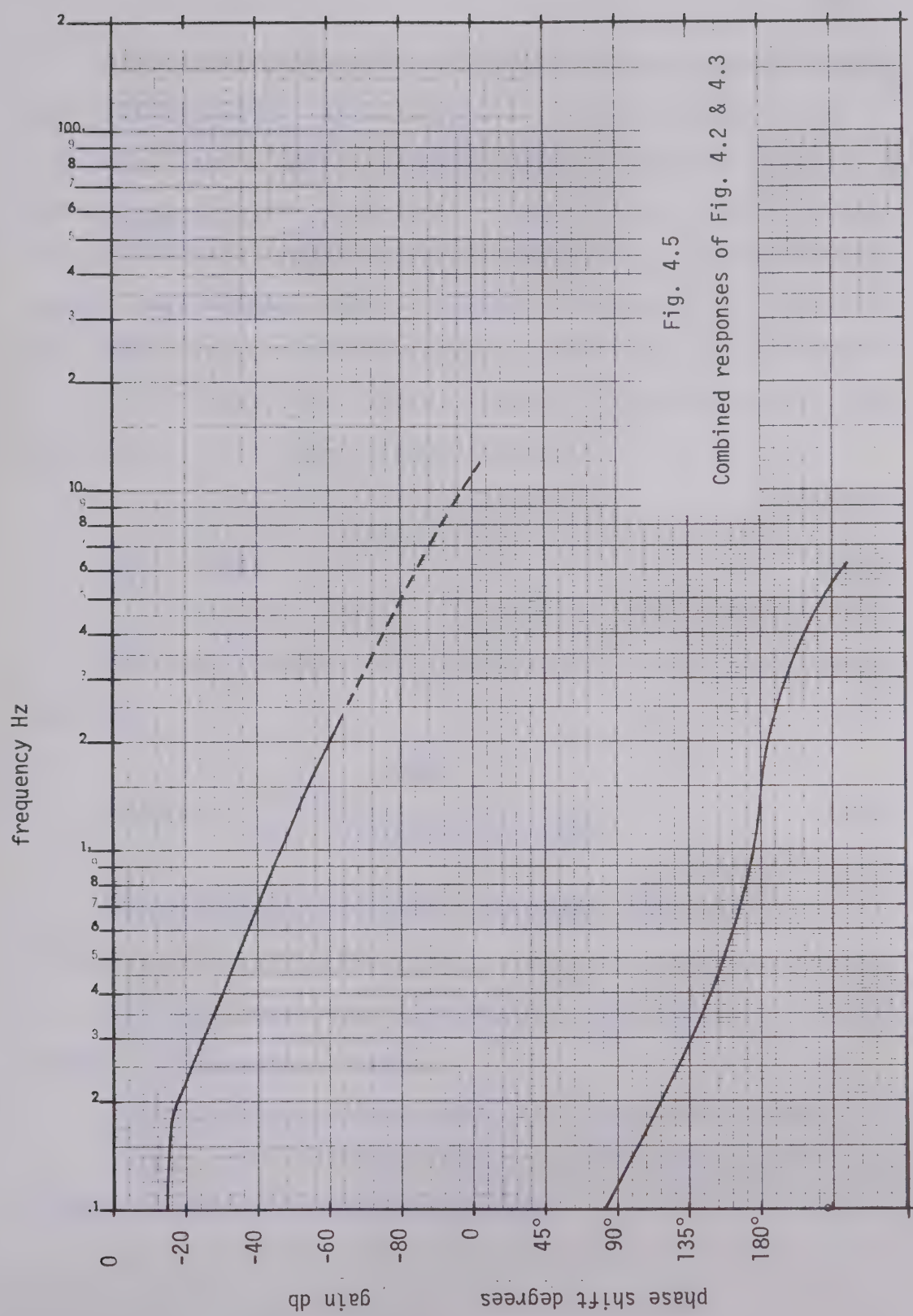


Fig. 4.4
Block diagram with calculated transfer functions.



The presence of the pole at the origin from the integrator creates the stability problem. By looking at the frequency response in Fig. 4.5, only a value of gain K_2 as small as 10 will result in negative phase and gain margins if the zero in $G(s)H(s)$ is not properly located. This will bring the system to instability even at very low forward gain and the system becomes useless. Therefore the zero at $s = -\frac{K_1}{K_2 T_i}$ must be carefully placed such that it cancels a pole either at $s = 0$ or at $s = -.25$. In order to maintain the integrating effect of the controller, the pole at $s = -.25$ should be cancelled; thus

$$\frac{K_1}{K_2 T_i} = .25. \quad (4.4)$$

The compensated open loop transfer function after cancellation is therefore

$$G(s)H(s) = \frac{17.83 \times 10^5 \times e^{-0.005s} \times K_2}{s(s+1.13)(s+125.66)^2(s+439.82)}. \quad (4.5)$$

The Bode diagram of the open loop transfer function for $K_2 = 1$ is plotted as solid lines in Fig. 4.6.

The steady state errors due to the reference input and the amplifier offsets are considered as follows.

a) Steady state positional error to the ramp function input

If this error is to be kept less than .05 volt per volt/sec (i.e., 5 %/sec) of the final output velocity, then

$$K_v = \frac{\text{output velocity}}{\text{steady state error}} = \frac{V_o}{e_{ss}} \quad (4.6)$$

$$= \frac{1}{.05} = 20 \text{ sec}^{-1}$$

and also

$$K_v = \lim_{s \rightarrow 0} s \cdot G(s)H(s) \quad (4.7)$$

$$= \lim_{s \rightarrow 0} \frac{s \cdot 17.83 \times 10^5 \times e^{-0.005} \times K_2}{s(s+1.13)(s+125.66)^2(s+439.82)} \quad (4.8)$$

$$= .227 K_2.$$

This implies that $.227 K_2 \geq 20$ or $K_2 \geq 88.1$.

Therefore $\frac{K_1}{T_i} \geq .25 \times 28.1$ or ≥ 22.03 depending on K_2 .

b) Steady state errors due to amplifier offsets

From the block diagram in Fig. 4.4, the closed-loop transfer function $\frac{V_{th}}{N_1}$ in the absence of V_R , N_2 is

$$\frac{V_{th}(s)}{N_1(s)} = \frac{1.13 \times 10^{-3}}{T_i s(s+.25)(s+1.13) + \frac{17.83 \times 10^5 \times e^{-0.005s}}{(s+125.66)^2(s+439.82)} (K_1 + K_2 T_i s)} \quad (4.9)$$

Hence the steady state error due to a step offset of magnitude N_1

is

$$e_{ss}(N_1) = \lim_{s \rightarrow 0} s \cdot \frac{-1.13 \times 10^{-3}}{T_i s(s+.25)(s+1.13) + \frac{17.83 \times 10^5 \times e^{-0.005s}}{(s+125.66)^2(s+439.82)} \cdot \frac{N_1}{(K_1 + K_2 T_i s)}} \cdot \frac{N_1}{s}$$

$$= -\frac{N_1}{227K_1} \quad (4.10)$$

The steady state output due to offset N_1 is then

$$c_{ss} = -e_{ss}(N_1) = \frac{N_1}{227K_1} \cdot \frac{N_1}{s} \quad (4.11)$$

The magnitude of N_1 is usually less than .2 volt and from this equation N_1 is usually minimized by a large gain from the recorder ($= 227$).

In the same manner, the steady state error due to a step offset N_2 can be found as

$$e_{ss}(N_2) = \lim_{s \rightarrow 0} s \cdot \frac{1.13 \times 10^{-3} T_i s}{T_i s(s+.25)(s+1.13) + 17.83 \times 10^5 e^{-0.005s} (K_1 + K_2 T_i s)} \cdot \frac{N_2}{s}$$

$$= 0 \quad (4.12)$$

Thus the steady state error due to offsets of the amplifier having gain K_2 and of the summing amplifier which do not pass through the integrator will be zero. In the transient state where these offsets have

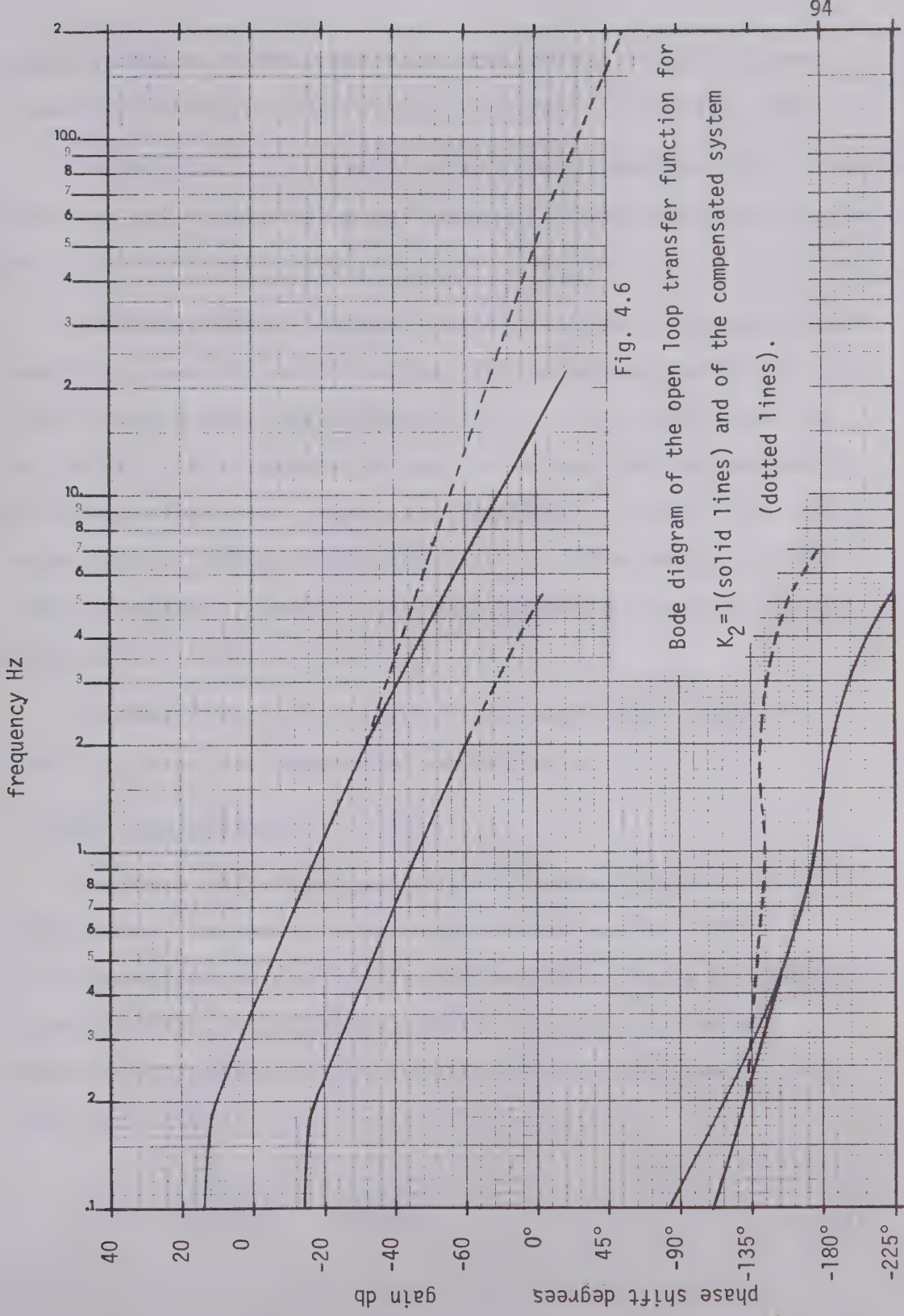


Fig. 4.6

Bode diagram of the open loop transfer function for
 $K_2=1$ (solid lines) and of the compensated system
(dotted lines).

some contribution to the error signal, they are still negligible when compared with the error signal due to the reference input (V_R) itself.

The amplifier drift is not a serious problem because of its equivalent rate of rise being small compared to the speed of the ramp input.

For a satisfactory transient response performance, the phase margin should be between 30° and 60° and the gain margin should be greater than 6 db.²¹ From the Bode diagram plotted in Fig. 4.6 the value of gain K_2 at 2 db will give a phase margin equal to 30° but from the requirements for steady state error, K_2 must be at least 88.1 or 38.9 db. At this value of gain K_2 the phase and gain margin are approximately -14° and -14 db respectively. These indicate that the system is unstable at this gain setting.

In order to meet all the system requirements and to maintain stability, phase lead compensation was introduced.

4.4 Phase lead compensation network

The phase lead network was designed²¹ based on the value of K_2 of 100 or 40 db. The desired phase and gain margin are 30° - 60° and ≥ 6 db respectively. The transfer function of the network as represented by the Bode plots was adjusted to compromise between the desired specifications and gain loss by the attenuation of the network. The design yields the transfer function of the network as

$$G_C(s) = \frac{s + (2\pi \times 2)}{s + (2\pi \times 50)} = \frac{s + 12.57}{s + 314.16} \quad (4.13)$$

The attenuation is $\frac{2}{50}$ or .04.

The network was inserted into the feedback path between the electrometer and the attenuating potentiometer as shown in Fig. 4.7.

The gain of the electrometer was set at 100 at which the frequency response was 0 - 1 KHz. The bandwidth was still wide such that its gain remained constant for the whole operating frequency range (<10 Hz).

The transfer function of the network is

$$\frac{V_o(s)}{V_e(s)} = \frac{R'_2}{R_1 + R'_2} \cdot \frac{\frac{R_1 C s + 1}{R_1 R'_2 . C s + 1}}{\frac{R_1 + R'_2}{R_1} 2} \quad (4.14)$$

$$= \frac{s + \frac{1}{R_1 C}}{s + \frac{1}{\alpha R_1 C}} \quad (4.15)$$

where $R'_2 = R_2 //$ (input resistance of the recorder and resistance of the attenuating potentiometer),

$$\alpha = \frac{R'_2}{R_1 + R'_2} \cdot \quad (4.16)$$

C was initially chosen as standard value of $1 \mu\text{f}$,

$$\text{therefore } R_1 = \frac{1}{10^{-6} \times 4\pi} = 79.5\text{K}$$

and $R'_2 = 3.32\text{K}$.

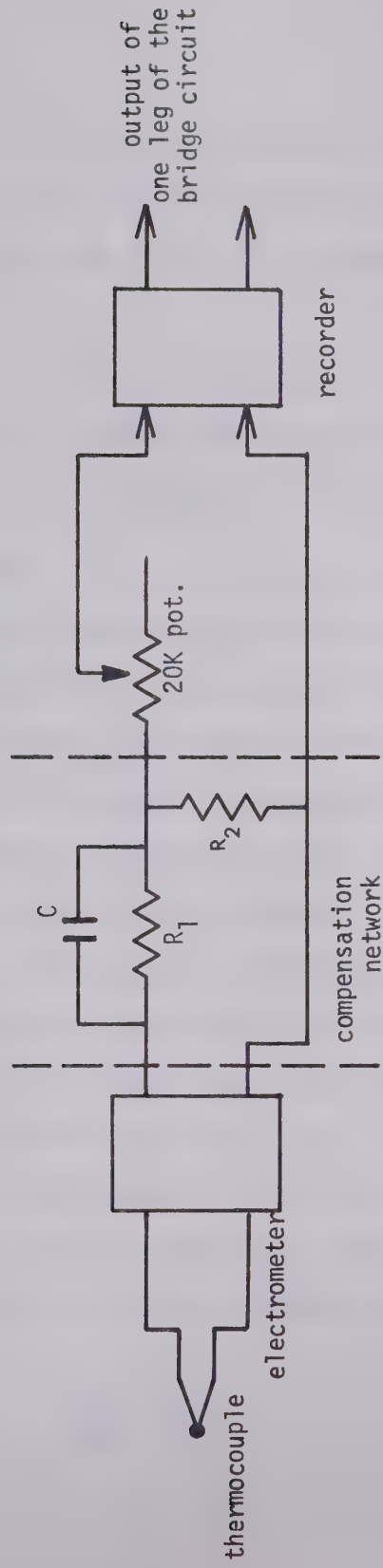


Fig. 4.7
Insertion of compensation network.

The input resistance of the recorder is approximately 340Ω . R_2 was chosen as $1M\Omega$. This will allow the adjustment of the attenuating potentiometer to be made to obtain the required input signal to the recorder.

The Bode diagram of the compensated system is plotted in dotted lines in Fig. 4.6. From the response curves the gain cross over frequency is at $f = 3.4$ Hz, the phase margin is $+34^\circ$ and the gain margin is +12 db.

4.5 Pole Shifting

Higher target temperatures will have the effect of reducing the time constant τ_h of the heating process as expressed by equation (2.21). The pole of the thermal plant nearer to the origin will move away from the origin, which will result in the cancellation of this pole by the zero from the controller becoming inexact. The root locus in this case may be shown as in Fig. 4.8 but without the compensation network. Increasing gain K_2 of the controller will move the zero at $- \frac{K_1}{K_2 T_i}$ towards the origin. The pole at the origin due to the integrator will be more effectively cancelled by this zero. The controller will then behave as a proportional controller having gain K_2 with only a small integrating effect. From the Bode diagram in Fig. 4.5, without the integrator, the forward gain can be increased up to 400 before the system becomes unstable. Therefore K_2 can be increased up to

$$\frac{400}{227 \times 4 \times 10^{-3}} = \frac{400}{.908} = 440$$

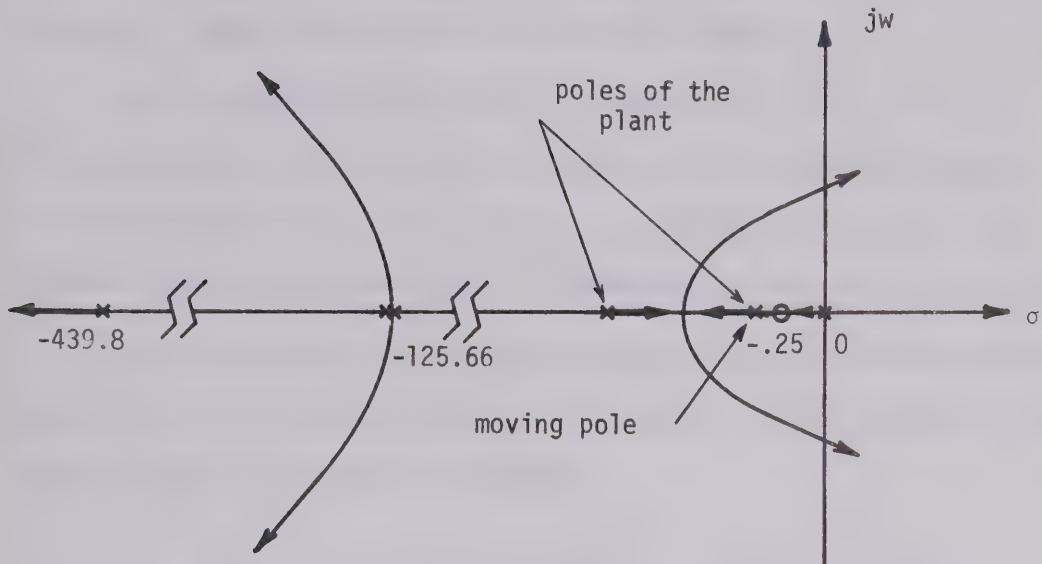


Fig. 4.8

Root locus of the system.

before instability sets in. Thus the controller has another operating condition as follows:

$$0 < K_2 < 440 ,$$

$$\frac{K_1}{K_2 T_i} \rightarrow 0, \neq 0, \quad (4.17)$$

i.e., the controller being mainly proportional and only slightly integral.

If the above condition is satisfied and gain K_2 is sufficiently high then the output will follow a ramp input with a small deviation

(depending on K_2) from linearity in the time interval and temperature range of interest. The long time constant of the thermal plant also helps to reduce this deviation to a smaller amount.

With the designed compensation network, the gain K_2 can be increased further to a very high value before the instability starts. From the interpolation curve in Fig. 4.5, the marginal value of the forward gain is 90 db or 3.163×10^4 corresponding to K_2 of about 3.48×10^4 .

The next chapter will illustrate typical step and ramp responses obtained from the actual system. These results will be compared to the specifications as set for the system.

CHAPTER V

RESULTS OF TEMPERATURE CONTROL

5.1 Introduction

This chapter will show the results of experiments carried out on the designed system, and will compare these against the specifications set for the system. Some other relevant characteristics of the control system will also be discussed.

5.2 Step Response

The output temperature change as a function of time in response to a step of input voltage was obtained by setting the reference potentiometer at a predetermined position corresponding to a required output temperature. The power to the control system was then turned on and the step response of the compensated system was recorded as shown in Fig. 5.1.

The transient performance of the controller may now be investigated. The temperature rises from room temperature ($\approx 25^\circ\text{C}$) up to the final temperature of approximately 1000°C with the following specifications

- a) Delay time, t_d : In this case the delay time is the time required for the response to reach half the final value. By measurement, $t_d \approx 1.7$ sec.
- b) Rise time, t_r : The time required for the response to rise from 10 to

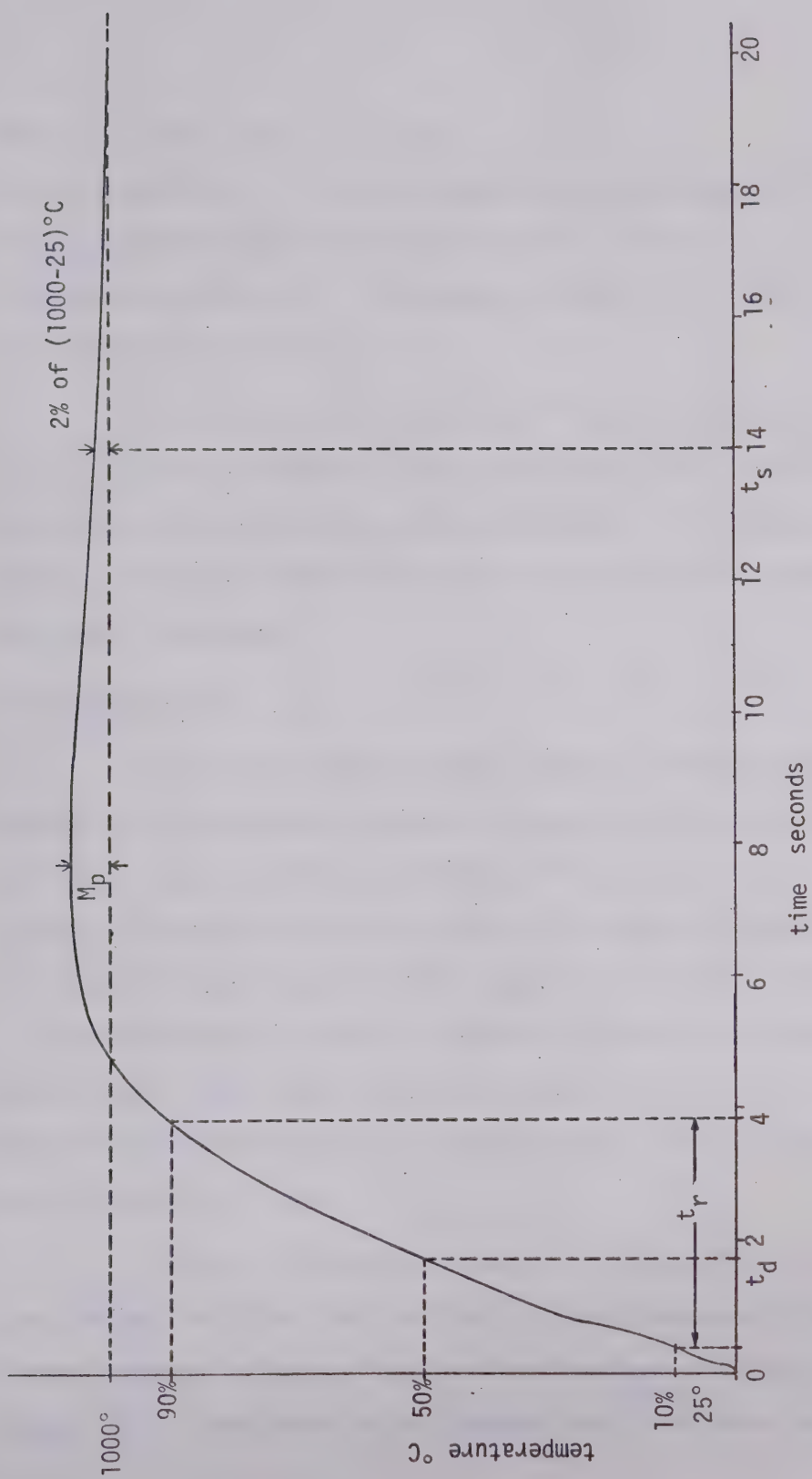


Fig. 5.1
Step response of the compensated system.

90% of its final value is ≈ 3.4 sec.

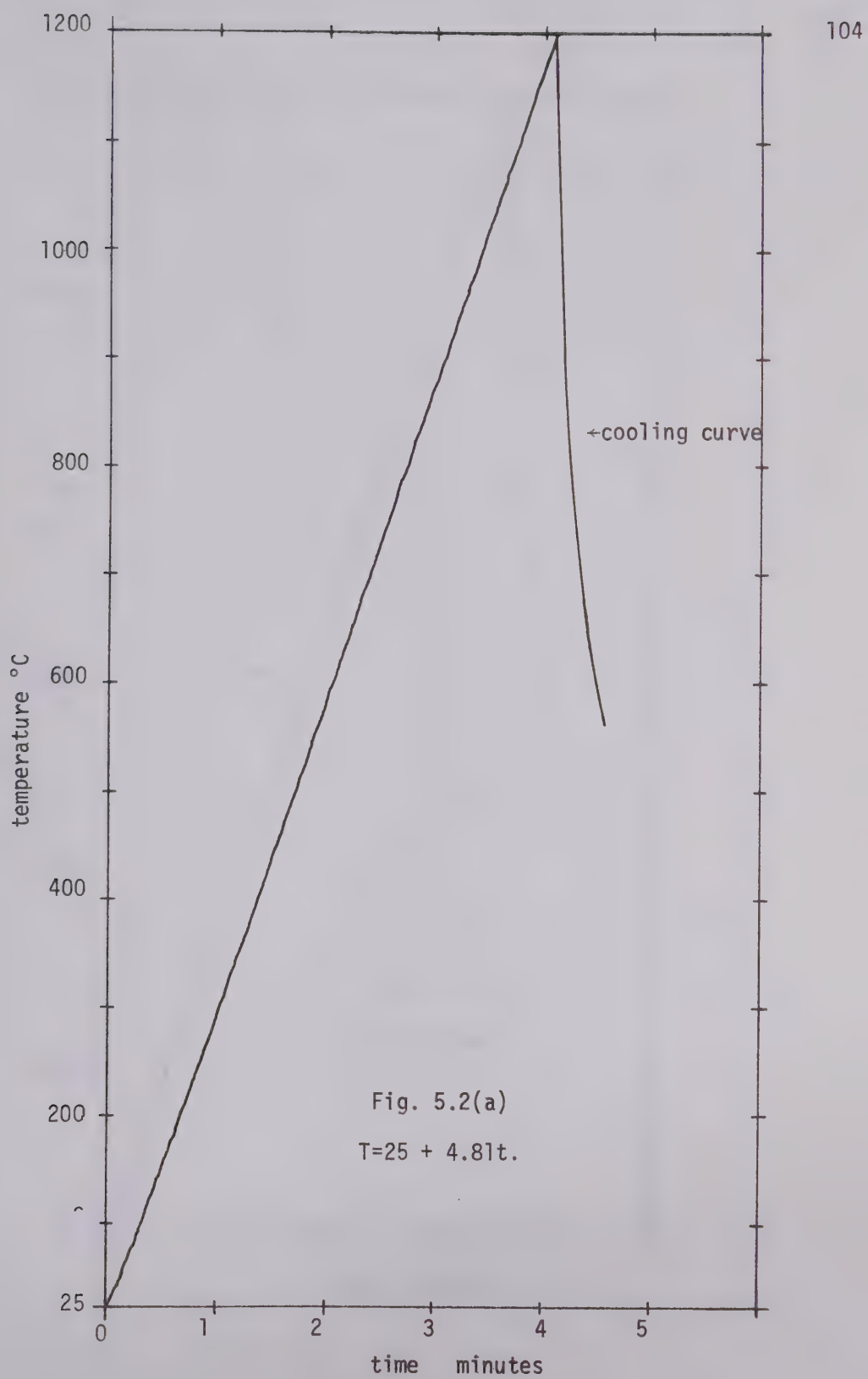
- c) Settling time, t_s : The time required for the response to decrease to and stay within 2% of its final value is ≈ 14 sec.
- d) Maximum overshoot, M_p : The maximum overshoot is $\approx 5.4\%$ corresponding to a damping ratio of $\xi \approx 0.7$.

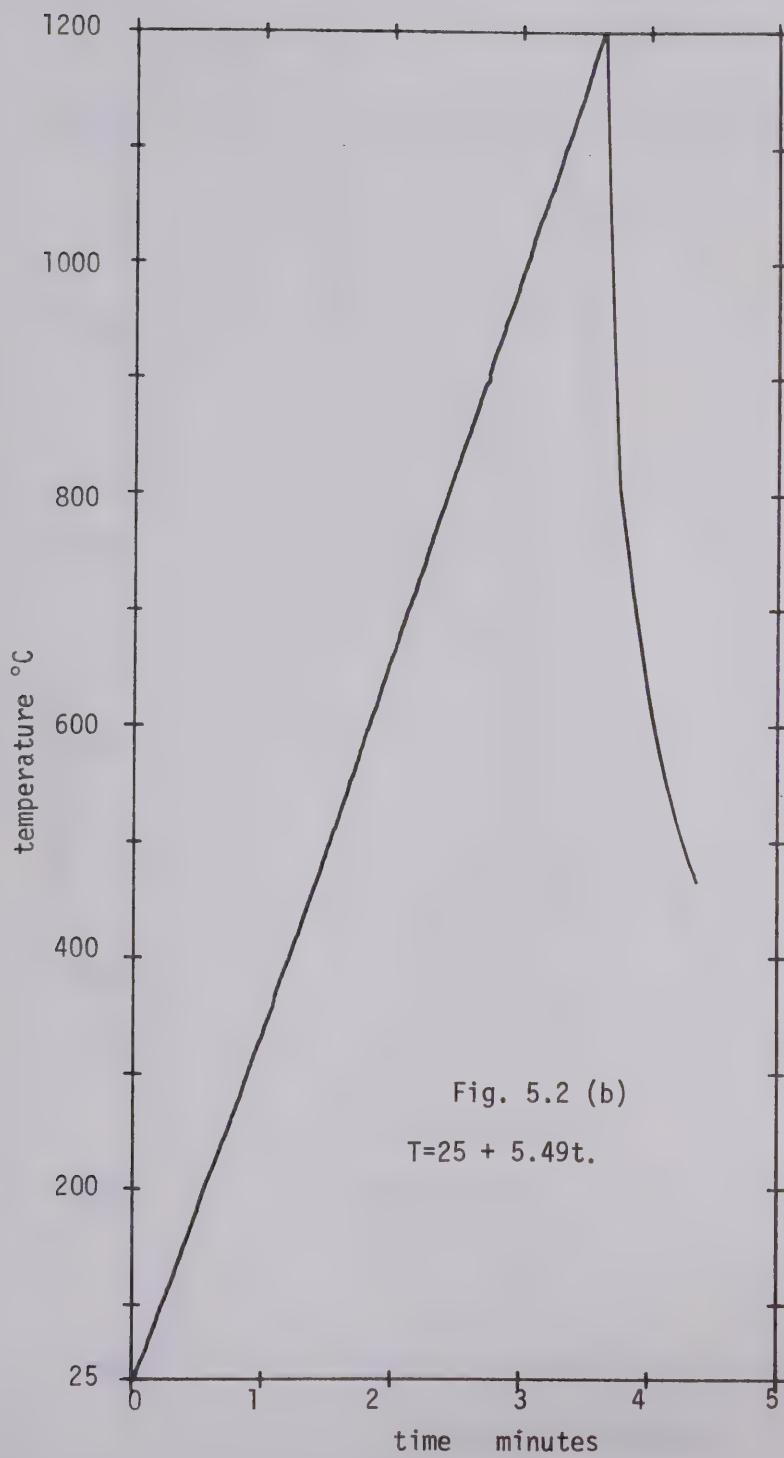
According to the required specifications, $t_r \leq 5$ sec and $M_p \leq 5\%$. These requirements conflict with each other. The maximum overshoot and the rise time cannot be made smaller simultaneously. However, the results obtained are quite acceptable and represent a reasonable compromise.

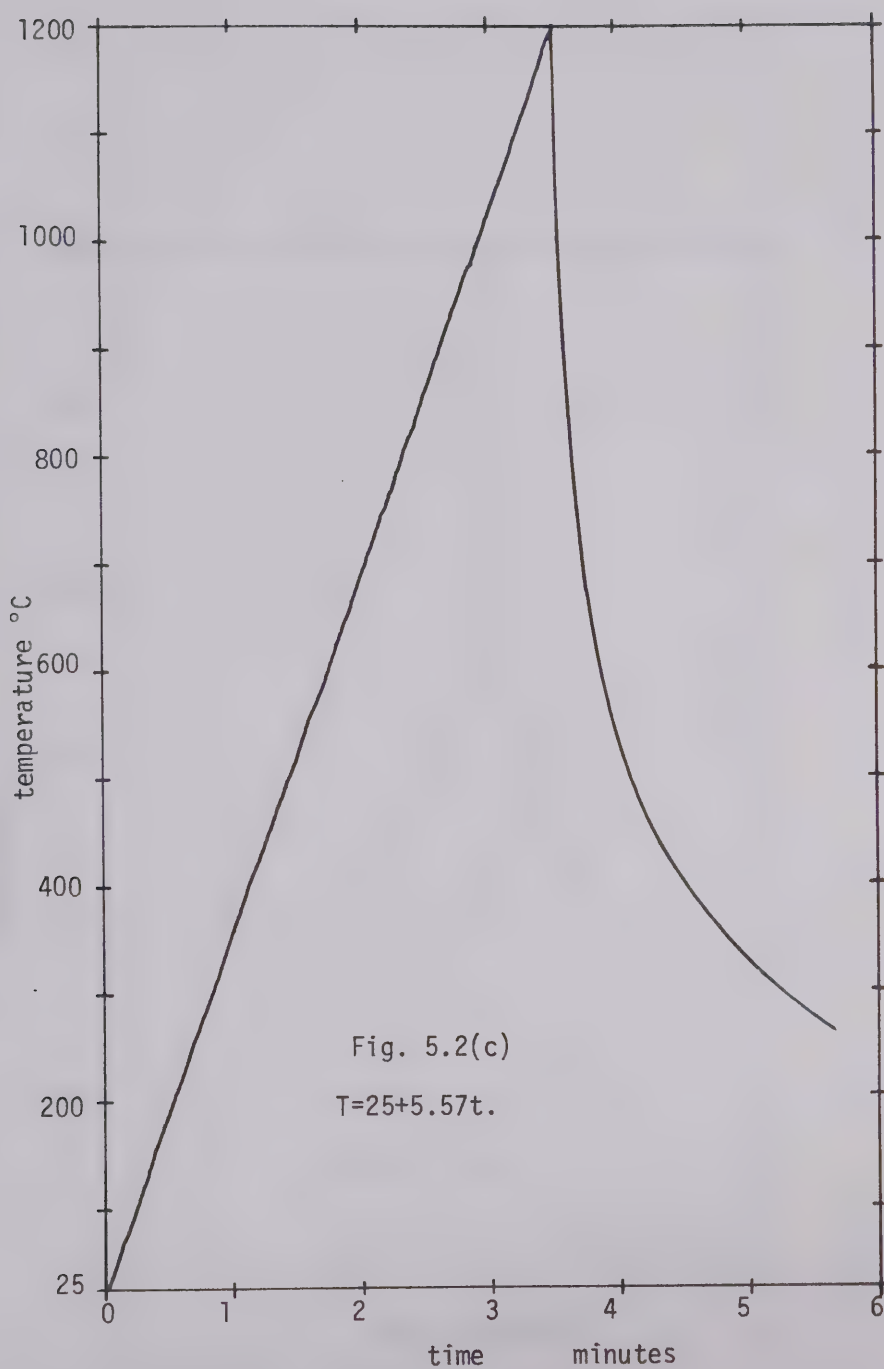
5.3 Ramp Response

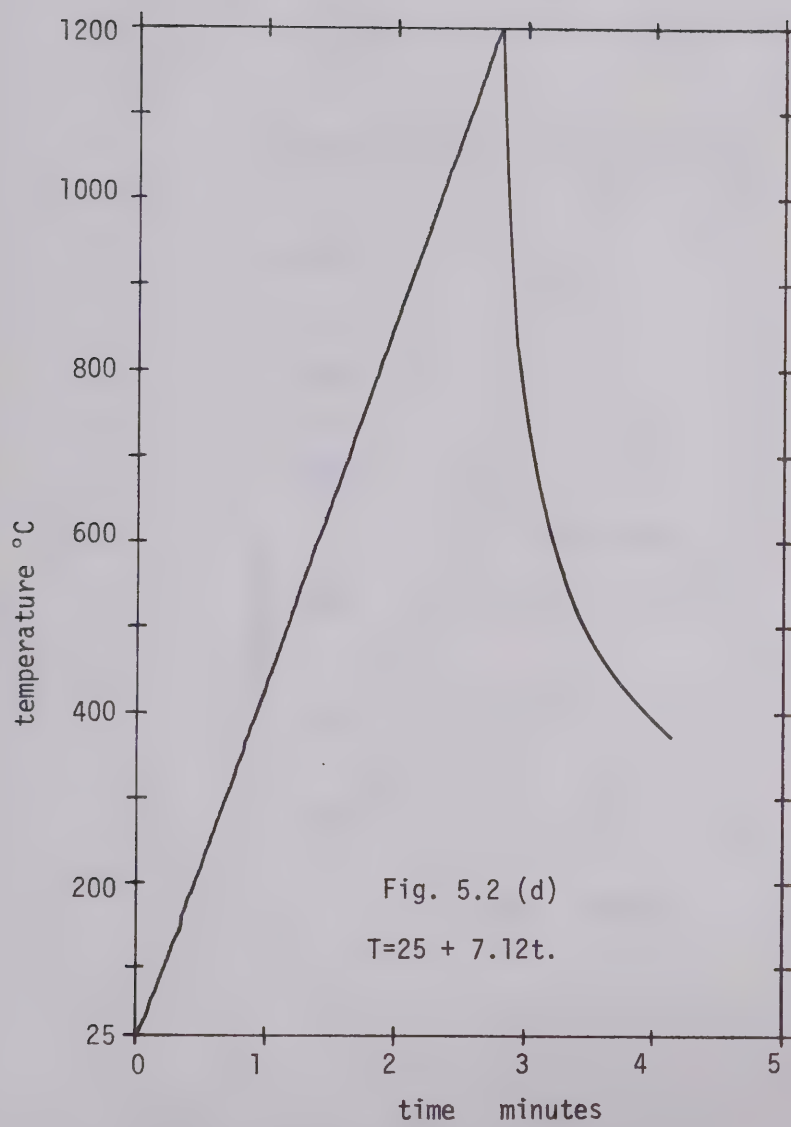
The linear temperature time curves or the ramp function responses of the compensated system are shown in this section together with their time functions in the form of $T = a + bt$. Fig. 5.2 a) to g) show the ramp responses of the system as designed previously. Fig. 5.3 shows the ramp responses of the system with parameters K_1 , K_2 and T_i adjusted for the second set of operating condition as described in section 4.5. These conditions were $K_2 = 400$, $K_1 = 150$, $T_i = 70$ for which the controller behaves as a proportional controller with only a small integrating effect.

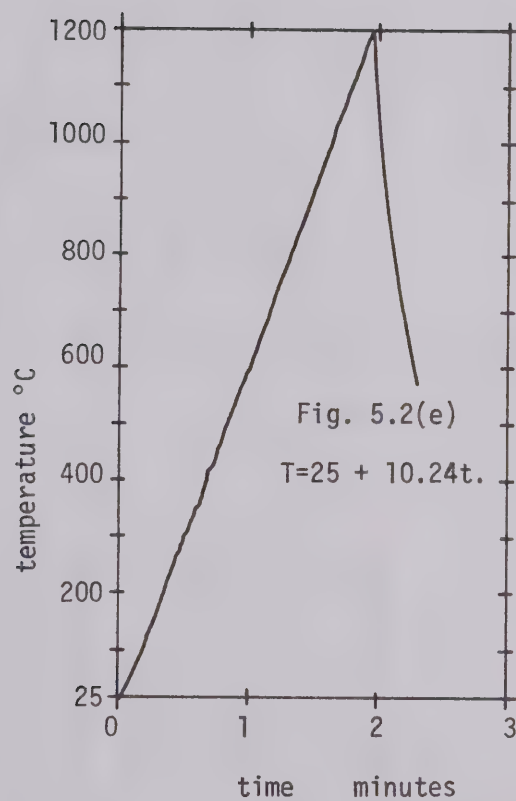
In Fig. 5.2 the steady state error signal (V_E) is fairly constant and less than 2 mV, implying that the thermocouple emf output differs from the reference input by less than $\frac{2}{227}$ mV in the steady state. This corresponds to the constant positional error in temp-

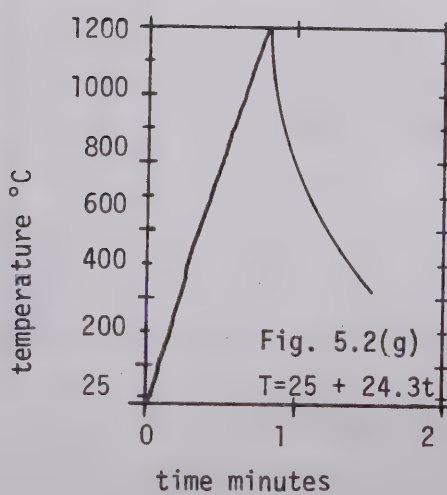
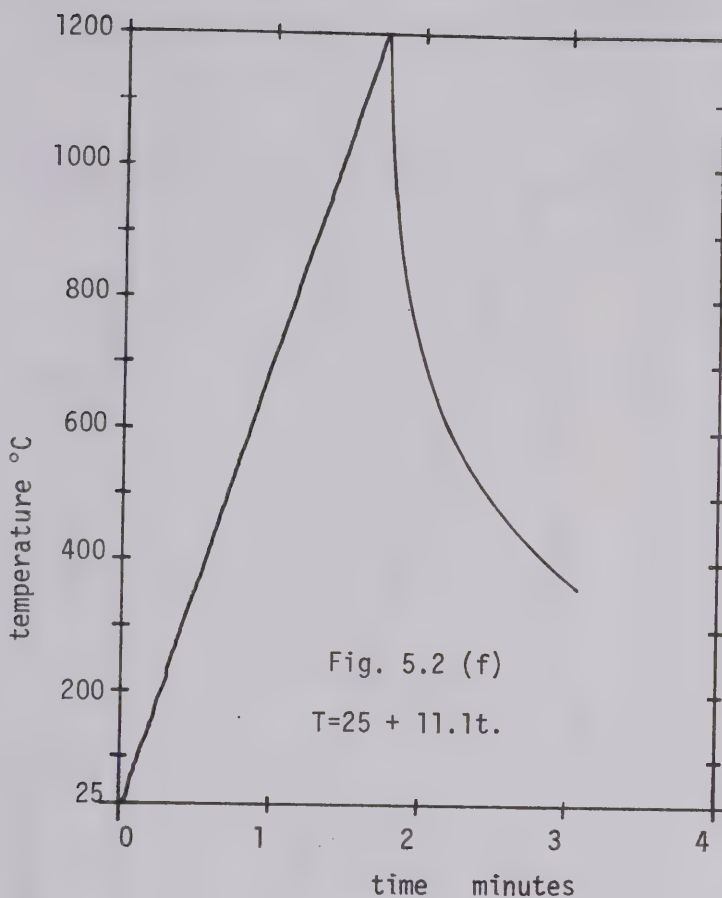


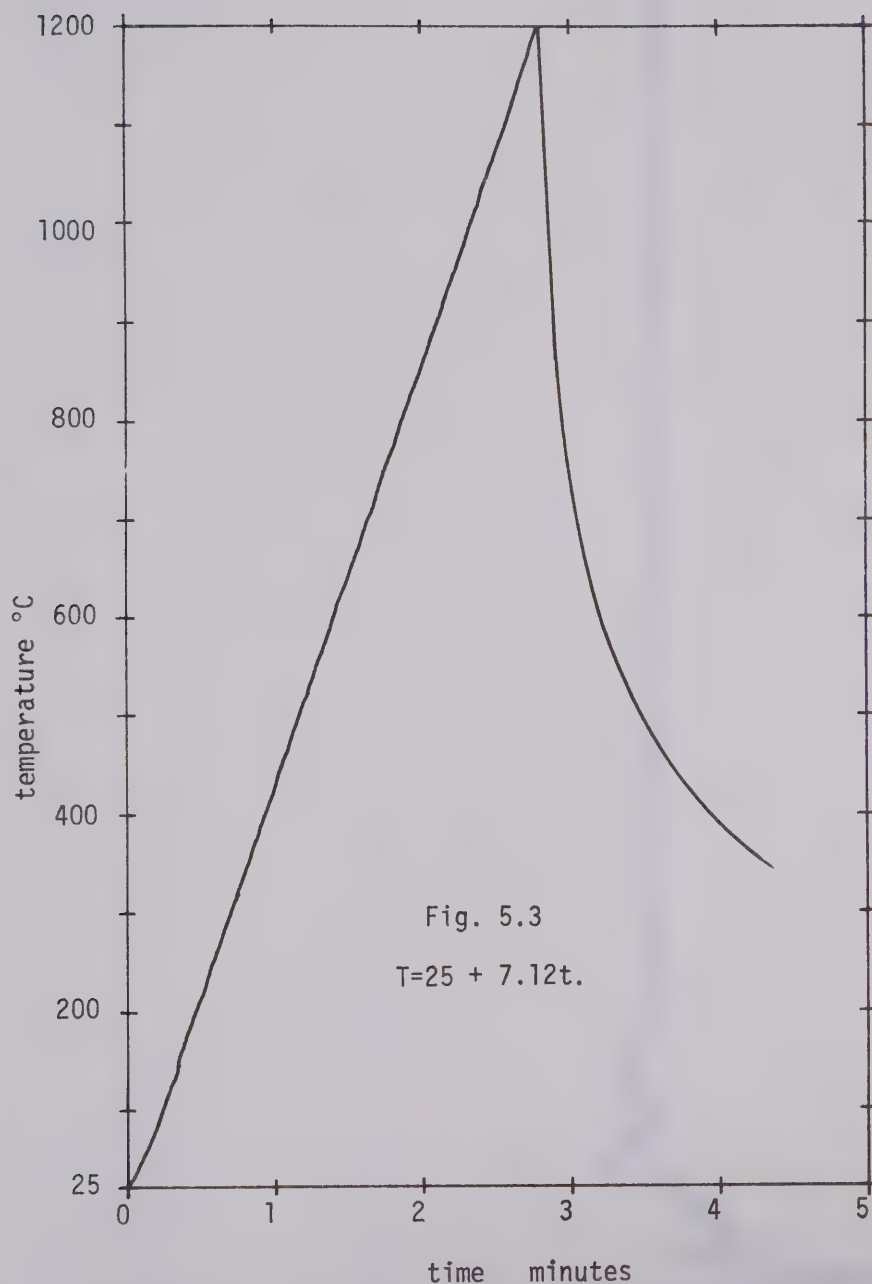












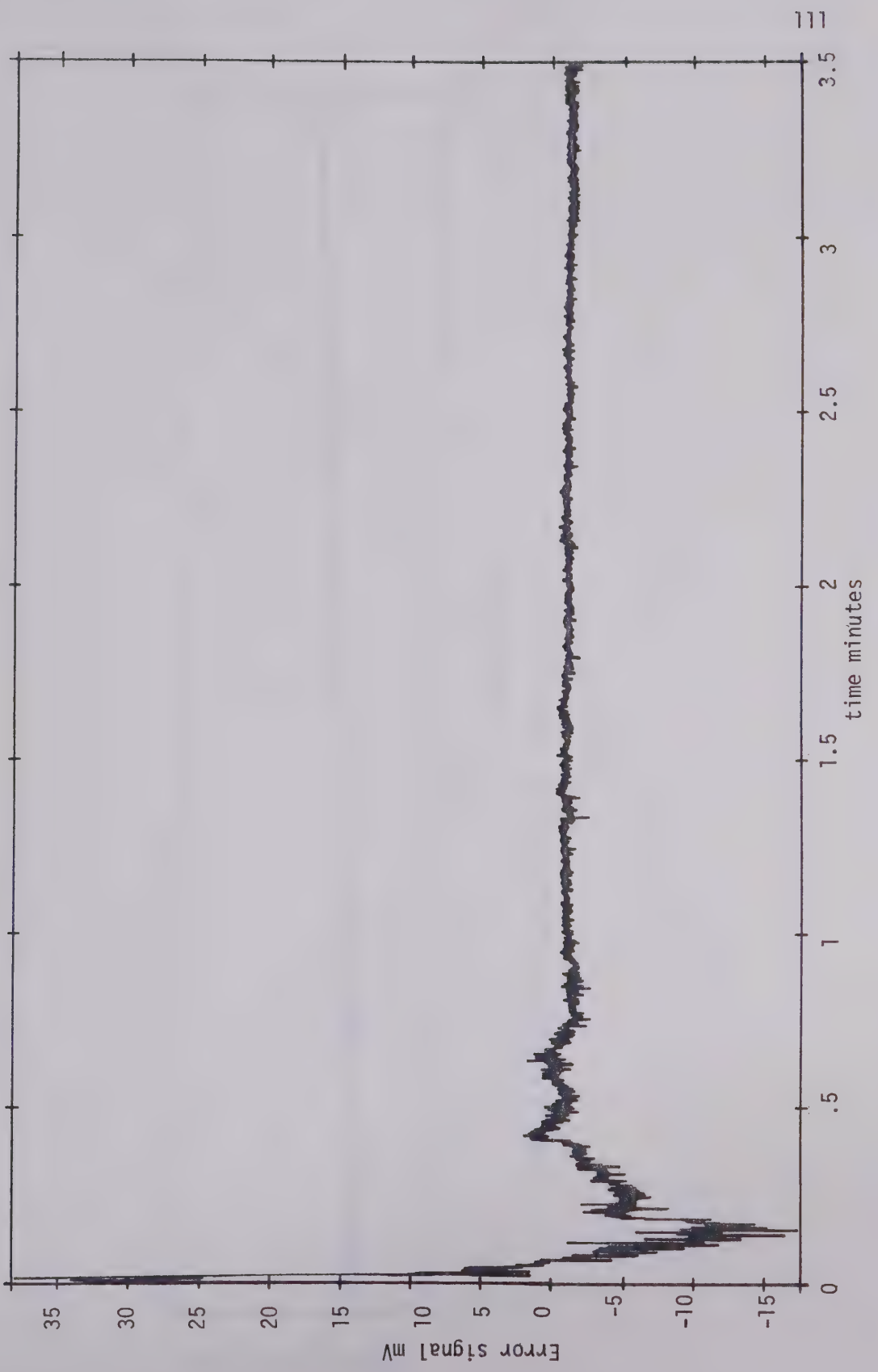


Fig. 5.4 Error signal (V_E) for a ramp input.

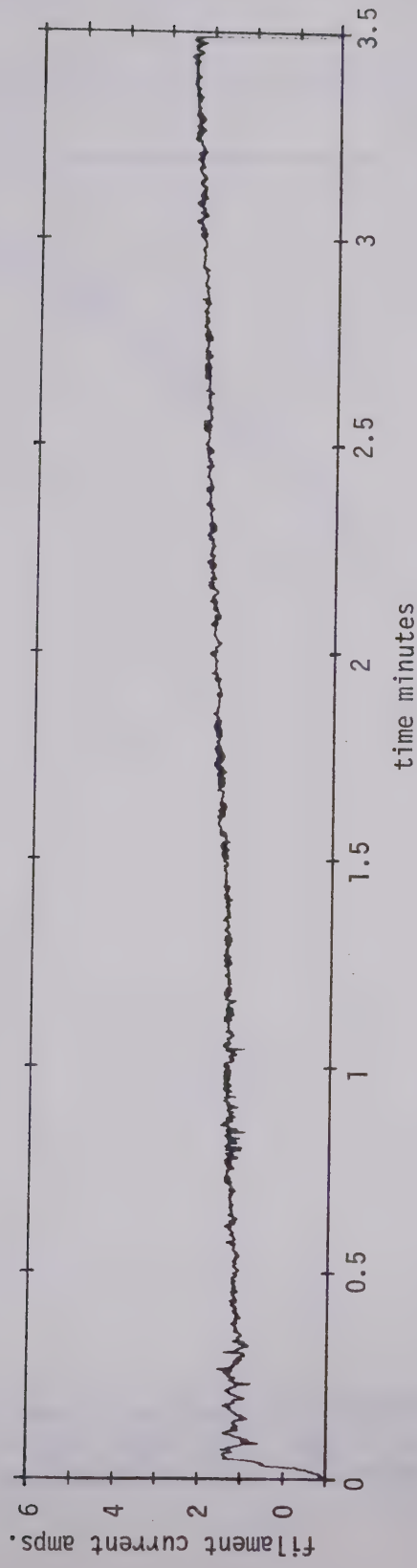


Fig. 5.5 Filament current (I_f) vs. time for a ramp input.

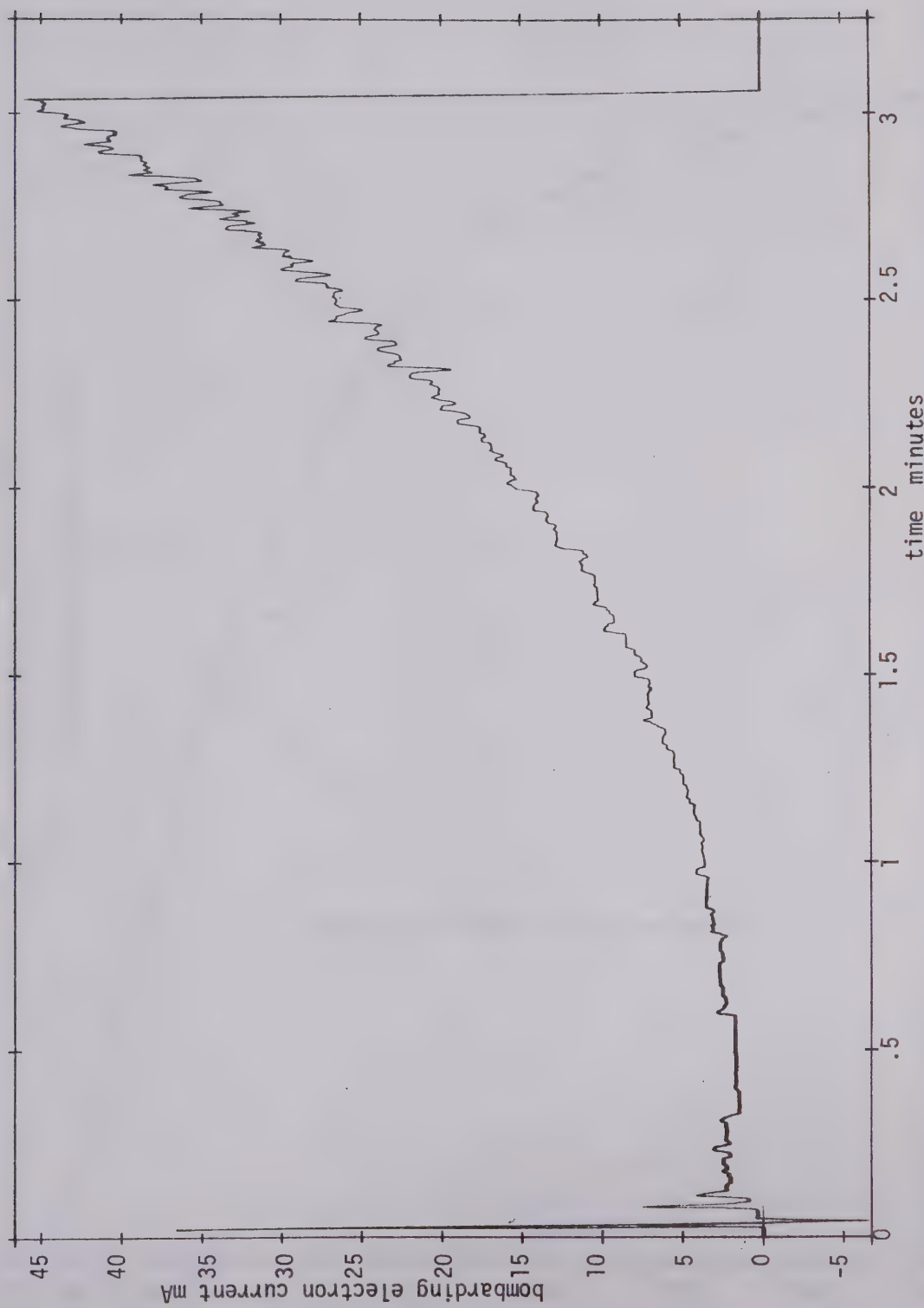


Fig. 5.6

Bombarding electron current for a ramp input.

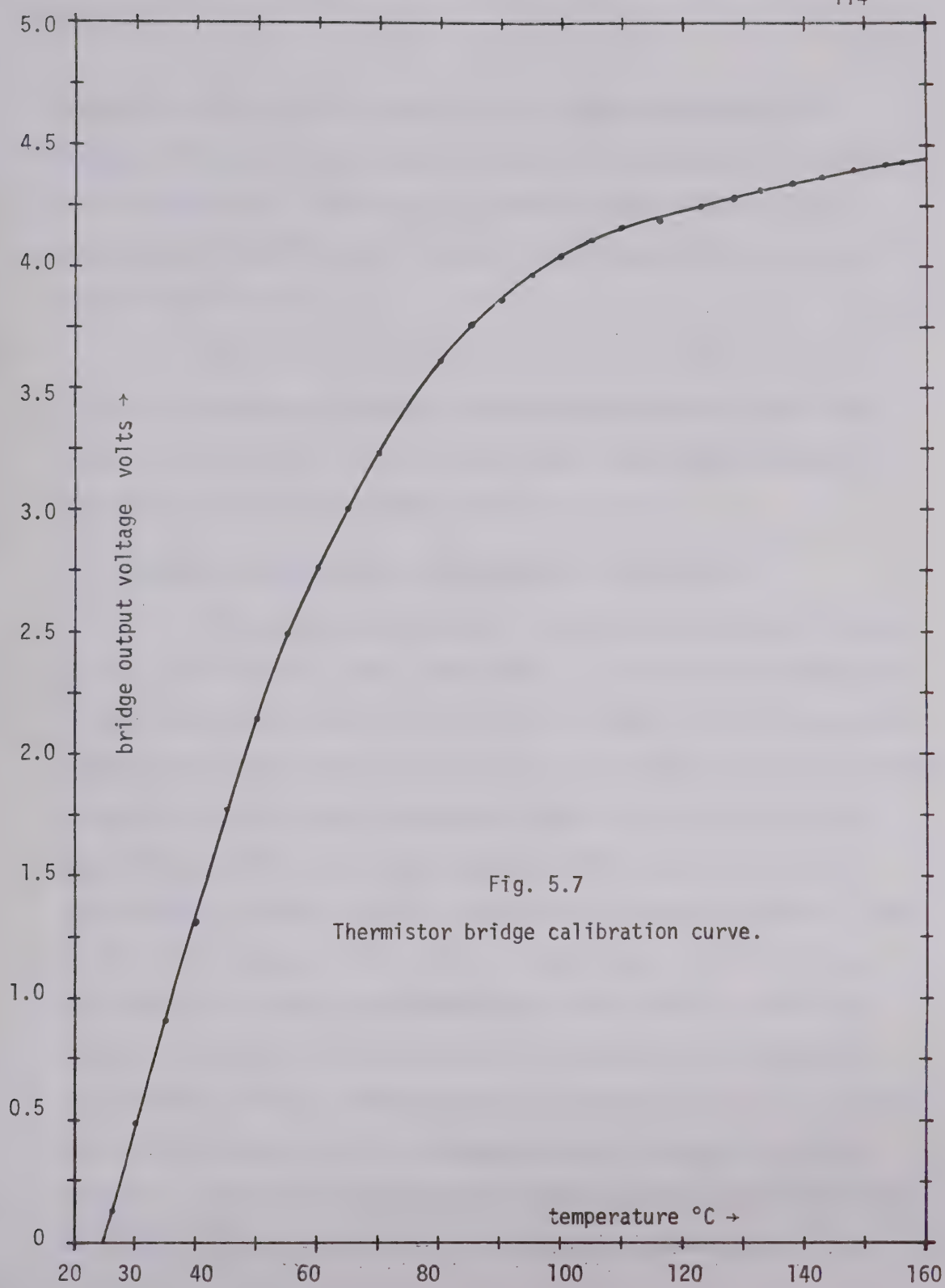


Fig. 5.7
Thermistor bridge calibration curve.

erature of less than 5°. However, at high temperatures near the target melting point this error is slightly increased due to the higher rate of heat loss. The linearity is also degraded when the input ramp speed is higher because the transient response affects a larger portion of the curve.

Figs. 5.4, 5.5, and 5.6 show the error signal, filament current and bombarding electron current respectively for a ramp input signal. These curves confirm the validity of the assumptions made in the analysis and also show the system performance.

5.4 Accuracy and Errors in the Measurement of Temperature

The best accuracy obtained from the thermocouple emf reading by means of the digital meter (DANA 3800) is .1mV which corresponds to a temperature difference of about 15°C. This means that the temperature reading is accurate within $\pm 15^\circ\text{C}$ as far as the digital meter is concerned. In addition to the direct thermocouple errors resulting from its own limitations in this kind of application, another cause of error is the reference junction becoming hotter during the heating period. Close to the final temperature this error is quite large. Within the heating period of 3 minutes the temperature at the reference junction was found to rise up to 45°C as measured by the thermistor bridge circuit. The thermistor bridge calibration curve is shown in Fig. 5.7. This temperature rise corresponds to a thermocouple emf reading of +.136 mV. Therefore at the target temperature of 1200°C the thermocouple emf should be $13.051 - .136 = 12.915$ mV but not considering other errors. The

increase in the reference junction temperature depends linearly (to a first approximation) on heating time period and the intensity of heat at the target and filament. Hence, for a long heating period, this error will be dominant and the temperature-time output for a ramp input will not be linear at high temperatures. It is then apparent that constant temperature control cannot be obtained over long time periods.

CHAPTER VI

THE STUDY OF DESORPTION SPECTRA

6.1 Introduction

This chapter demonstrates some of the desorption spectra obtained by using a linear time temperature schedule as described in the previous chapter. Some of these results will then be compared with those obtained by Burch².

6.2 Apparatus

In the present work the same ion beam generator and the same configuration as described by Burch were used to bombard a clean stainless steel target with measured doses of helium and argon ions within the energy range of 100 to 800 ev. Following bombardment the chamber was evacuated and isolated and the target temperature was raised at a known rate. The rate of pressure change caused by the desorption of the trapped gas was recorded by differentiation of the output signal from an AEI "Minimass" mass spectrometer tuned to the mass number of the inert gas.

The differentiating circuit as shown in Fig. 6.1 consists of a noninverting FET dc amplifier set at a gain of 100 followed by a low noise differentiator circuit.

Two matched, general purpose silicon JFET's, type MPF111 were used in the amplifier. The current source, comprising two 2N3904

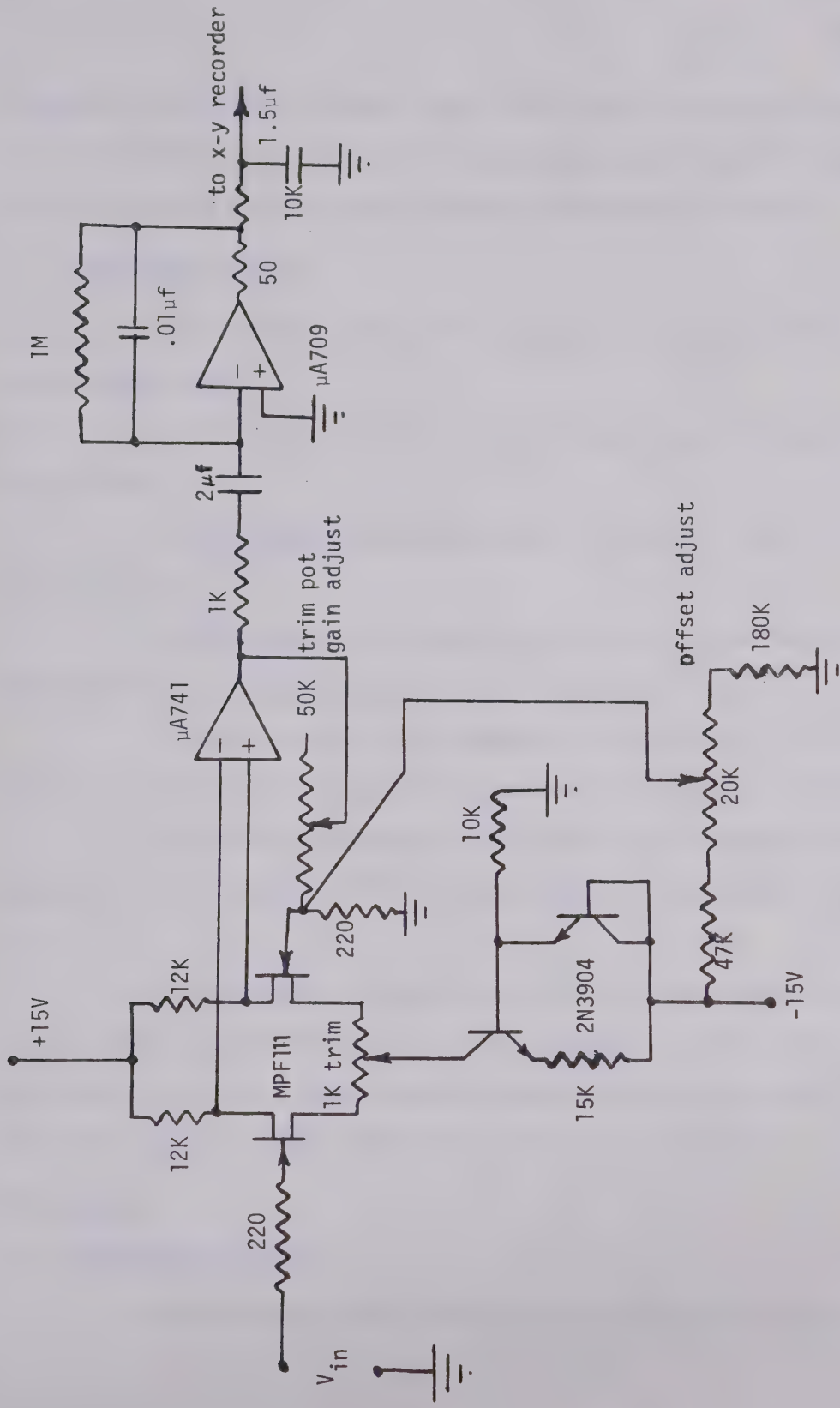


Fig. 6.1

Differentiating circuit

transistors as shown, delivered about 400 μ A. One transistor connected as a diode acted as a zener device to partially compensate for variations with temperature of the other transistor's base-emitter voltage.

6.3 Experimental Method

The bombardment-desorption sequence involved the following experimental steps:

1. The target was cleaned by heating by electron bombardment up to 1200°C.

2. The chamber was evacuated to a background pressure of 5×10^{-10} torr.

3. The chamber was isolated and an inert gas was admitted to the system to a pressure between 1×10^{-5} and 4×10^{-5} torr.

4. The clean target was bombarded at the selected ion energy and the target current recorded in a specified time period.

5. Following bombardment, the chamber was evacuated to a pressure of less than 5×10^{-10} torr with the mass spectrometer now turned on.

6. The chamber was again isolated, the target heated at a linear rate as controlled by the circuits described in this thesis and the time derivative of output from the mass spectrometer was recorded during the heating period, generating a desorption spectrum.

6.4 Results

6.4.1 Desorption Spectra

The desorption spectra obtained for incident ion energies of

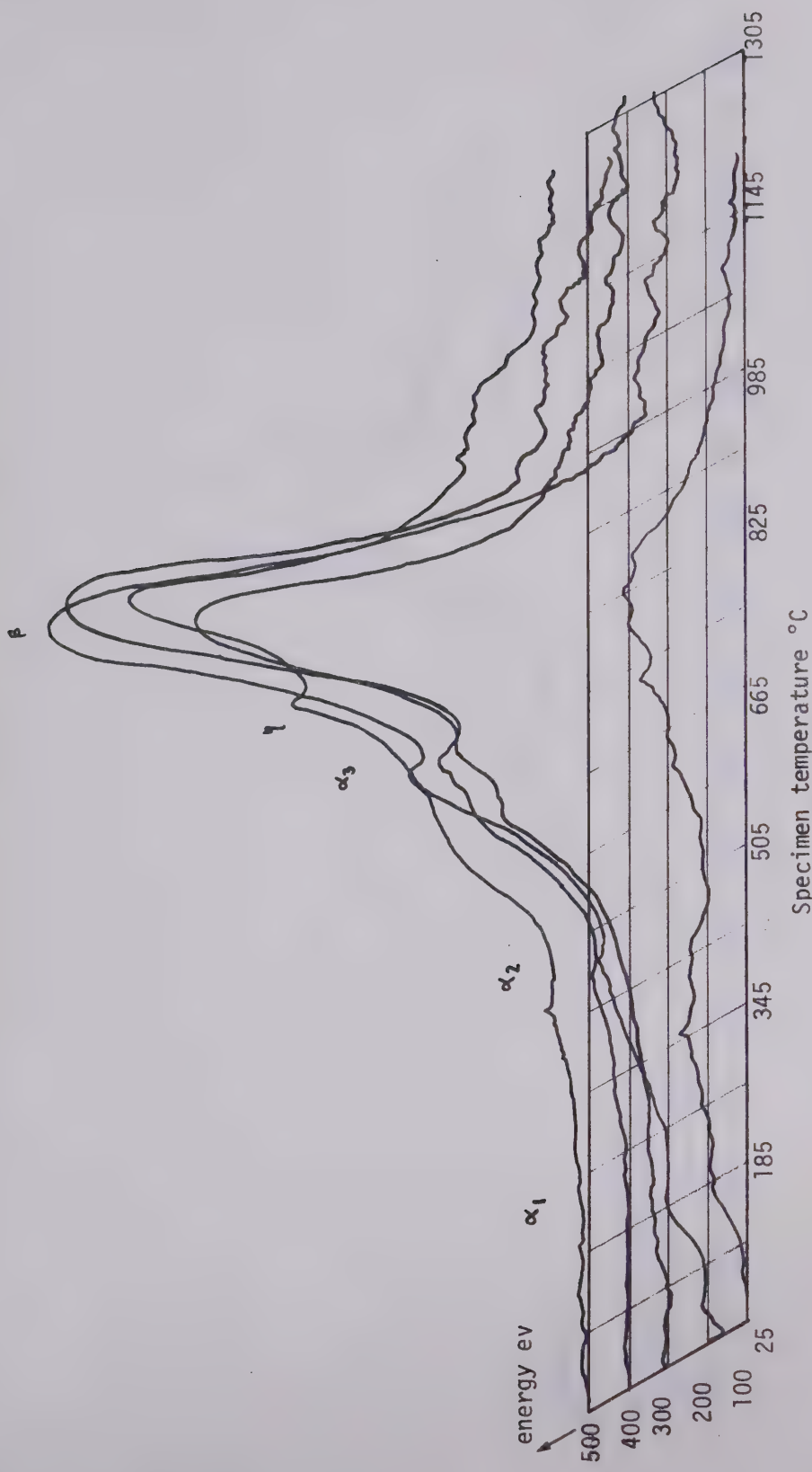


Fig. 6.2
 Helium desorption spectra at constant dose
 1×10^{14} ions/cm², heating rate $6.83^{\circ}\text{K/sec.}$



Fig. 6.3

Helium desorption at constant dose 1×10^{14} ions/cm 2 , heating rate $6.7^\circ\text{C}/\text{sec.}$

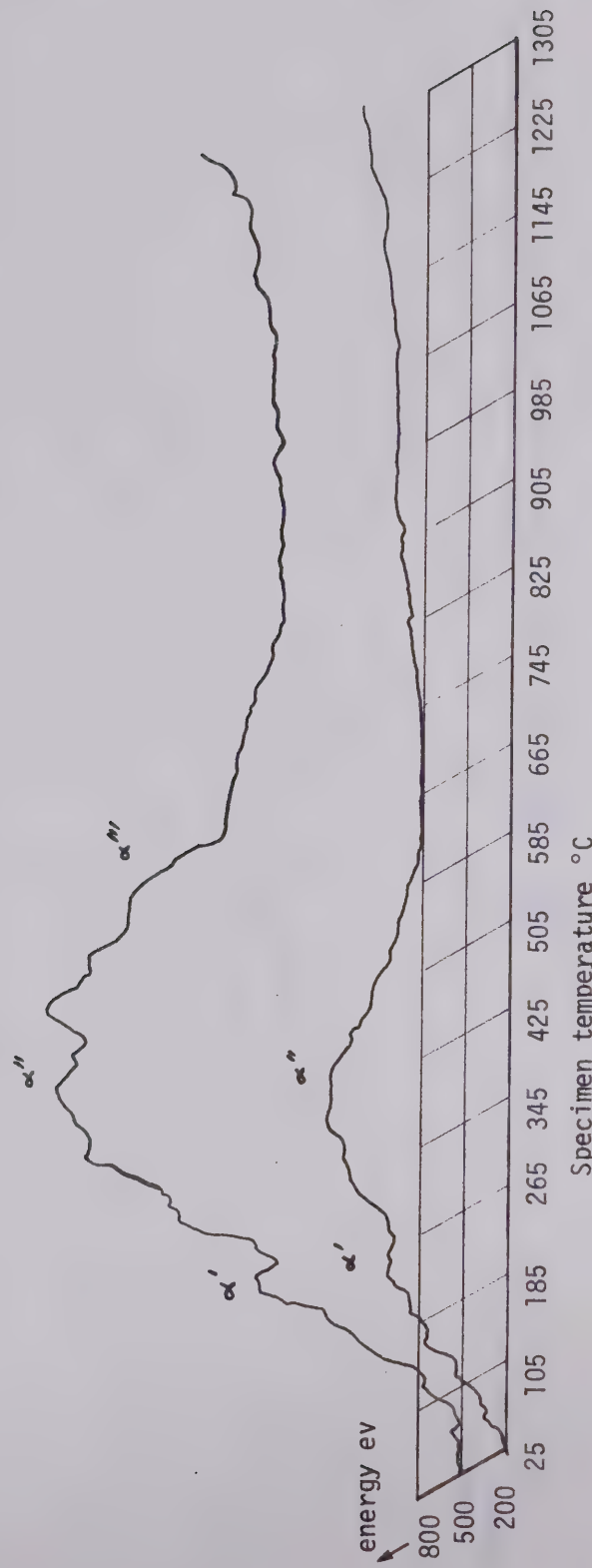


Fig. 6.4

Argon desorption at constant dose 1×10^{14} ions/cm², heating rate 5.25°C/sec.

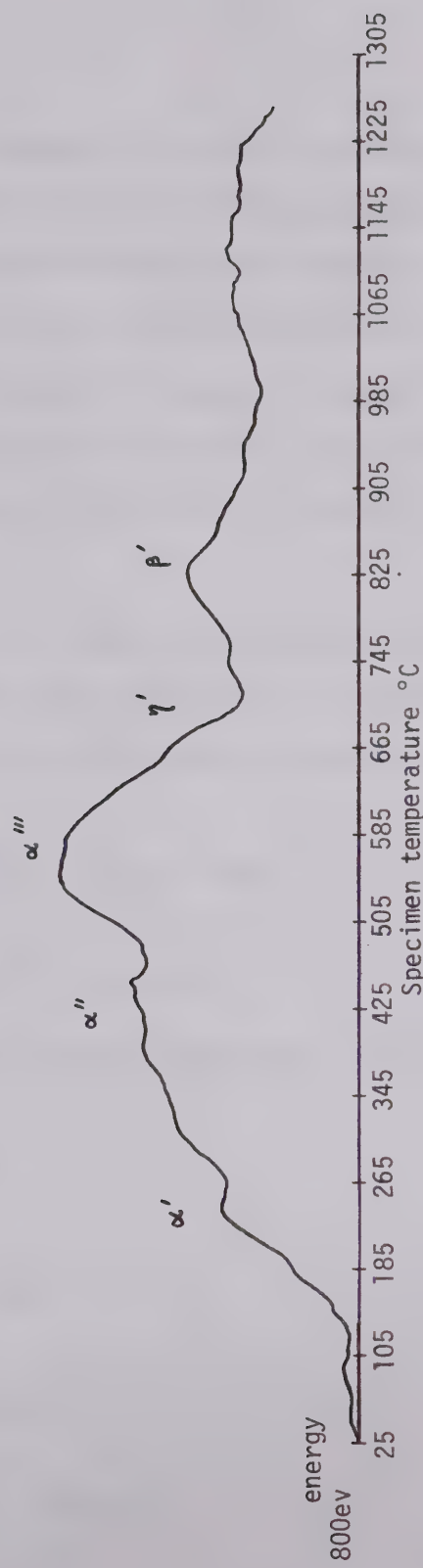


Fig. 6.5

Argon desorption at constant dose 1×10^{14} ions/cm 2 , heating rate 67°C/sec.

100 to 500 eV for helium are shown in Fig. 6.2. The heating rate is $6.83^{\circ}\text{K/sec.}$ from room temperature up to 1200°C approximately. Figure 6.3 shows desorption spectra of the same gas of incident ion energies 600 - 800 eV but the heating rate is slightly changed to $7.12^{\circ}\text{C/sec.}$

Two desorption spectra for argon at incident ion energies of 200, 500 eV with heating rates of 5.25°C/sec are shown in Fig. 6.4. Another spectrum at an energy of 800 eV with a heating rate of 6.7°C/sec. is shown in Fig. 6.5.

In all cases, the incident ion current was constant at 1.5×10^{-7} amperes throughout a 5 minute bombarding period. The target area is 2.25 cm^2 , hence the number of incident ions by measurement is

$$n(\text{meas}) = \frac{1.5 \times 10^{-7}}{1.6 \times 10^{-19}} \times \frac{1}{2.25} \times 60 \times 5$$

$$= 1.25 \times 10^{14} \text{ ions/cm}^2$$

However secondary emission reduces this to a value²

$$n(\text{true}) = \frac{n(\text{meas})}{(1+\epsilon)} \quad (6.1)$$

$$= 0.8n(\text{meas}) \quad (6.2)$$

$$= 0.8 \times 1.25 \times 10^{14}$$

$$= 1 \times 10^{14} \text{ ions/cm}^2.$$

The desorption spectra in Fig. 6.2 contain many distinct peaks which show pronounced variation with increasing energies. At low energies ≈ 200 ev there are 5 individual peaks. For ease of identification and comparision with previous work, these peaks are labeled α_1 , α_2 , α_3 , η and β in order of increasing temperature. The first three peaks are very wide and the α_1 peak is visible only at ion energies of 100, 200 ev at 150-160°C. The α_2 peak can be noticed up to an ion energy of 500 ev at 395-405°C.

The population of α_3 is much higher than that of α_2 but is found to decrease and maintain the same magnitude in spectra taken beyond 300 ev. This peak occurs at 590-600°C.

The η peak appears clearly in the 200 ev spectrum at 655-660°C but seems to contribute only slightly to the total gas desorption spectrum. It gradually decreases in magnitude and disappears in the 600, 700, 800 ev spectra.

The β peak is the most dominant peak in all desorption spectra and is found to shift from 765-775°C to 805-815°C in going from the 100 ev to the 500 ev spectra.

Fig. 6.3 shows the effect of increasing ion energy with only a slight increase in heating rate. Only two distinct peaks α_3 and β can be noticed. It is found again that the positions of the α_3 peaks are the same at 600-610°C but β peak shifts slightly from 850-860°C to 870-875°C. These two peaks eventually decrease in amplitudes for higher

ion energies as observed in the 800 eV spectra. Higher ion energy gas will be trapped more deeply below the surface and will require a higher energy for release. It can be seen from Fig. 6.3 that most gas is desorbed at higher temperatures. This also corresponds to the temperature shift that β exhibits for progressively higher incident ion energies.

The shape of the desorption spectra can be used to determine the order of the desorption reaction³. For a first order case the peak shape is expressed by

$$\ln\left[\frac{N_p}{N}\right] = \frac{E}{R}\left[\frac{1}{T} - \frac{1}{T_p}\right] + \left[\frac{T}{T_p}\right]^2 \cdot \exp\left[-\frac{E}{R}\left(\frac{1}{T} - \frac{1}{T_p}\right)\right] - 1 \quad (6.3)$$

where N_p = the rate of desorption at T_p ,
= maximum desorption rate.

This equation shows that for first order reactions the desorption rate curve is asymmetric about T_p .

For the second order case

$$\frac{N_p}{N} = \frac{1}{4} \left\{ \exp\left[-\frac{E}{2R}\left(\frac{1}{T_p} - \frac{1}{T}\right)\right] + \left(\frac{T}{T_p}\right)^2 \exp\left[-\frac{E}{2R}\left(\frac{1}{T} - \frac{1}{T_p}\right)\right] \right\}^2 \quad (6.4)$$

when $\left(\frac{T}{T_p}\right)^2 \rightarrow 1$, then

$$\frac{N_p}{N} \approx \cosh^2\left[-\frac{E}{2R}\left(\frac{1}{T} - \frac{1}{T_p}\right)\right] \quad (6.5)$$

Thus the desorption rate curve is symmetric about the maximum at T_p for $|T-T_p|$ small.

Using appropriate sweep speeds for the linear temperature-time schedules, as described in the previous chapter, will give good resolution and the symmetry of these peaks may be clearly distinguished simply by visual examination. The desorption spectra obtained were examined by use of this fact and only the β peak was found to be symmetric. The α -group peaks are asymmetric and too wide. The η peak is rather small and likely to be symmetric if it is not masked by α_3 and β peaks, however the other properties incline to those of the α group.

From the information discussed so far it can be summarized that for α group peaks the activation energies (which are functions of T_p) are independent of ion energy and their shapes are asymmetric. Those for the β group appear to increase with incident ion energy and their shapes are symmetric. The η peak behaves midway between the α and β groups. Thus it will be concluded that the α group peaks are first order processes and the β peak is a second order process. The processes governing the gas desorption in the η peak cannot be characterised by visual examination alone.

6.4.2 The determination of activation energies

The activation energies for α group peaks may be calculated from equation (1.4):

$$\frac{E}{RT_p} = \ln\left(\frac{v_1 T_p}{b}\right) - 3.64 \quad (1.4)$$

$$\text{Then } E = RT_p \left[\ln \frac{v_1 T_p}{b} - 3.64 \right] \quad (6.6)$$

$$= 1.986 \times 10^{-3} \times T_p \left[\ln \frac{10^{13} T_p}{b} - 3.64 \right] \text{ k cal/mole} \quad (6.7)$$

$$\text{or in electron volts : } E(\text{eV}) = \frac{E(\text{kcal/mole})}{23.05} \quad (6.8)$$

Redhead³ has shown that

$$\frac{\sigma_p}{\sigma_0} \approx \frac{1}{e_{n=1}} \approx \frac{1}{2_{n=2}} \quad (6.9)$$

where σ_0 = the coverage at the start of the temperature sweep,

σ_p = the coverage at temperature T_p .

The initial surface coverage can be obtained by measuring the area under the desorption rate curves, i.e.,

$$\sigma_0 = \int_0^{\infty} N dt \quad (6.10)$$

Using basic desorption rate equations and the approximation for $\frac{\sigma_p}{\sigma_0}$, it was shown for the linear sweep case that

$$\begin{aligned}
 E &= \frac{eN_p RT^2}{\sigma_0 b p} \quad : \text{ for } n = 1 \\
 &= \frac{4N_p RT^2}{\sigma_0 b p} \quad : \text{ for } n = 2
 \end{aligned} \tag{6.11}$$

Therefore at the same T_p and the same peak the activation energy obtained from the first order calculation (E_α) and that obtained from the second order calculation (E_β) will have the ratio

$$\frac{E_\beta}{E_\alpha} = \frac{4}{e}$$

$$E_\beta = \frac{4}{e} E_\alpha \tag{6.12}$$

Hence the activation energies of the β peaks can be calculated from equations (6.7) and (6.12). If gas desorption from the η peak can be regarded as a first order reaction process, the activation energy can then be found from equation (6.7).

The results from the calculation are tabulated below:

Results from Helium Desorption

<u>Peak</u>	<u>T_p</u> (approximated in $^{\circ}\text{C}$)	<u>Activation Energy</u> (kcal/mole)	(ev)
α_1	155	26	1.13
α_2	400	41.3	1.79
α_3	595	53.6	2.34
η	657	57.8	2.56

<u>Peak</u>	<u>T_p</u> (approximated in °C)	<u>Activation Energy</u>	
		kcal/mole	ev
β	765-815	95.35-99.25	4.14-4.32 (Ion energy 100-500ev)
	850-875	103.1-104.9	4.47-4.55 (Ion energy 600-800 ev)

In the high temperature region gas is continuously desorbed from many sites of different desorption energies. These small peaks with no gap between them make the analysis rather difficult and uncertain. For higher incident ion energy most gas desorbs from this region and the desorption rate will stay high until the target is melted.

The same phenomenon appears in the argon desorption spectra as shown in Fig. 6.4 and 6.5. By carefully examining these three desorption spectra some dominant peaks can be labelled as α' , α'' , α''' , and β' . Only the first two peaks appear in the low ion energy (200 ev) spectrum. The next peak (α''') arises in the spectrum for 500 ev ion energy and eventually all four peaks appear in the spectrum for 800 ev ion energy. Some additional peaks also appear between α group peaks.

It is interesting that the α group peaks and β' peaks in the argon desorption spectra correspond to those for the helium desorption spectra. This agrees with the observation¹ that the activation energies are the same for all gases, suggesting a release mechanism determined by the thermal behaviour of the lattice rather than of the trapped particle itself. It may be checked here by calculating the activation

energies of different peaks when the orders of reaction are known from the corresponding helium desorption peaks. The results are tabulated below:

Results from Argon Desorption

<u>Peak</u>	<u>T_p</u>	<u>Activation Energy</u>	
	(approximated in °K)	kcal/mole	ev
α'	460	28.2	1.22
α''	639	38.5	1.67
α'''	819	51	2.21
η'	943	58.6	2.54
β'	1108	101.5	4.41

It can be seen that the calculated activation energies given above agree with those obtained from helium desorption spectra within experimental error.

Another distinct peak appears between α'' and α''' peaks in Fig. 6.4 approximately at 718°K and has the activation energy 44.6 kcal/mole (1.94 ev).

It should be noticed that the resolution of the argon desorption spectra at low ion energy is rather low compared with helium and higher ion energy must be used to clarify all peaks. The reason for this concerns mass and radius of the trapped gas atom. The helium atom, having small radius and mass will have deeper penetration for a

given ion energy.

6.4.3 Comparison to previous results by Burch²

Most results from this work agree with those obtained by Burch. However, more peaks are found both in helium and argon desorption spectra and the activation energies for the β peaks are different.

Each peak can be compared by the order of the reaction and activation energy as follows:

present peak :	α_1	α_2	α_3	n	β	
peak found by Burch:	α_1	-	α_2	n	β	

The activation energies for α -group peaks and the n peak are in the same range but those for β peaks as calculated by Burch are between 2.98 to 3.08 ev while the values from the present work are between 4.14 - 4.32 ev for the same range of ion energy (100-500 ev). Different methods of calculation and different target configurations probably cause differences in activation energies.

CHAPTER VII

CONCLUSIONS

7.1 Summary

The work reported in the preceding chapters of this thesis can be summarized as follows. A proportional plus integral temperature controller was built for the linear control of the temperature rise of a stainless steel target from room temperature up to the melting point. Successful attempts were made to limit the number of complicated components in the construction of the controller while maintaining its efficiency and accuracy as required in this application. The solution resorted to some mechanical arrangement of the available potentiometers which become the most valuable parts of the controller and simplify all delicate work. Thus the design of the controller is electromechanical in nature. At least one high performance ramp generator and a summing amplifier with inherent drifts and offsets were eliminated.

The controlled thermal system appeared to be a nonlinear system mainly because of the associated radiant heat gain and heat loss from the target. The behaviour of the thermal system, as described by some complicated expressions, showed that the position of one pole of the thermal system depended on the actual target temperature. To avoid any difficulty in dealing with these nonlinear solutions, a linearizing method was introduced and the thermal system was approximated as a linear

second order system. Therefore, the entire system could be analysed and designed by using only basically linear techniques.

Stability of the system was obtained by cancellation of an unwanted pole in the transfer function of the system. After doing so, the Bode plot showed that the phase and gain margin of the system were very small. To keep the steady state error of the target temperature to a small level the controller gain had to be increased, again causing the system to be unstable. A phase lead compensation network had to be introduced into the feedback path to increase the stability and improve the system performance. The results were better linearity of the output temperature, no noticeable overshoots, greater overall system stability.

Many unavoidable errors in the temperature measurements are pointed out. These errors were due to the rapid deterioration of the thermocouple under the particular conditions of use, and the increase of the reference junction temperature during each run. When the control system was operated over a normal time period (3 minutes) of one run, the error due to the latter cause was small and of the same magnitude as the error from the measuring instrument.

To demonstrate the application of the controller and to study the gas adsorption from the surface of stainless steel (type 304) commonly used in vacuum system manufacture, some helium and argon ion desorption spectra for different ion energies were obtained. The results revealed

that the activation energies obtained from the desorption spectra for both trapped gases were in the same range. This shows that the activation energies are the properties of the material itself.

Generally most results agree with those obtained by Burch. The α -group peaks are first order reactions, the β peak is a second order reaction process while the η peak falls between the α and β characteristics. The activation energies for the α and η peaks in both this and Burch's work are within the same range but for the β peak the present values, as calculated by the method described, are higher.

7.2 Suggestions for Further Work

Considering the designed controller, better performance may be achieved by replacing all moving parts with electronic circuits specially designed for this purpose. The electronic controller will be more accurate, have better overall frequency response and be capable of controlling a faster rate of temperature rise. The integrator and summer should be modified such that the drifts and offsets which create additional errors are minimized. The target and filament configurations should also be modified so that heat transfer by the electron bombarding process is much more effective resulting in the effective gain of the thermal system being increased. This may also require another high voltage power supply capable of delivering more current at higher voltage. To implement the suggested improvements, the ultra high vacuum chamber may also have to be modified to prevent breakdown between the filament

current supply leads and the chamber.

Further useful information on surface properties of various materials may be obtained by performing different desorption tests using the facilities provided by this linear temperature controller.

BIBLIOGRAPHY

- [1] E.V. Kornelsen, "The Ionic Entrapment and Thermal Desorption of Inert Gases in Tungsten for Kinetic Energies of 40 EV to 5 KEV," *Can. J. Appl. Phys.*, vol. 42, pp. 364-381, 1964.
- [2] W.G. Burch, "Low Energy Ion Bombardment of Stainless Steel," *M.Sc. Thesis*, The University of Alberta, Canada, 1971.
- [3] P.A. Redhead, "Thermal Desorption of Gases," *Vacuum*, vol. 12, pp. 203-211, 1962.
- [4] G. Carter, "Thermal Resolution of Desorption Energy Spectra," *Vacuum*, vol. 12, pp. 245-254, 1962.
- [5] R.B. Burtt, J.S.-Colligon and J.H. Leck, *Brit. J. Appl. Phys.*, vol. 12, p. 396, 1961.
- [6] K.R. Spangenberg, "Vacuum Tubes," ch. 4, 8, McGraw-Hill, 1948.
- [7] W.H. Kohl, "Handbook of Materials and Techniques for Vacuum Devices," p. 570, Reinhold Publishing Corp., New York, 1967.
- [8] E.L. Chaffee, "Theory of Thermionic Vacuum Tubes," Ch. 4, 5, McGraw-Hill, New York, 1933.
- [9] American Society for Testing and Materials, Committee E-20 on Temperature Measurement, "Manual on The Use of Thermocouples in Temperature Measurement," 1970.
- [10] R.L. Forgacs, B.A. Parafin, and E. Eichen, "High Voltage Cathode Temperature Measurement," *The Review of Scientific Instruments*, vol. 36, No. 8, pp. 1198-1203, Aug. 1965.

- [11] M. Kutz, "Temperature Control," John Wiley and Sons, Inc., New York, 1968.
- [12] B. Gebhart, "Heat Transfer," Ch. 4, 5, Second Edition, McGraw-Hill, New York, 1971.
- [13] W.K. Roots, "Fundamental of Temperature Control," Ch. 3, Academic Press, Inc., New York, 1969.
- [14] P. Naslin, "The Dynamics of Linear and Non-Linear Systems," pp. 225-228, Blackie and Son Limited, London and Glasgow, 1965.
- [15] G.J. Deboo, C.N. Burrous, "Integrated Circuits and Semiconductor Devices - Theory and Application," Chapter 3, McGraw-Hill, New York, 1971.
- [16] "Application Note for μ A726 Temperature Controlled Differential Pair," Fairchild Semiconductor, Mountain View, California, 1967.
- [17] J.G. Graeme, G.E. Tobey and L.P. Huelsman, "Operational Amplifiers, Design and Applications," McGraw-Hill, New York, 1971.
- [18] "Application Note for MC1439G, MC1539G Operational Amplifiers," Motorola Semiconductor Products, Inc., Phoenix, Arizona, 1968.
- [19] "Application Note for MC1741, MC1741C Operational Amplifiers," Motorola Semiconductor Products Inc., Phoenix, Arizona, 1969.
- [20] F.W. Gutzwiller, et al., "SCR Manual," 4th Edition, General Electronic Company, Syracuse, New York, 1967.
- [21] K. Ogata, "Modern Control Engineering," Prentice-Hall Inc., Englewood Cliffs, N.J., 1970.

B30046